STUDY OF PURE-SILICA ZEOLITE NUCLEATION AND GROWTH FROM SOLUTION

A Dissertation

by

XIANG LI

Submitted to the Office of Graduate Studies of
Texas A&M University
in partial fulfillment of the requirements for the degree of

DOCTOR OF PHILOSOPHY

August 2011

Major Subject: Chemical Engineering

STUDY OF PURE-SILICA ZEOLITE NUCLEATION AND GROWTH FROM SOLUTION

A Dissertation

by

XIANG LI

Submitted to the Office of Graduate Studies of
Texas A&M University
in partial fulfillment of the requirements for the degree of

DOCTOR OF PHILOSOPHY

Approved by:

Chair of Committee,	Daniel F. Shantz
Committee Members,	Hae-Kwon Jeong
	Carl Laird
	Christian Hilty
Head of Department,	Michael Pishko

August 2011

Major Subject: Chemical Engineering

ABSTRACT

Study of Pure-silica Zeolite Nucleation and Growth from Solution. (August 2011)

Xiang Li, B.S., Beijing University of Chemical Technology;

M.S., Tianjin University

Chair of Advisory Committee: Dr. Daniel F. Shantz

Zeolites are microporous crystalline materials, which are widely used in catalysis, adsorption, and ion-exchange processes. However, in most cases, the synthesis of novel zeolites as functional materials still relies on trial-and-error methods, which are time consuming and expensive. Therefore, the motivation for this thesis work is to understand the zeolite synthesis mechanismand further develop knowledge for manipulating zeolite properties and ultimately the rational design of porous materials. This work focused on formation of silicalite-1 (pure-silica ZSM-5) from basic aqueous solutions containing tetraorthosilicate (TEOS) as silica source, and tetrapropylammonium (TPA) cations as the organic structure-directing agent. The presence of silica precursor particles with size of 2-5 nm in these mixtures prior to and during hydrothermal treatments have been observed through dynamic light scattering (DLS), small-angle X-ray (SAXS) and transmission electron microscopy (TEM). However, to quantify composition and the molecular structure transformation of these silica precursor particles during zeolite synthesis is still a technical challenge. Another important yet unresolved question is how organocations interact with these nanoparticles and direct zeolite nuclei. Unlike many studies performed analyzing the inorganic phase (silica) present in synthesis mixtures, this study quantified the organocation-silica particle interaction and its ultimate effect on zeolite growth mainly through probing the behavior of the organocations. Pulsed-field gradient (PFG) NMR was used to capture the mobility change of organocations, and was complemented with scattering measurements (DLS, SAXS) on the silica nanoparticles. On the basis of the measurement results, the thermodynamic and kinetic properties of the organic-inorganic interaction were derived. Upon aging at room temperature, this interaction manifested as binding of TPA onto the silica particles due to electrostatic interactions, and such binding behavior can be well described by the Langmuir adsorption model. Upon hydrothermal treatment, a fraction of TPA adsorbed at room temperature dissociates from the growing silica nanoparticles and the corresponding desorption profiles were fitted well by the pseudo-second order kinetic model. The addition of tetramethylammonium (TMA) as "competitors" promoted TPA desorption kinetics and hindered silica nanoparticle growth due to stronger association of TMA with particles than that of TPA. Finally, the TPA adsorption strength increased via addition of monovalent salts with increasing ionic size whereas that of TMA shows an opposite trend. This suggests one potential route for tuning the organic-silica precursor particle interactions and thus possibly affecting some kinetics steps in the synthesis.

ACKNOWLEDGEMENTS

I would like to express my deepest appreciation to my advisor, Dr. Daniel Shantz, for his inspiring and encouraging guidance throughout the course of my Ph.D. study. I also owe my academic achievements to my committee members, Dr. Hae-Kwon Jeong, Dr. Carl Laird, and Dr. Christian Hilty, for their valuable advice and suggestions. I would like to thank Dr. Steve Silber and Dr. K. P. Sarathy for their fruitful discussions and technical support on NMR instruments. I deeply appreciate the help and collaborations from my colleagues in Dr. Shantz's group and Dr. Jeong's group. Specifically thanks to Nataly G. Vargas for SEM workand Victor V. Guerrero for training on TGA and XRD instruments. Last but not least, I would like to thank my family and friends, especially, Yuan Lu, for his encouragement and generous support.

TABLE OF CONTENTS

LIST OF FIGURES

FIGURE Page

FIGURE Page

FIGURE Page

FIGURE Page

LIST OF TABLES

CHAPTER I

INTRODUCTION

1.1 Overview

Zeolites are one class of solid materials with a broad range of applications in catalysis, adsorption as well as nano-devices.[1-3] Given their importance in the chemical and refining industries, the nucleation and crystallization of zeolites has been widely studied for developing a molecular-level understanding of their formation mechanism and further rational design of novel zeolitic materials.[4-6] During the past decades, numerous *in situ* and *exit situ* techniques including small angle X-ray and neutron scattering,[7-10] microscopy,[11, 12] as well as NMR spectroscopy [13-15] have been introduced to investigate the nucleation and growth of zeolite from solutions. Findings from these works have provided useful insights for developing a more complete picture of zeolite formation. Another important, yet unresolved question is how organic molecules used for directing zeolite structures interact with silica species during the course of zeolite syntheses. In this study, pulsed-field gradient (PFG) NMR was employed to probe the motion of these organic molecules, from which quantitative insights about organic-inorganic interactions were obtained.

1.2 Zeolite Structures and Applications

Zeolites are microporous, crystalline aluminosilicates which are formed from

---

This dissertation follows the style and format of *Langmuir*.

primary tetrahedral units (TiO_4) linked to generate a three-dimensional framework structure. (See Figure 1-1) Given the flexibility in T-O-T bond lengths and angles, more than 200 zeolite topologies have been developed, and each is distinguished by its unique powder diffraction pattern.[16] These topologies are named according to a three-letter code, among which MFI, LTA, FAU are the most industrially relevant framework-type. While the classical zeolites are aluminosilicates, open frameworks with partial or full substitution by heteroatom can be synthesized and denoted as zeotypes. This include families of microporous crystalline aluminophosphate ($AlPO_n$), [17] and silica-and metal-alminophosphate (SAPO, MeAPO) molecular sieves. [18, 19]

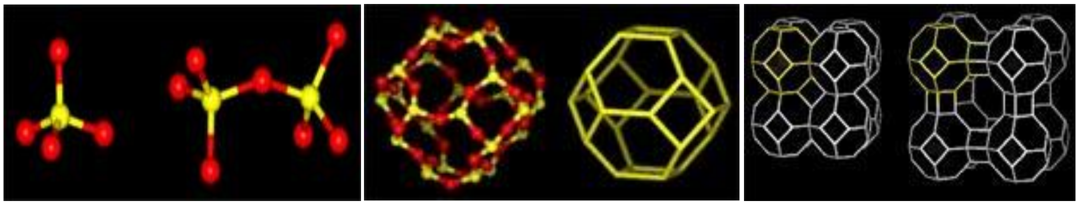

Figure 1-1. (from left to right) Primary building unit (TiO_4, Ti=Si or Al), secondary bulding units (Sodalite cage), zeolite A and zeolite Y. [20]

Since tetrahedral aluminum is negatively charged, zeolite frameworks containing aluminum need extra-framework cations, such as alkali or alkaline metal species (Na^+, K^+, Ca^{2+}), to maintain charge neutrality of the zeolite. [21] Thus, the general empirical formula of zeolite materials is shown as follows where *m* is the valence of cations (M) and *x* represents the alumina content.

$$M_{x/m}Al_xSi_{2-x}O_4$$

Hence, zeolites are usually classified into three different types with respect to Si/Al ratio: low-silica (Si/Al < 5) zeolites with high cation content and excellent ion-exchange ability, intermediate-silica (5<Si/Al< 10), and high-silica zeolites (Si/Al> 10) first reported by Mobil R&D laboratories during 1960s-1970s. [22, 23]

The fascinating catalytic properties of zeolites originate from three major reasons: pore structures, compositions and extra framework species. As shown in the above formula, the incorporation of a trivalent heteroatom, such as aluminium, in zeolites gives rise to a negative charge, which is the source of framework acidity. Figure 1-2 shows a typical zeolite acid site which consists of a hydroxyl group bridging a silicon atom and an aluminum atom corresponding to a strong Brönsted site and oxobridges with Lewis base properties.

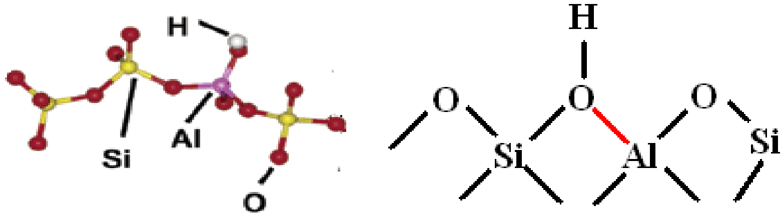

Figure 1-2. (Left) detail of the atomic structure, illustrating the linked tetrahedral (TO_4), (right) active site in zeolite framework showing T-O-T linkage.[24]

In addition, zeolites are size and shape selective regarding molecular adsorption due to the distinct pore systems with size of 0.3 nm to 1.2 nm (e.g., cages, channels and interconnected channels). Figure 1-3 shows the framework projections and the ring size for the most studied frameworks. The pore openings are uniform throughout zeolite crystals and have selectivity for molecules with dimensional differences less than 0.1 nm.

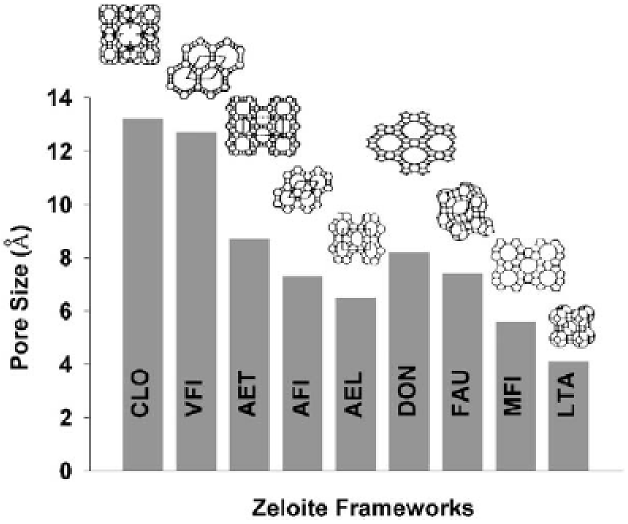

Figure 1-3. Comparison of pore size of different zeolite framework structures.[25]

For zeolite-catalyzed reactions, there are three types of shape selectivity as shown in Figure 1-4. Reactant selectivity depends on pore size limits on the entrance of the reactant molecules. Product selectivity occurs when the products are too bulky to diffuse out and thus converted to less bulky molecules. Transition-state selectivity refers to suppression of certain reactions due to pore limits on corresponding transition states of the reactions. [26]

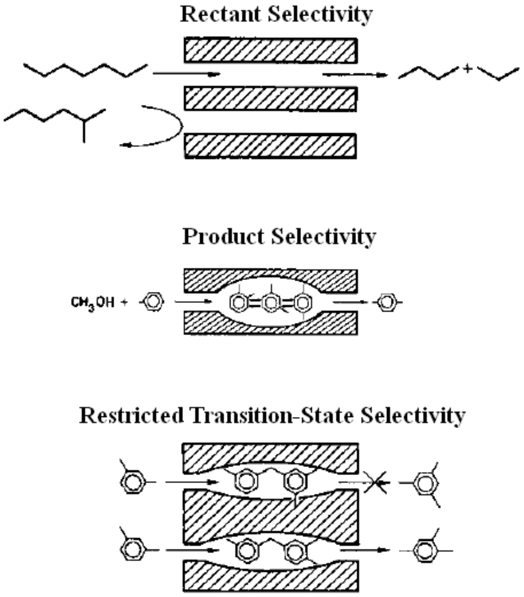

Figure 1-4. Different types of reaction selectivity imposed by rigid pore structure of zeolite. [26]

Table 1-1. Selected major catalytic applications of zeolites.[27]

Process	Catalyst	Products
Catalytic Cracking	Re-Y, US-Y, ZSM-5	Gasoline, Fuels
Hydrocracking	Y, Mordenite	Diesel, Benzene
Alkylation of aromatics	ZSM-5, Mordenite	p-xylene, ethyl-benzene, styrene
Hydroisomerization	ZSM-5	p-xylene
Catalytic dewaxing	ZSM-5	Improvement of cold flow properties
Methanol-to-gasoline	Ga-ZSM-5	Aromatics

Two of the largest markets for zeolite materials are in the petrochemical and chemical industries. FCC (Fluid Catalytic Cracking) of petroleum accounts for the most consumption of zeolite Y. MFI and MWW type zeolites are the most widely used additives to FCC catalysts for octane number enhancement.[28] Zeolites are also employed in purification of natural gas, separation of paraffin, desulfurization, as well as fine chemical productions. The major applications of zeolites are summarized in Table 1-1.

1.3 Hydrothermal Zeolite Synthesis

Given the scientific interest in zeolite structure-property relations and their industrial importance, much effort has been paid to zeolite synthesis. zeolites are synthesized under hydrothermal conditions from gels or clear solutions in alkaline or fluoride media at temperatures between 60 ^{o}C and 200 ^{o}C. Typical reagents include a silica source, an alumina source and organic molecules as structure-directing agents for high Si/Al ratio zeolite. Figure 1-5 highlights the developments of high-silica zeolite materials over the last several decades. [29]

1.3.1 Silica and Alumina Sources

Zeolite growth kinetics and framework structures can be affected by dissolution of the solid reactants as well as formation of aluminosilicate precursors in synthesis mixtures. The typical silica sources for industrial usage are fumed silica or sodium silicate solutions which require significant dissolution time to research the desired zeolite growth conditions. Hydrolysis of tetraethyl orthosilicate (TEOS), a high cost reagent, yields mononeric silica sources more quickly. Also the formation of ethanol as byproducts of TEOS hydrolysis needs to be accounted when analyzing synthesis mixtures.[30] Sodium aluminate is most the common aluminum source but has low water solubility which can limit the range of experimental studies of precursor solutions. [31]

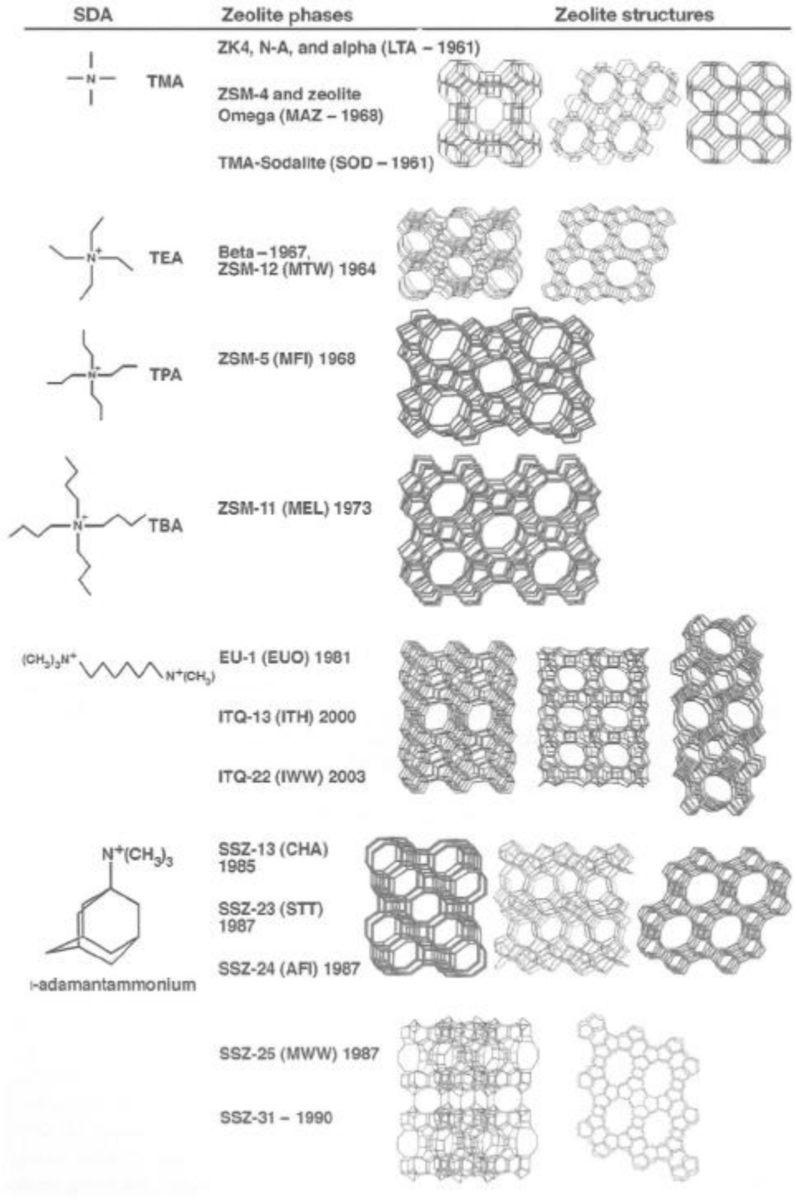

Figure 1-5. Development of zeolites synthesized using organic ammonium cations. [29]

1.3.2 Structure Directing Agent (SDA)

Many different types of molecules can be used to form zeolites. These include alkali cations, organocations, ethers, etc. Although the precise role of these molecules during - zeolite formation is not fully understood, they can act as space fillers, templates or structure director.[3, 4] In most cases, the inorganic and small organic species fall into the group of space fillers, which are loosely incorporated within zeolite frameworks. However, there is neither translation of the organic into the final zeolite structures, nor is necessarily 1:1 selectivity between organic species and zeolite structures.[32, 33] A few organic molecules serve as true templates. They often have rigid structures which enable them to form specific zeolite frameworks. The synthesis of SSZ-58 and ZSM-18 can be considered as examples and are shown in Figure 1-6.[34, 35] Particularly, the tri-quat molecule is a true template in that the ZSM-18 cage has C3 rotational symmetry, same as the organocation.[34]

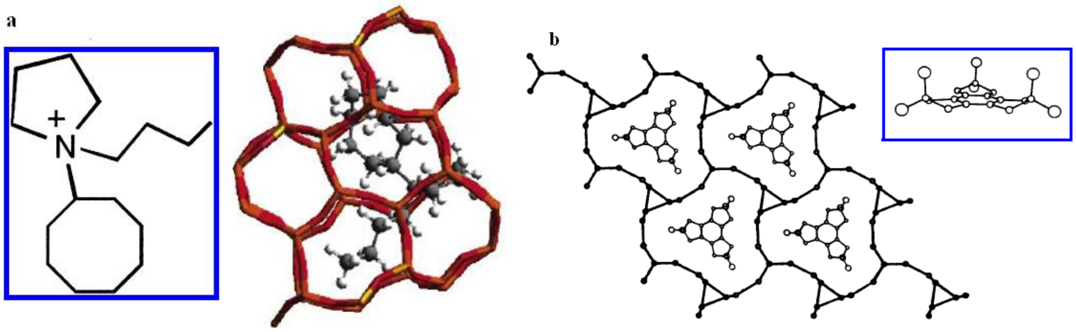

Figure 1-6. (a) Energy-minimized configuration of 1-butyl-1-cyclooctylpyrrolidinium SDA (within frame) with the cavity at the channel intersections of SSZ-58.[34] (b) The proposed locations of the tri-quat (within frame) relative to the 3-rigns in ZSM-18 framework along (001) unit cell direction.[36]

Many organic molecules act as structure directing agents, in that they appear to strongly favor the formation of specific zeolite phases. A typical example is synthesis of ZSM-5 which is aluminum-containing form of MFT framework, with tetrapropylammonium (TPA) as SDA. ZSM-5 crystallizes in the orthorhombic space group P_{nma} with lattice constants *a*=20.1 Ǻ, *b*=19.7Ǻ and *c*=13.1 Ǻ, and contains two channels (one straight and one sinusoidal) with pore size of 5.1-5.6 Ǻ. [23, 37] The TPA is located in the intersection of the two channels with four hydrocarbon chains each extending into one channel, as shown in Figure 1-7. Despite that ZSM-5 can be synthesized using inorganic cations and organic molecules other than TPA, it is more difficult to make phase-pure MFI materials in the absence of TPA.[18]

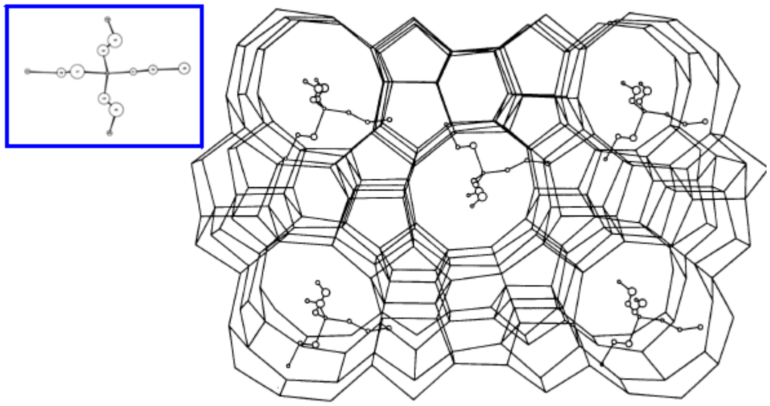

Figure 1-7. Molecular structure of TPA (within the frame) and packing diagram with Si atoms as framework viewed along (010) face.[38]

Given the unique role of TPA in MFI synthesis, the influence of other tetraalkylammonium (TAA) cations has been examined in the presence of alkaline metal

(Li^+, K^+).[39-41] Tetramethylammonium (TMA), more hydrophilic than TPA, directed ZSM-5 and ZSM-39 in presence of Li^+, whereas in the presence of K^+, ZSM-39 and ZSM-48 were formed at high TMA concentrations.[39] Tetraethylammonium (TEA) is intermediate in behavior and led to ZSM-5 as the main zeolitic phase whereas ZSM-11 is obtained using tetrabutylammonium (TBA).[40] The stabilization energies as a function of TAA cation occluded in ZSM-5 and ZSM-11 are compared in Figure 1-8. As can been seen, the energy increases to a maximum for TPA and declines in progressing to TBA assuming four TAA per unit cell. Reducing the loading to three TBA per unit cell leads to a slight increase in stabilization energy yet the value is still less than that obtained with four TPA per unit cell. One explanation is increasing the length of alkyl chain results in an increase in organic-zeolite non-covalent interactions and the repulsive interactions between end methyl groups of TBA.[41]

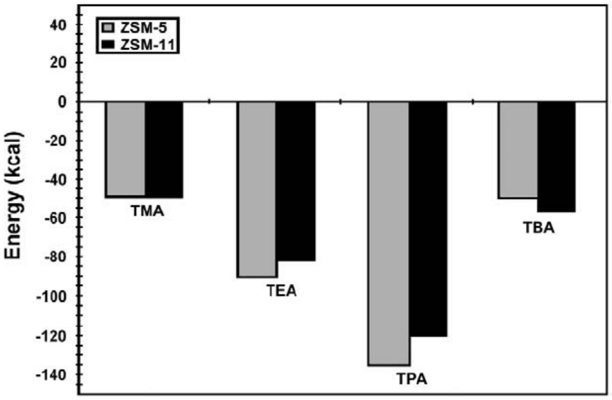

Figure 1-8. Stabilization energy of tetraalkylammonium (TAA) cations occluded in ZSM-5 and ZSM-11 at an occupancy of four cations per unit cell. [25, 41] (All energies are in kcal per unit cell.)

While there are many cases where multiple SDAs give the same zeolite framework, the flexibility and physicochemical properties of SDA play an important role in their phase selectivity.[3, 42-46] In general, increasing the bulk size of SDA with increasing C+N number results in a decrease in the number of zeolite frameworks that can be formed in its presence, i.e., increasing phase selectivity. (see Figure 1-9).[4]

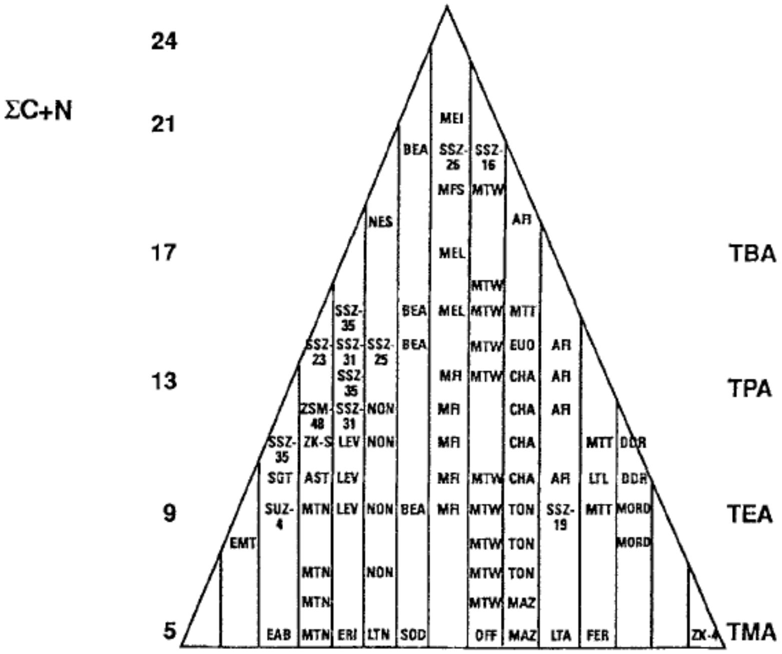

Figure 1-9. Illustration of the increased selectivity of different SDA as the size of the molecule (C+N) is increased.[4]

Figure 1-10 proposes a synergetic balance between the hydrophilicity of the organic SDA and hydrophobic features of the high/pure-silica zeolites directed by the SDA. [44, 47] As shown in Figure 1-10a, the organocations with C/N ratios ranging from 11 to 15 are effective SDAs for directing zeolite formation partially due to their moderate hydrophobicity. Furthermore, this hydrophobic character of the SDA could be independent of its structural symmetry as suggested by Figure 1-10b.[4]

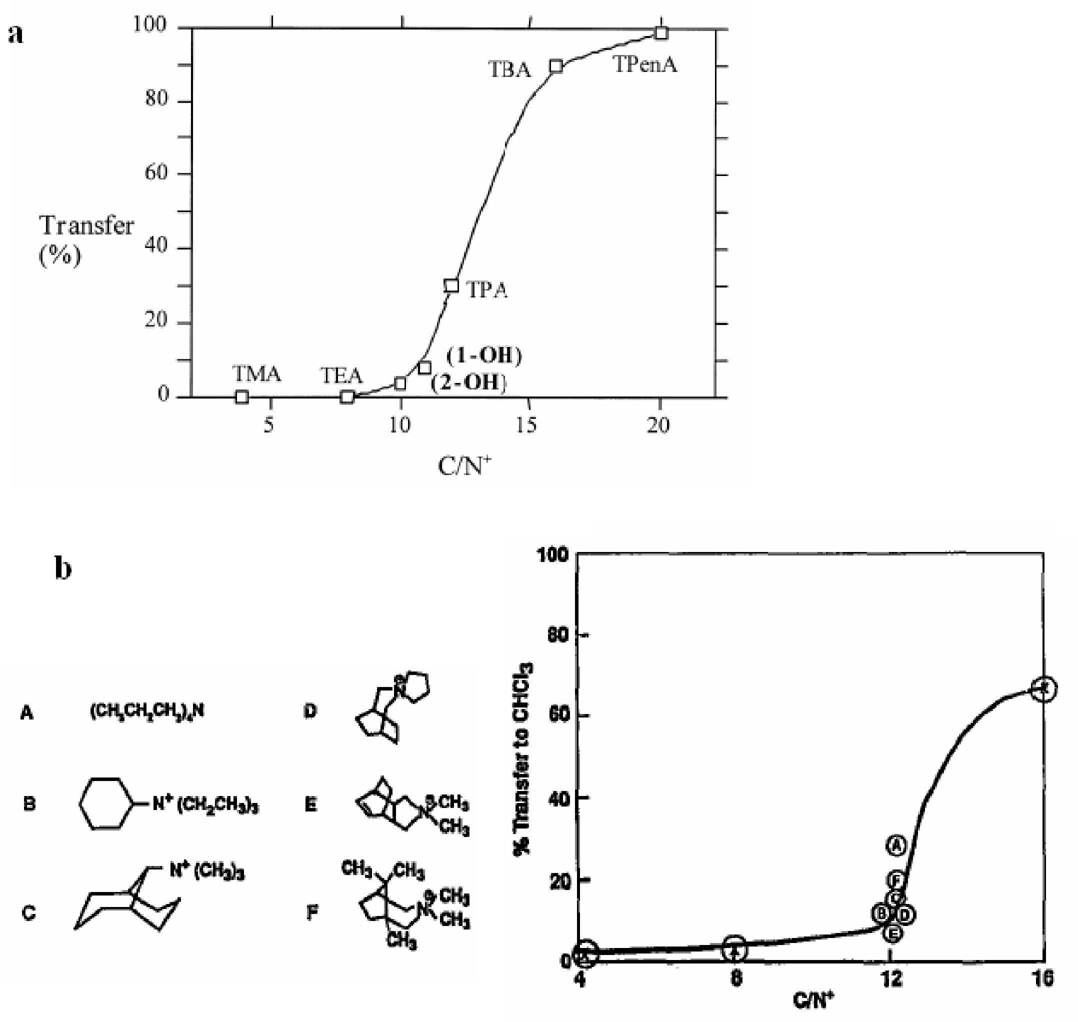

Figure 1-10. (a) Percentage of the ammonium iodide salt transferred from the aqueous to the chloroform (organic) phase. (TPenA represents tetrapentylammonium)[47].(b) Partition of quaternary ammonium compounds between water and chloroform.[4]

1.4 Zeolite Nucleation and Crystallization

Zeolite synthesis under hydrothermal condition is simple to perform but involves complex silica chemistry and transport. Also the numerous interdependent quasi-equilibria and condensation steps occur simultaneously during zeolite growth, which complicates the mechanisitic studies. Unlike covalent organic synthesis which can be divided into numerous reactions with separate reagents, separation of desired from unwanted steps and products for zeolite synthesis is always difficult. In other words, there may not be a universal mechanism describing all zeolite growth. Thus, this work emphasizes high and pure-silica zeolite formation from solution using organic molecules.

1.4.1 Early Studies of Zeolite Formation Mechanism

There are two primary categories of growth mechanisms for zeolite synthesis: gel-phase mechanism and solution-phase mechanism. The gel structure shown in Figure 1-11 is depolymerized by hydroxide ions. The hydrated alkali metal cations rearrangthe aluminosilicate and silicate anions in the hydrogel, leading to the formation of polyhedral units and ultimately, zeolite structures.[48, 49] One can view zeolite growth from solution as a process with multiple stages including nucleation of various structures, crystallization and dissolution of metastable species (See Figure 1-12). The conversion of silica-alumina species to crystals accelerates once the crystallization process starts, suggesting that nucleation is the rate-limiting step.[50] Tezak and Flanigen [51, 52] suggested four substages involved in zeolite synthesis: formation of monomer and polymeric aluminosilicates, aggregation of these complexes to form zeolite embryo, nucleation as aggregate formation with a well ordered primary particles, and finally aggregation of primary particles via oriented aggregation.

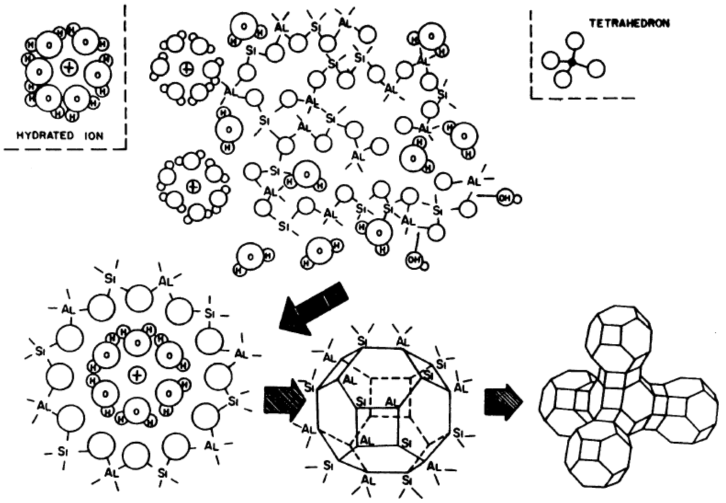

Figure 1-11. Schematic view of the formation of zeolite crystal nuclei in hydrous gel.[51]

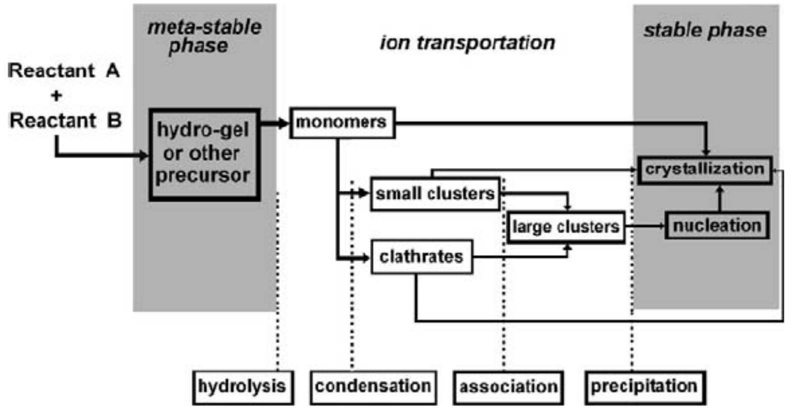

Figure 1-12. A schematic view of zeolite synthesis process.[53]

Cufaz and co-workers [54] introduced a semi-quantitative method for estimating zeolite nucleation and growth kinetics. Assuming that the rate-limiting step was crystal growth, they measured crystallization rates as the percentage conversion per hour at the highest rate (50% conversion). A similar treatment of nucleation rate was taken as the reciprocal of the induction period. (see Figure 1-13). A number of framework types (e.g., LTA, FAU, MFI) follow such trend in growth, where by an induction period for nucleation is followed by linear growth rates that level off when crystallization approach completion.[25] Vlacho's lab established a population balance formulation to describe zeolite growth from precursor gels, which is in qualitative agreement with experiment results and shown in Figure 1-14. [55, 56]

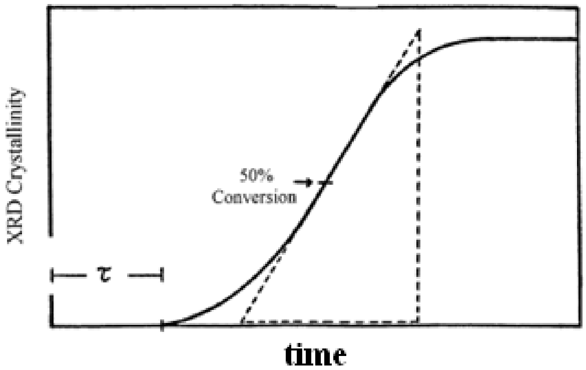

Figure 1-13. Nucleation rate is taken as the reciprocal of the induction time and crystallization rate as the slope of crystallization curve at 50 % conversion. [54]

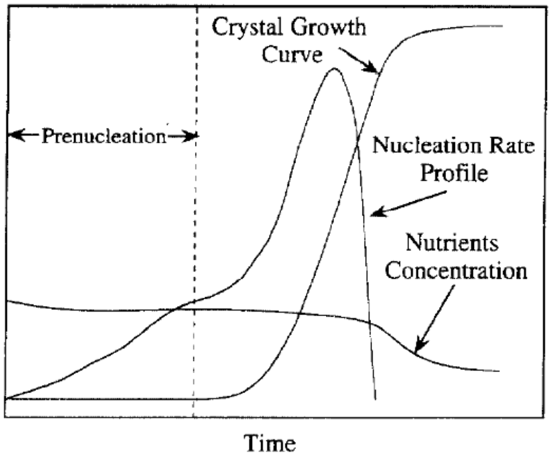

Figure 1-14. Schematic view of the nucleation rate, crystal growth and nutrient content as function of zeolite synthesis time. [56]

1.4.2 Studies of TPA-ZSM-5 Synthesis

The synthesis of ZSM-5 (MFI) has been widely studied as a model system for understanding zeolite formation. Its siliceous form, silicalite-1, can be synthesized exclusively using TPA over a wide range of experimental conditions including gel and solution systems (see Figure 1-15). [57] Unlike aluminum-containing MFI zeolites which are hydrophilic, silicalite-1 is hydrophobic, and selectively adsorbs organic molecules in the presence of water. [58] Studies on silicalite-1 synthesis began on hydrogels containing sodium hydroxide (NaOH), a fumed silica source and TPABr. Transformation of amorpohous silica gels to crystals was monitored using small-angle scattering of X-ray and neutron, suggesting the presence of primary particles with size of ~12 nm which grow during heating time. [59-61] Solution syntheses of nanoscale ZSM-5 have been developed as to date, many studies investigated the synthesis mechanism of pure ZSM-5 under a wide synthesis composition range and summarized in Figure 1-16.

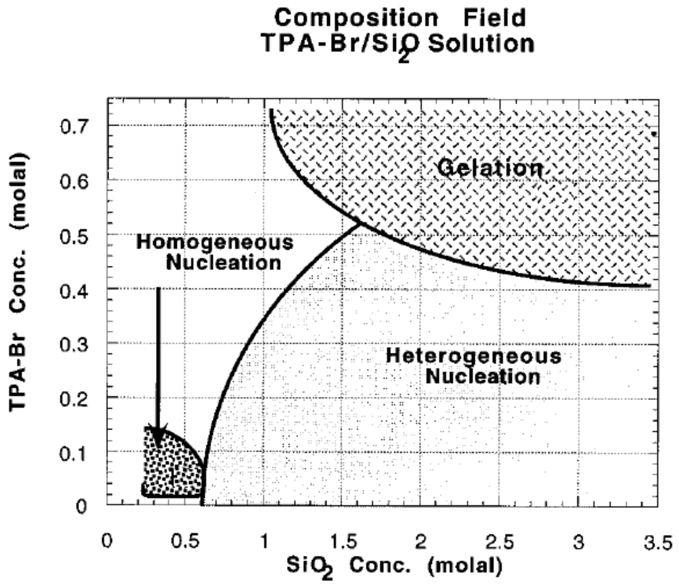

Figure 1-15. Diagram of crystallization behavior of TPA-silicalite-1.[57]

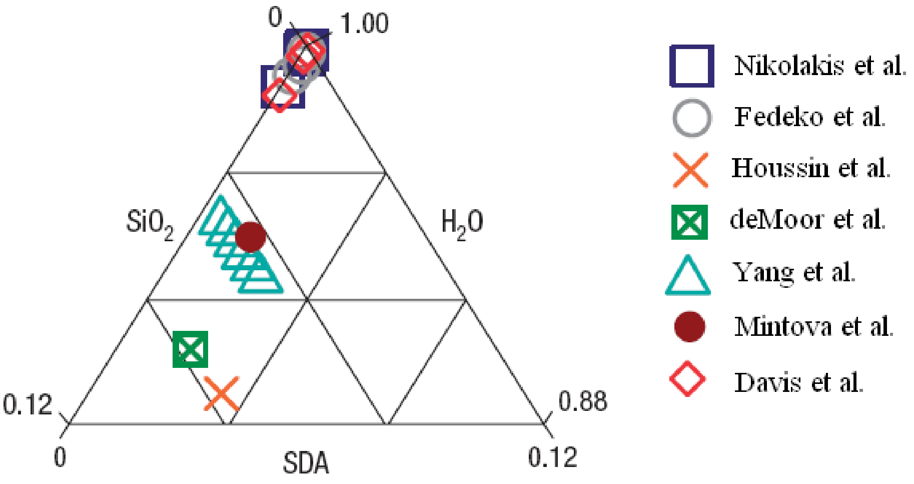

Figure 1-16. Composition (molar fraction) range investigated in TPA-silicalite-1 studies to date. (□Reference [62]; ○ Reference [7]; × Reference [63]; ⊠ Reference [64]; △ Reference [65]; ● Reference [66]; ◇ Reference [11])

Despite debate over the growth mechanisms, the silica precursors present in synthesis mixtures and their interactions with organic SDA, the proposed mechanisms can be classified into two roughly groups. The 'monomer/oligomer addition' mechanism, as shown in Figure 1-17a, suggests that TPA organizes soluble silica species into a portion of its hydration sphere via the hydrophobic interactions, leading to the formation of organic-inorganic composites. These composite spheres aggregate and participate in nucleation with addition of silica monomers/oligomers. The following crystal growth occurs via diffusion of these above species to the growing crystalline cores.[67] The second mechanism proposed that addition of colloidal nanoparticles to growing zeolite nuclei via aggregation mechanism. (see Figure 1-17b) Kirschhock and Houssin suggested these particles as zeosil nanoslabs with included TPA on the basis of TEM and SAXS measurements (See Figure 1-18a).[68] [27, 62, 69] [70] However, the nanoslab models has subsequently been disproved by several laboratories. [71, 72]

Many labs, including the Lobo, Vlachos, Tsapatsis and Shantz laboratories suggested these colloidal particles are initially amorphous and surrounded by a shell of organic SDA (see Figure 1-18b) on the basis of SAXS and SANS measurements. [7, 72-77] Furthermore, the average particle size are largely controlled by solution alkalinity and nearly independent of organocations studied.[78] Along this theme Tsapatsis and co-wokers [11, 12, 79-81] proposed that these amorphous precursor particles contribute to growth, and their direct addition to the growing crystal can be rate limiting. (see Figure 1-19) Intensive experimental studies on kinetics and thermodynamics of zeolite growth have been performed to develop these above mechanisms.

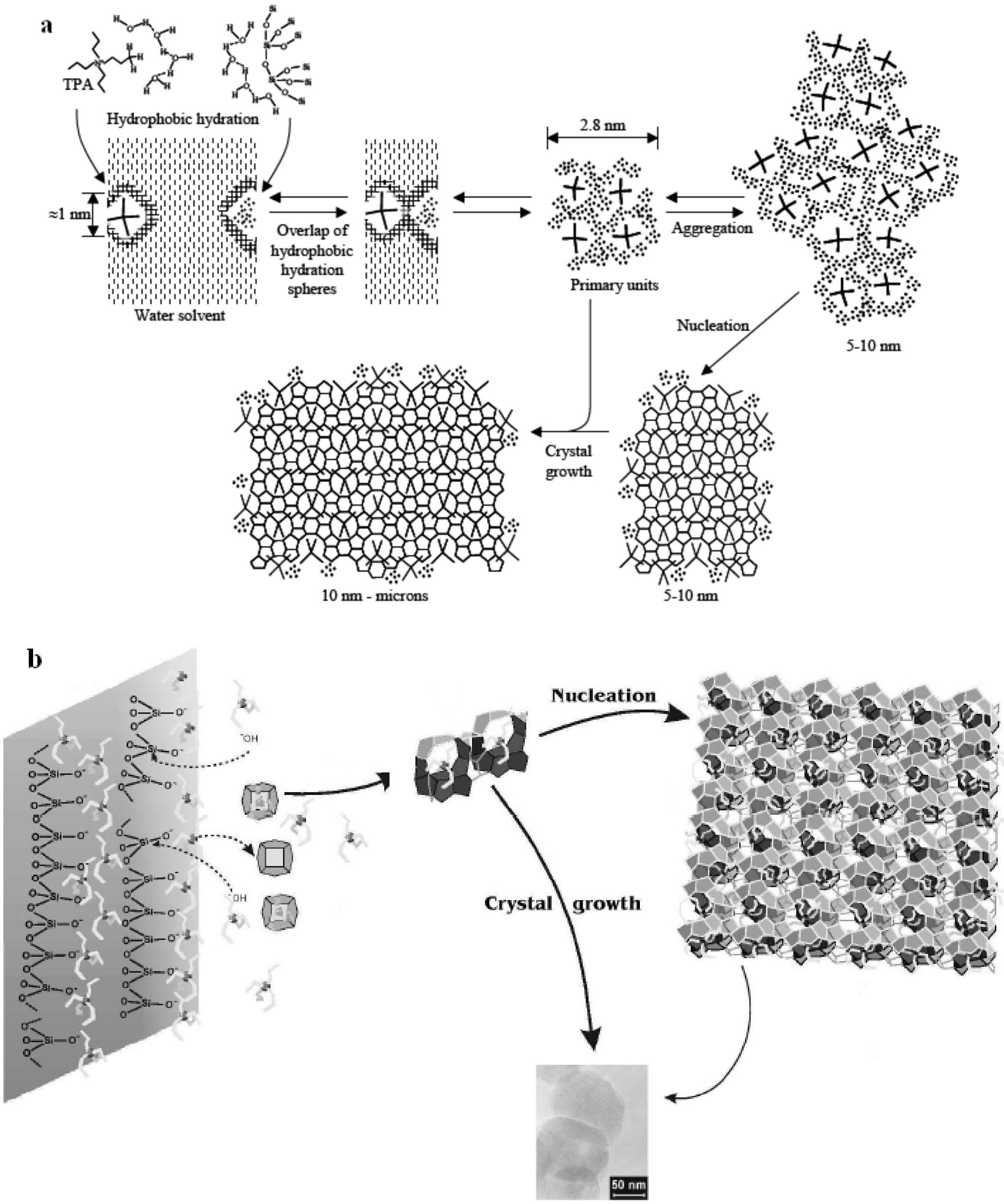

Figure 1-17. (a) Schematic view of TPA-silicalite-1 crystal growth involving inorganic-organic composite species.[67, 82] (b) Schematic crystallization of TPA-silicalite-1 via aggregation of nanoslabs with zeolite structures.[27]

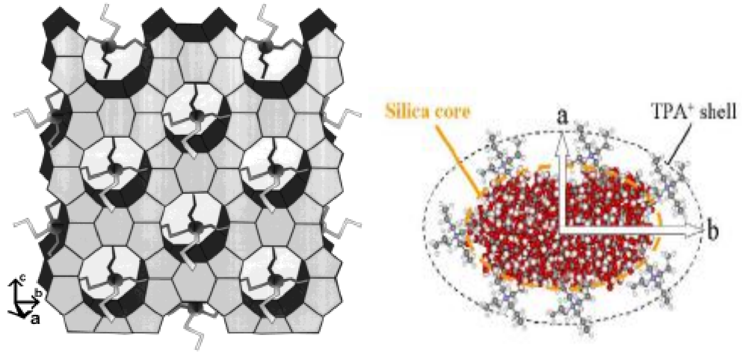

Figure 1-18. (a) Schematic view of a proposed nanoblock with included TPA.[69] (b) Ellipsoidal core (silica)-shell (TPA) structure of precursor nanoparticles formed from TEOS hydrolysis. (Ellipsoidal axes are labeled as a and b.) [78]

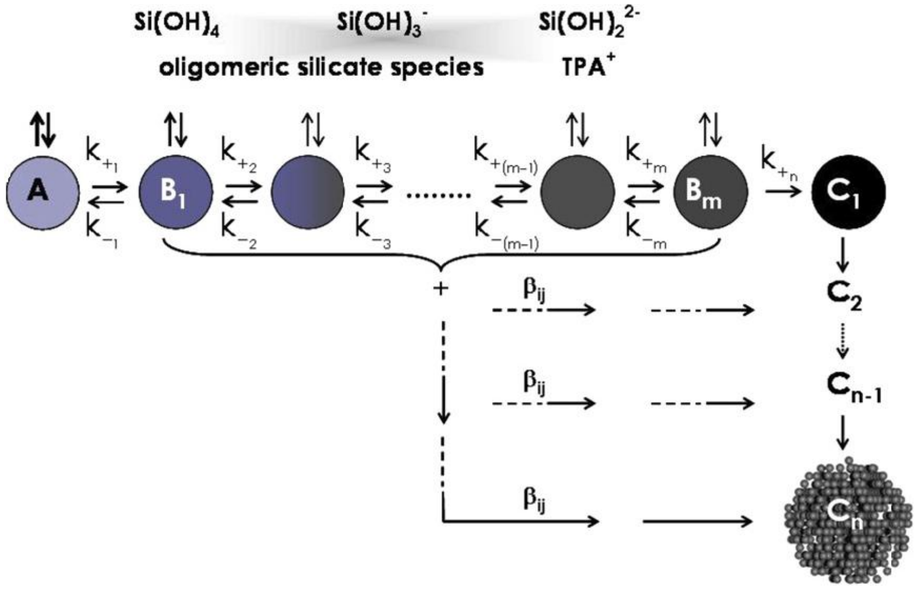

Figure 1-19. Schematic view of transformation of silica primary particles into zeolite nuclei and crystal growth by aggregation. (**A** represents primary particles, $\mathbf{B_i}$ is intermediate primary particles of age state i , $\mathbf{C_i}$ is crystal of size i, $\boldsymbol{\beta_{ij}}$ is coalescence rate constant between a particle of size i and size j, $\mathbf{k_+}$ and $\mathbf{k_-}$ are forward and reverse aging rate constantans, respectively.)[80]

Schoeman and his co-workers [83-86] reported the initial *in situ* dynamic light scattering (DLS) measurements on TPA-silicalite-1 crystallization at 70 °C, and the results are shown in Figure 1-20. Two particle populations can be observed, a suspension of colloidal silicate particles with nearly constant diameter of ~ 3.3 nm during the crystallization period studied, and larger particles with size approximately 10-12 nm, indentified as crystalline silicate and a linear growth rate of 0.72 nm/h. Similar particle populations in sililcate-1 synthesis solutions were also observed by de Moor et al. using as series of SAXS and WAXS despite of different Si: OH^- molar ratio and using "dimer" or "trimer" of TPA.[9, 64, 87] Nanoparticles of approximately 2.5 nm in size were detected before hydrothermal treatment, consistent with DLS measurements. Two additional populations approximately ~ 10 nm and above 50 nm appear after 1h heating. However, continued heating favors the growth of the 50 nm particles and both the 10 nm and 2.5 nm colloidal particles disappear. These observations suggested the connection between the disappearance of colloidal particles and the growing of the silicalite-1 nuclei could be the basis of zeolite nucleation. Nikolakis et al.[62] performed quantitative analysis of silicalite-1 crystal growth using DLVO theory which focused on electrostatic interactions between negatively charged surfaces on silicalite-1 and colloidal nanoparticles. This study described the experimental trends in particle growth rate at various temperatures and predicted the activation energies.[62] In addition, the physicochemical features of silicalite-1 surfaces was investigated through TPA adsorption using zeta potential measurements over a range of solution pH.[88]

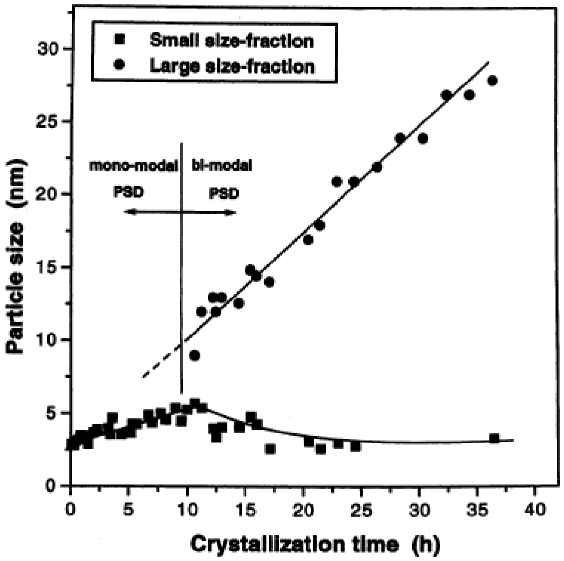

Figure 1-20. Particle size distribution as function of heating during crystallization of TPA-silicalite-1 at 70 °C.[85]

Given that zeolite growth mechanisms are synthesis parameter dependent, the growth kinetics can be varied by changes in temperature, silica content, solution alkalinity and ionic strength, among which temperature and alkalinity are the most profound parameters. Table 1-2 compared the activation energy obtained at various syntheses conditions yet the origin of the variation is not clearly understood.[89] Cundy et al. [90] investigated the temperature dependence of crystal growth rates along the (010) and (100) directions (see Figure 1-21), and the results were shown in Table 1-3. The resulting activation energies for length and width growth are 79 ± 1 and 62 ± 1 kJ/mol, respectively, indicating the crystallization is probably controlled by surface integration of growth species into the framework.

Table 1-2. Comparison of activation energies for TPA-silicalite-1 crystallization.[89]

	SiO_2: OH^-: TPA: H_2O^a			
	Si/OH	Si/TPA	Si/H_2O	Ea (kJ/mol)
deMoor et al.[87]	2.4	4.1	0.088	83
Twomey et al.[91]	2.3	2.8	0.055	96
Schoeman et al.[83]	2.8	2.8	0.05	42
Li et al.[92]	2.8	2.8	0.052	70
Watson et al.[57]	1.7	8.3	0.008	70
Nikolakis et al.[62]	4.4	4.4	0.004	90
Sano et al.[93]	10	10	0.003	48
Cundy et al.[90]	30	20	0.04	71
Feokitistova et al.[94]	16.7	10.1	0.04	55

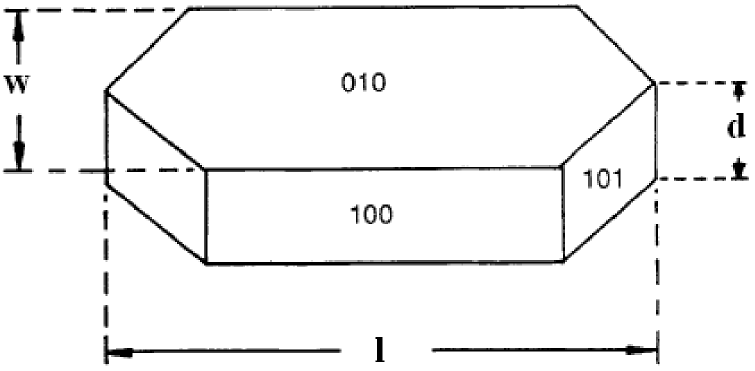

Figure 1-21. Idealized crystal morphology of silicalite-1.[90]

Table 1-3. * Growth rates for silicalite-1 at different temperatures.[90]

T/K	length-growth rate R_l/µm h^{-1}	width-growth rate R_W/µm h^{-1}
368	0.011	0.005
393	0.061	0.027
413	0.228	0.074
433	0.55	0.126
448	1.17	0.195

*Synthesis composition with molar ratio of 1Na_2O: 60 SiO_2: 3TPABr:1500 H_2O: 240EtOH.

In addition to kinetics of zeolite formation, thermodynamic aspects of zeolite formation rationalize driving forces for zeolite synthesis. Navrotsky and co-workers[95], performed detailed studies on formation enthalpies of zeolites respect to α-quartz, the thermodynamic stable phase. Despite that these values became more endothermic with decreasing framework density; the variation of enthalpies is slight compared with the wide range of pore diameters of zeolite studied. Zeolites studied are only 7-14 kJ/mol less stable than quartz in enthalpy and 3.2 – 4.2 J/K·mol above quartz in entropies.[96, 97] Furthermore, Piccione et al.[98] compared the Gibbs free energies of the interactions in several pure-silica zeolite frameworks and occluded organic SDA. Their results showed that the crystallization process is favorable and the energy values range from -1.1 to -5.9 kJ/mol SiO_2. Therefore, small energetic differences indicate that various kinetic pathways lead to the formation of zeolites. Also the SDA may play more of a kinetic role in selectivity of zeolite phases than stabilizing one phase with respect to the others.

1.5 Thesis Outline

The above studies provide valuable insight into growth mechanism of pure silica zeolite. Also interactions among primary colloidal particles, organic SDA and monomer species present in synthesis mixtures were identified and characterized by Burkett and Knight et al using ^{1}H-^{29}Si CP MAS NMR and ^{29}Si NMR techniques.[13, 14, 67, 99-101] However, few definitive statements of silica precursor particles and their association with the organic SDA can be drawn from these works. In contrast to most previous studies performed analyzing the silica species, i.e. inorganic phases, this thesis addresss these issues via investigating how organic SDAs participate in zeolite nucleation and quantifying their association with silica precursor particles. Given that the determination of the strength of organic-inorganic interactions in solution is not trivial, pulsed-field gradient (PFG) NMR provides a potential opportunity for studying this problems since it is non-invasive.[102] Chapter II describes the theoretical background and experimental procedures regarding PFG NMR as well as scattering techniques used for investigating silica species present in synthesis solutions. Chapter III investigates the formation of silica precursor nanoparticles in clear solution of TEOS-TAAOH-water and analyzed interactions of TAA cations with silica particles at room temperature with combined DLS and NMR methods. The Langmuir isotherm model was used to describe the organic-inorganic association at equilibrium. Chapter IV focuses on studying the behavior of TPA during early stages of silicalite-1 nucleation and determining TPA desorption kinetics. The effect of tetramethyl ammonium (TMA), as a competitive ion, on TPA-silica particles interaction at room temperature and elevated temperatures is discussed in Chapter V. The questions of how the colloidal stability of TAA-silica particles is affected by solution ionic strength and its ultimate effect on formation of the zeolite phase were addressed in Chapter VI. Also, the perturbation of TMA- and TPA-silica interactions in presence of salt induce particle aggregations were studied and compared in this chapter. Finally, Chapter VII summarizes important findings from these above chapters and outlined the areas for future work with respect to application of NMR methods in dynamic studies and technical basis for synthesizing pure silica zeolite nanocrystals.

CHAPTER II

EXPERIMENTAL METHODS AND SAMPLE PREPARATION

The main methods used in this thesis, along with their experimental details, are described in this chapter. Liquid-state NMR spectroscopy in general and pulsed-field gradient (PFG) NMR spectroscopy in particular, were heavily utilized to determine the organocation-silica interactions. Dynamic light scattering (DLS) and small-angle X-ray scattering (SAXS) were used to determine the size of the inorganic particles present in the mixtures.

2.1 Nuclear Magnetic Resonance (NMR) Spectroscopy

NMR was usedto capture the essential chemistry and dynamics of organic structure directing molecules in synthesis mixtures. Particularly, NMR parameters including chemical shifts, nuclear relaxation time and self-diffusion coefficients can be measured to obtain information about molecular structure and motion, binding energy and reaction kinetics. Before introducing advanced NMR methods, it is necessary to discuss the basic theory of generating NMR signal.

For a nucleus of spin I there are $2I+1$ possible orientations. For example, proton nucleus with spin ½ has two possible orientations. In the absence of an external magnetic field, the two orientations are of equal energy. When a magnetic field (B_o) is applied, the energy levels split into a two quantum magnetic states, i.e., $m_\alpha = -½$ against the field, and $m_\beta = ½$ aligned with the field, as shown in Figure 2-1. The energy difference (ΔE) between these two states can be described as

$$\Delta E = \frac{h\gamma B_o}{2\pi} \qquad (2\text{-}1)$$

where *h* is Planck constant (6.6261×10^{-34} Js), γ is the magnetogyric ratio (the value for ^{1}H is 2.6752×10^{8} rad s^{-1} T^{-1}) and B_o is the strength of the applied magnetic field. Furthermore, the ratio of nuclei population in the two energy levels is determined by the Boltzmann distribution. Thus, the number of nuclei at lower energy level (m_α) is slightly higher than that at higher energy level (m_β).

$$\frac{N_\beta}{N_\alpha} = e^{-\frac{\Delta E}{kT}} \qquad (2\text{-}2)$$

where N_α and N_β are the population of nuclei in lower (α) and higher energy level (β), respectively, *k* is Boltzmann constant (1.380×10^{-23} J/K).

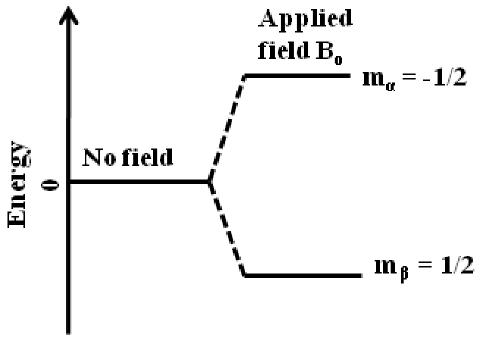

Figure 2-1. Energy levels for a ^{1}H nucleus with spin quantum number (I = ½).

Electromagnetic radiation of energy equal to ΔE could excite the nuclei at α spin level into β level in the magnetic field B_o, which is called the resonance condition. The frequency (ν) of the radiation can be calculated by

$$\nu = \frac{\gamma B_o}{2\pi} = \frac{2\mu B_o}{h} \tag{2-3}$$

where μ is the z-component magnetic moment of the nucleus, i.e., align with the quantization axis. Analogous to precession of a spinning mass in a gravitational field, the magnetic moment (μ) associated with a nucleus precesses in the applied magnetic field (B_o). This precession frequency is called Larmor frequency (ω_o) and is denoted as

$$\omega_o = \gamma B_o \tag{2-4}$$

Figure 2-2 illustrates the vector diagrams of proton magnetization behavior in a magnetic field (B_o). The vector **M** represents the vector sum of magnetization of proton α and β spins (see Figure 2-2 A). On the basis of the Boltzmann distribution, $\mathbf{M_z}$ of spins in the magnet is aligned with the B_o, along z-axis as shown in Figure 2-2 B. Since the system is at thermal equilibrium, no NMR signal can be observed. A secondary magnetic field is produced orthogonal to B_o via applying a radio frequency (RF) pulse along x-axis, a fractions of nuclei at α level are excited to the higher β level, thus **M** will shifts away from z-axis and toward y-axis, generating a vector component $\mathbf{M_{xy}}$ in xy plane.(see Figure 2-2C) After irradiation the spin system returns to equilibrium state ($\mathbf{M_z}$) in a process named relaxation, and $\mathbf{M_{xy}}$ precesses about B_o at the Larmor frequency (ω_o) which gives rise to the detected NMR signal by inducing a current in the coil surrounding the sample. The frequency difference between the induced signal and the RF pulse is called the Free Induction Decay (FID) as shown in Figure 2-2D. This time-domain signal includes all amplitude and frequency information of each resonance, and can be converted to frequency-domain NMR spectrum through Fourier Transformation (see Figure 2-2E).

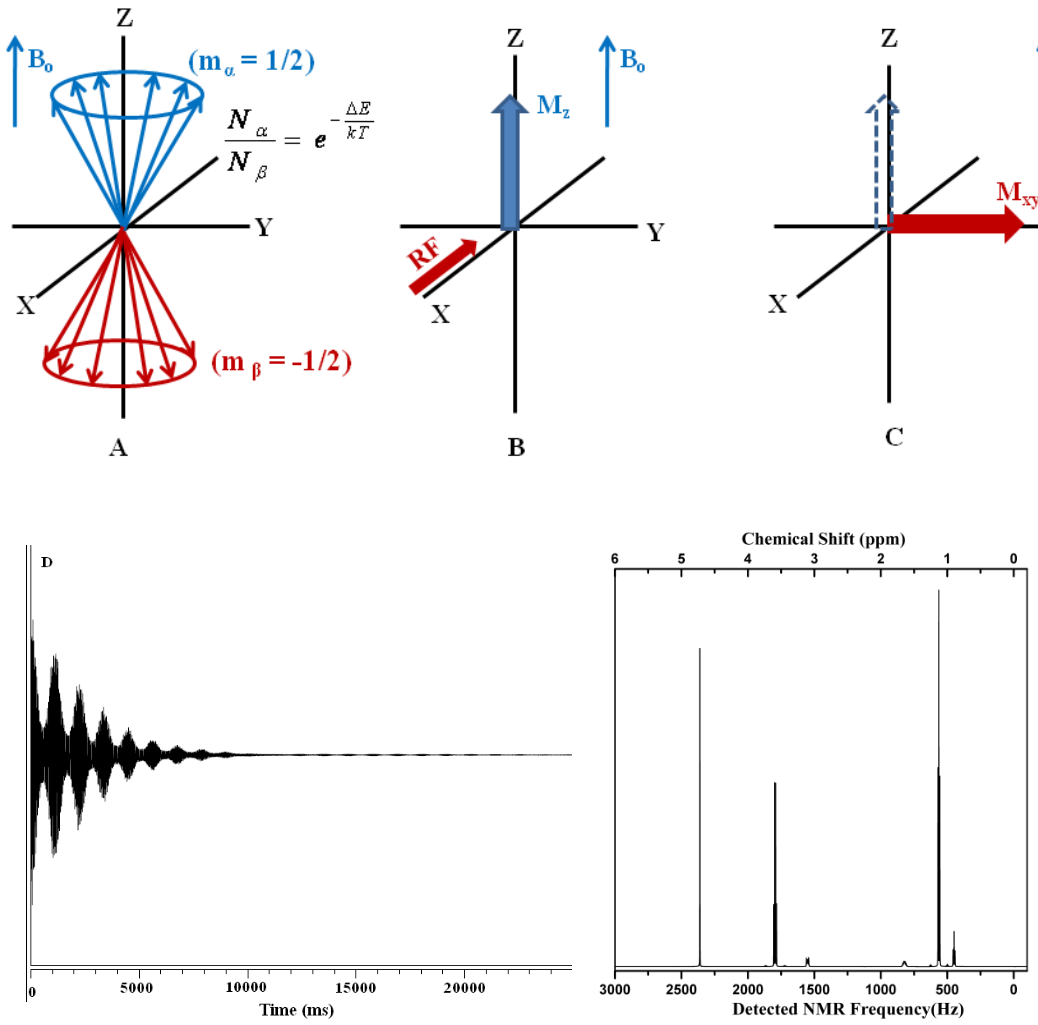

Figure 2-2. Vector diagram of magnetization pressing in applied magnetic field (B_o). (A) Two populations of spins alligned with B_o (α) and against B_o(β); (B) net magnetization $\mathbf{M_z}$ along z-axis due to excess of spin in lower level (α); (C) Transition of $\mathbf{M_z}$ to $\mathbf{M_{xy}}$ via application of 90^o radio-frequencey pulse along x-axis; (D) A free induction decay (FID) of TPABr-Ethanol-water mixtures in this study and (E) the corresponding NMR spectra generated through a Fourier Transformation of the FID in shown in D. (The detected frequencies (in Hz) for ^{1}H are already referenced against DSS (4,4-dimethyl-4-silapentane-1-sulfonic sodium)). Chemical shift with unit of ppm is defined as detected frequency divided by frequence of the spectroscopy, which is 500 MHz in this study.) ((A), (B) and (C) are adopted from the reference [103].)

2.2 Relaxation NMR

As shown in Figure 2-2 C, after the RF pulse, the excited magnetization relaxes back to the thermal equilibrium along z axis. This relaxation process is determined by two components in absence of chemical exchange. The first is spin-lattice relaxation which involves the transfer of excited spins to their surroundings. The intensity of the magnetization during the spin-lattice relaxation can be described as:

$$I_Z(t) = I_o[1 - \exp(tR_1)] \qquad \text{(2-5a)}$$

$$R_1 = \frac{1}{T_1} \qquad \text{(2-5b)}$$

where I_Z and I_o are the intensity at time t following the pulse and at equilibrium, respectively. R_1 is the first-order rate constant at which the spins return to equilibrium along z or longitudinal axis. T_1 is the relaxation time constant.

The second component is the relaxation of the bulk magnetization in the transverse (xy) plane after the RF pulse, leading to the dephasing of magnetization in this plane. This relaxation is called spin-spin (or transverse) relaxation, which involves the transfer of excess energy between the individual spins, and occurs simultaneously with spin-lattice relaxation. The intensity change during the transverse relaxation can be explained by

$$I_{xy} = I_o \exp(-tR_2) \qquad \text{(2-6a)}$$

$$R_2 = \frac{1}{T_2} \qquad \text{(2-6b)}$$

where I_{xy} and I_o are the intensity of the magnetization at time t following the pulse and of the equilibrium magnetization. R_2 is the rate constant for spin-spin relaxation and T_2 is corresponding relaxation time constant. T_2 relaxation time constant cannot be larger than the T_1 relaxation time constant. In addition, the effective transverse relaxation time (T_2^*) is a combination of T_2 and magnetic field inhomogenity. In a perfect homogenous magnetic field, T_2^* is equal to T_2, whereas T_2^* is shorter than T_2 when the field is inhomogeneous. Furthermore, the width of a NMR resonance at half-height ($w_{1/2}$) is inversely proportional to the value of T_2^*.

$$T_2^* = \frac{1}{\pi w_{1/2}} \tag{2-7}$$

According to the above equation, the resonance of a nucleus gets broadening as the corresponding T_2 relaxation time decreases. The increase in resonance width usually occurs when observing binding behavior. For example, tetrapropylammonium (TPA) bind to colloidal particles in solution. TPA in solution has a T_2 of 0.31 s. The binding of TPA onto silica particles in solution is manifested by decrease in T_2 to the value of 0.025s. The measurement of T_1 and T_2 are described in subsection 2.5.1.

2.3 Pulsed-field Gradient (PFG) NMR

One of the many capabilities of NMR is the ability to spatially label nuclear spins by applying magnetic field gradients to the sample. This ability leads to the possibility of measuring self-diffusion coefficients of molecules in solution. PFG NMR was developed based on NMR pulse sequences to measure the translational self-diffusion coefficient of molecules via labeling their nuclear spins in a spatially varying magnetic field by applied gradient pulses.[103-106] Conventional techniques for diffusion measurements including light and neutron scattering, fluorescence, and zero-length chromatography often have detection limitations on sample concentration range and can be invasive in nature. PFG NMR, while having its own limitations is ideally suited for the current work as it is non-invasive and given the high-number of protons per organocation is sufficiently sensitive even at millimolar concentrations of organocation.[107] Furthermore, it provides complementary information to mutual diffusivity obtained from scattering techniques.[108] Of relevance to the current work PFG NMR has been applied for studying weakly interacting host-guest systems via separating different species in such systems based on their different diffusion coefficients (i.e. the ability to discern a 'free' and a 'bound' state). Particularly, the method has been used successfully to describe small molecule binding in macromolecular systems even when resonances assignments of the macromolecule are unknown.[109-115] Given the difficulties of investigating the organocation during zeolite synthesis it was determined to use PFG NMR to probe organocation-silica interactions.

2.3.1 Measuring Self-Diffusion with Magnetic Field Gradients

Random translational motion, i.e, Brownian motion of molecules or ions, is called self-diffusion which is the most fundamental form of transport and characterized by the self-diffusion coefficient (D_S). Such diffusion can be described by Debye-Einstein theory and obtained by the following equation .[116]

$$D_S = \frac{k_B T}{f} \tag{2-8}$$

where k_B is the Boltzmann constant, T is temperature, and f is the friction coefficient. For the case of spherical diffusing species with an effective hydrodynamic radius (R_H) in a solution of viscosity (η), the friction coefficient (f) is given by

$$f = 6\pi\eta R_H \tag{2-9}$$

Generally, the friction coefficient can be modified by including the factors such as molecular shape, hydration.[104] The self-diffusion coefficient provides information on the molecular interaction and structural properties of the diffusing species under study. It is also known the average displacement of a molecule due to thermal motion,$<l^2>$, in isotropic medium can be related to the diffusion time t, by the Einstein relation. [117]

$$< l^2 >= 6D_S t \tag{2-10}$$

For non-isotropic media the self-diffusion (D_S) must be replaced by the diffusion tensor $\mathbf{D_S}$. [117] The average displacement plays a central role in the interpretation of NMR-based diffusion studies.

In principle, nuclear spins can be labeled by a well defined magnetic field gradient, and thus diffusion coefficients can be calculated from the echo attenuation if the amplitude (g) and duration (δ) of the magnetic field gradient are known. Typically, a field gradient is generated by passing current through a coil wound across the sample. The resulting gradient with amplitude **g** can be described by:

$$g = \frac{\partial B_x}{\partial x}\hat{i} + \frac{\partial B_y}{\partial y}\hat{j} + \frac{\partial B_z}{\partial z}\hat{k} \tag{2-11}$$

where $\hat{i}, \hat{j}, \hat{k}$ are unit vectors in the x, y, z directions, respectively. Here the z-direction is defined by the direction of $\boldsymbol{B_0}$ and we are concerned with gradients in the *z* direction.[102] The original diffusion NMR measurement was a simple modification of the Hahn spin-echo pulse sequence (see Figure 2-3), developed by Stejskal and Tanner.[118] As shown in Figure 2-3(top), after the first 90° radio frequency (RF) pulse along *x* the axis and a short delay (t_1), the applied z-direction gradient pulse encodes nuclear spins along the length of sample. Such spatial encoding occurs since the nuclei precess at different frequencies due to their different positions in the applied field gradient (g). Following that a delay (τ) allows the magnetization to undergo precession in the *xy* plane. Then a 180° RF pulse is applied along the y axis, which reverses the direction of the precession. The magnetization refocuses along –y axis at the end of the second τ delay. This refocused magnetization is termed as an 'echo'. During this delay period (τ), a second identical gradient pulse is applied along the sample, which spatially decodes the spins. As a result, a spin echo is generated at a time of 2 τ after the first $90°_x$ pulse, and the NMR signal is acquired. The PFG NMR experiment exploits that due to Brownian motion the molecules in the system move during this process. Thus the nuclei do not experience the same gradient strength from the second gradient due to motion. This leads to incomplete focusing of the echo. Moreover, the signals observed, i.e. the extent of signal attenuation, can be readily related to the rate of motion. Since large molecules diffuse more slowly, less attenuation of the NMR signal occurs.[103] However, the diffusion time (Δ) of PGSE sequence which allows a molecule to diffuse before coherence is limited by the Spin-Spin relaxation time (T_2),i.e. $\Delta \leq T_2$. This constraint restricts the size of molecules that can be measured using this pulse sequence. To circumvent this limitation one can use the pulsed-field gradient stimulated echo (PFG-STE) [119] which stores the magnetization along the negative z-axis during the diffusion time (Δ), in contrast to the PGSE sequence where the magnetization is stored in the xy plane during the diffusion period (Δ). Thus the PFG-STE experiment, shown in Figure 2-3(bottom), produces echoes whose attenuation are limited by the Spin-Lattice relaxation (T_1), which is usually longer than T_2, and eliminates the dephasing of magnetization due to spin-spin coupling.

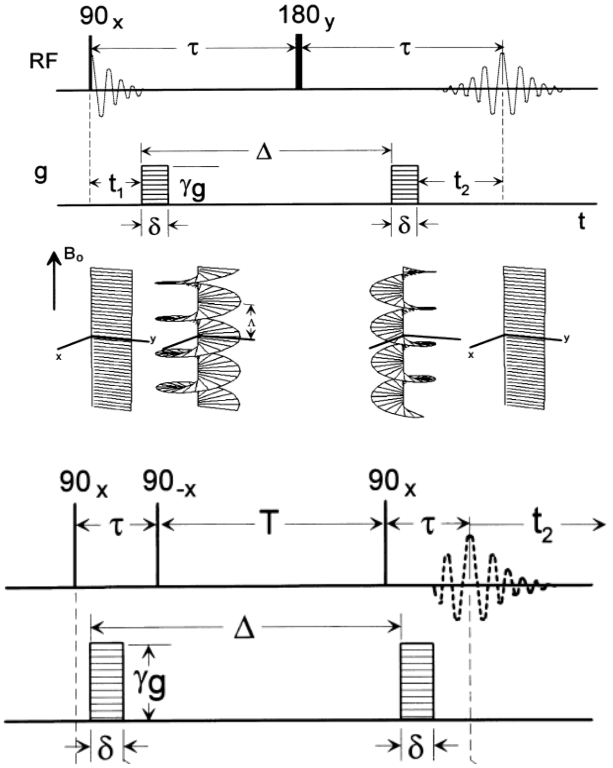

Figure 2-3. (Top) A schematic view of how the Stejakal and Tanner (or Pulse Gradient Spin Echo) pulse sequence measures diffusion. (Bottom) Hahn stimulated echo (STE) with pulsed field gradients. [102]

Another noteworthy issue is the eddy current induced by the short gradient pulse (*g*), which is required to dissipate before the NMR signal can be acquired. One of the best ways to minimize these currents is to replace the gradient pulse by a pair pulse of different polarity separated by a 180°RF pulse. The composite bipolar gradient STE pulse sequence is shown in Figure 2-4.

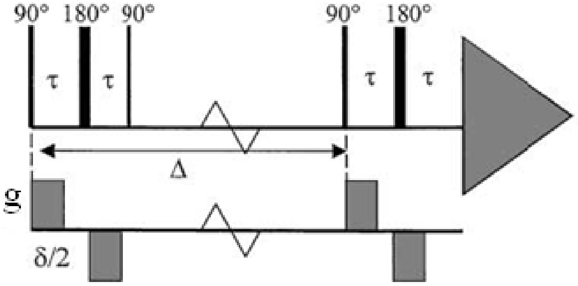

Figure 2-4. Bipolar-pulse pair stimulated each (BPPSTE) pulse sequence. [120]

Typically PFG NMR measurements are performed by acquiring a series of spectra with systematically increased the gradient amplitudes. Figure 2-5 (top) shows a PFG NMR stack spectra of tetrapropylammonium (TPA)-ethanol-water mixtures acquired with the BPPSTE sequence shown in Figure 2-4. As can be seen in Figure 2-5 (top), the resonances assigned to water (4.7ppm), ethanol (3.6 and 1.2 ppm) and TPA (3.1, 1.7 and 0.9 ppm) attenuate as the gradient strength increases yet with different attenuation rates. Particularly, the self-diffusion coefficient of TPA (0.9 ppm) is obtained by monitoring the TPA signal intensity as a function of the squared gradient amplitude (g^2). For the BPPSTE sequenced used the signal decay is given by

$$I = I_o \exp[-D_S \gamma^2 \delta^2 (\Delta - \frac{\delta}{2} - \frac{\tau}{3}) g^2] \qquad (2\text{-}12)$$

where γ is the magnetogyric ratio, g is the gradient strength or amplitude (G/cm), Δ the diffusion time between gradient pulses, and τ is the time between the gradient pulse and the following RF pulse shown in Figure 2-4. I and I_o are the NMR peak heights and the value at initial gradient strength. Accurate D_s measurements require attenuation of signal intensity to 10 % of the value obtained at the initial gradient strength. The exponential decay fit based on equation (2-12) to the TPA signal attenuation yields a diffusion coefficient of 4.28×10^{-10} m^2/s. Also shown in Figure 2-5, the intensity of ethanol (1.2 ppm, $Ds = 7.21\times10^{-10}$ m^2/s) shows a larger decay slope than that of TPA, since ethanol has a smaller molecular size and thus diffuses more quickly than TPA. This simple numerical analysis, as performed for the data in Figure 2-5, is effective if resolved resonances are available for each component in the sample, or if the diffusion coefficients of overlapped resonances differ significantly. However, alternative analysis methods are required for analysis of complex mixtures, where resonances are highly overlapped and/or the difference in diffusion coefficients is small.

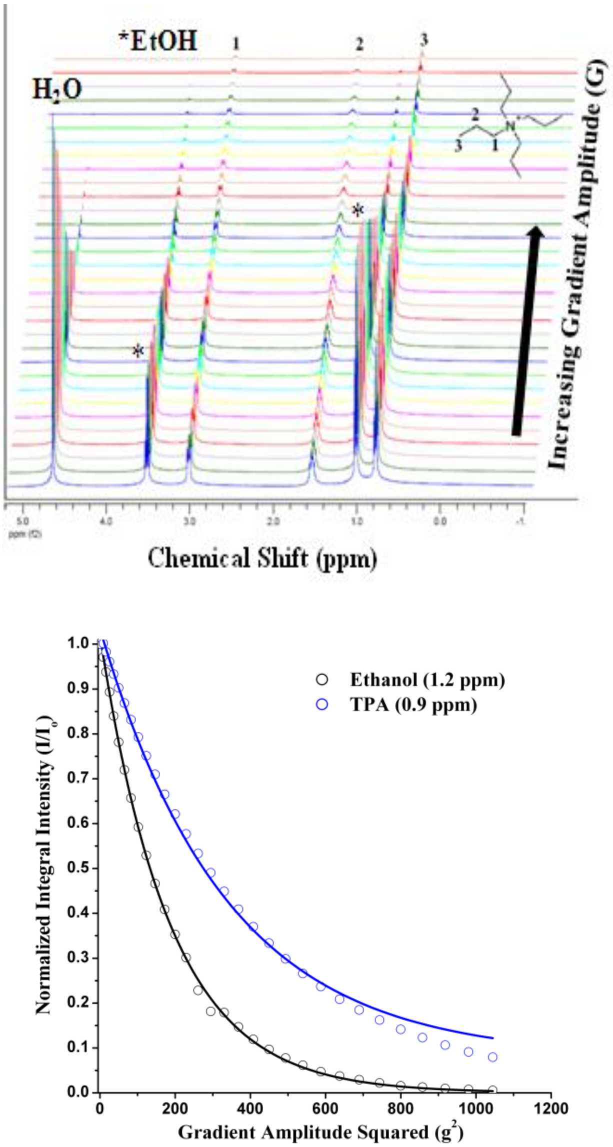

Figure 2-5. (Left) ^{1}H PFG NMR stack spectra of a TPA-ethanol-water mixture collected with the BPPSTE sequence. (Right) The normalized integral intensity of TPA and ethanol plotted against the square of the gradient amplitude.

2.3.2 Two-Dimensional Diffusion Ordered NMR Spectroscopy (DOSY)

The PFG NMR data set can be visualized as two-dimensional spectrum called <u>D</u>iffusion <u>O</u>rdered <u>S</u>pectroscop<u>y</u>, or DOSY, via user selected transformations that display conventional chemical shift spectra in one dimension and corresponding ‘diffusion spectra’ based on molecular diffusion rates in the other dimension. [105, 106] The general DOSY data processing scheme is shown in Figure 2-6. The NMR spectra are obtained by a Fast Fourier Transformation (FFT) of FID data in the time domain to frequency domain of chemical shift, as shown in Figure 2-2D. The core of DOSY processing is the transformation and display of diffusion data in the second spectral dimension. The PFG NMR experiment provides a data set [102, 106]

$$I(K, v_m) = \sum_n A_n(v_m) \cdot \exp[-D_n(\Delta - \delta\varepsilon)\mathrm{K}^2] \tag{2-13}$$

where $K = \gamma g \delta$ and the value of ε depends on the shape of the gradient pulse. $A_n(V_m)$ is the amplitude of the 1D NMR spectrum for the n$^{\text{th}}$ diffusing species when g is close to zero and D_n is the corresponding diffusion coefficient. According to equation (2-10), each frequency (v_m) of the NMR spectrum has a 1D data set that is described by a sum of exponential components with K^2 as the independent variable. Thus, at a given frequency (v_m), the 1D date set I (K) describing the attenuation of the peak at v_m can be described as

$$I(K^2) = \int_0^\infty \alpha(\lambda) \exp(-\lambda K^2) d\lambda \tag{2-14}$$

where $\lambda = D_n(\Delta - \delta\varepsilon)$ and $\alpha(\lambda)$ is the ‘spectrum’ of the diffusion coefficient. The decay function $I(K^2)$ obtained by PFG NMR is the Laplace Transformation of $\alpha(\lambda)$. Therefore, $\alpha(\lambda)$ can be calculated via Inverse Laplace Transformation (ILT) of the decay function $I(K^2)$ (see Figure 2-6 as an example). However, in contrast to FT which suffices to yield a unique spectrum in the absence of truncation errors, ILT is an ill-conditioned problem and may be completely intractable. In some cases, even if solutions for $\alpha(\lambda)$ can be found that are consistent with $I(K^2)$ they are usually not unique. Thus, prior knowledge for the sample under study may be essential for limiting the range of solutions as well as obtaining the most likely diffusion spectrum.

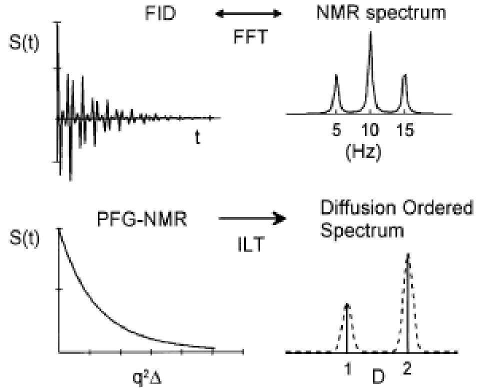

Figure 2-6. DOSY data processing by Fast Fourier Transformation (FFT) and Inverse Laplace Transformation (ILT). [102]

Figure 2-7 shows the transformation of a PFG NMR stack plot of Tetrapropyl ammonium (TPA)-Tetramethylammonium (TMA)-silica mixture to a DOSY plot, which is associated with Figure 2-6. The details of data inversion process by means of various computer algorithms are well documented in the literature. [102, 121, 122]

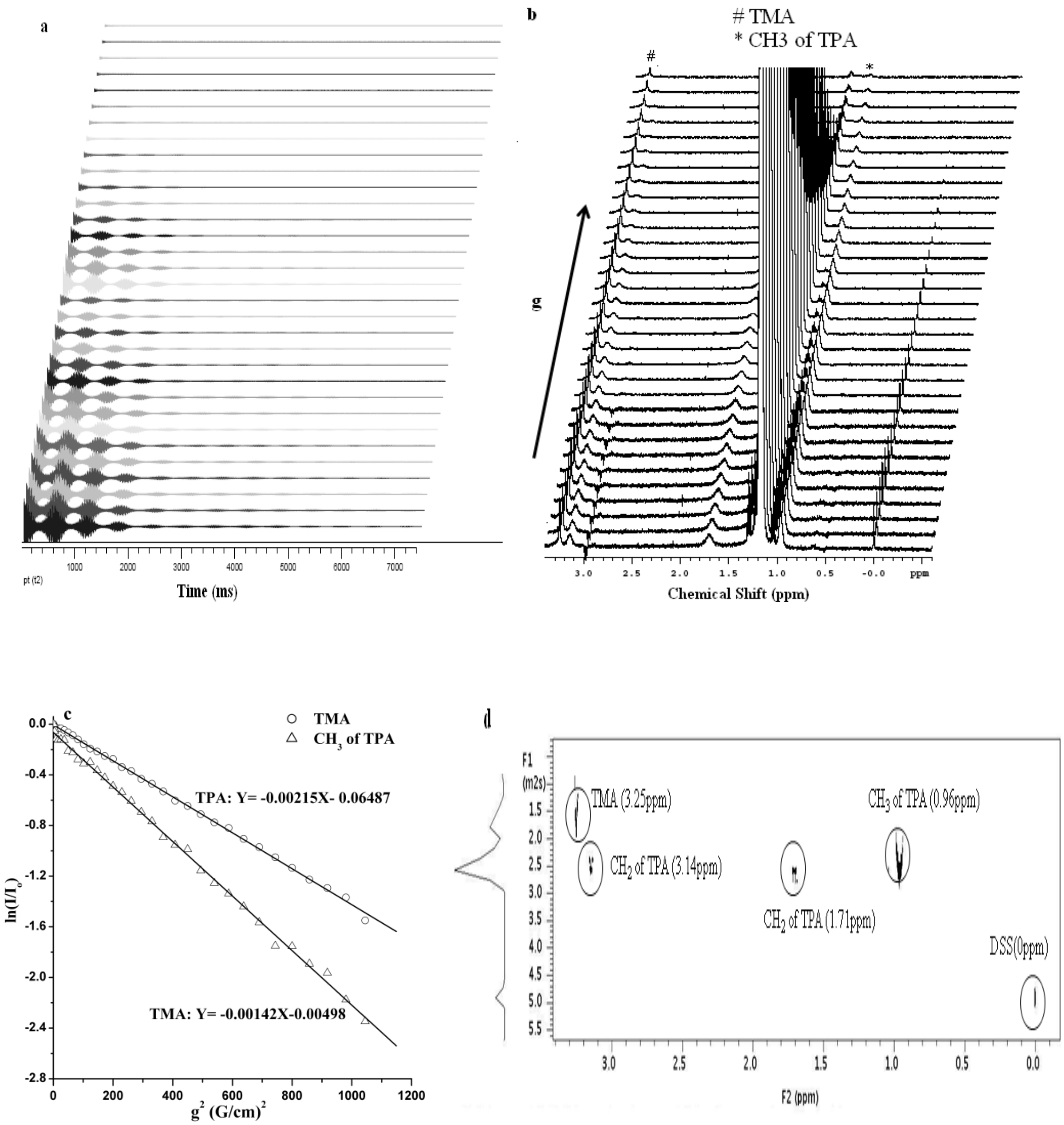

Figure 2-7. (a) PFG NMR stack FIDs of TPA-TMA-silica mixture as a function of gradient amplitude and (b) corresponding stack NMR spectra obtained via FFT. (c) NMR intensity decay plot obtained from (b), and (d) corresponding DOSY contour plot obtained by ILT. (For clarity, signal from water and ethyl group of ethanol are not shown.)

2.3.3 Exchange Effects in Diffusion NMR Experiments

Numerous studies have been performed on chemical exchange processes using NMR methods.[123-125] The exchange rates, i.e. inverse lifetimes, can be manipulated by changes in temperature and concentrations for intermolecular reactions. In diffusion NMR the variable is gradient strength and duration ($g\delta$), rather than time, thus no analogue of lifetime broadening exists in the diffusion dimension.[125, 126] However, chemical exchange can potentially influence the observed PFG NMR results. Consider a system where a nuclear spin can stay in two separate environments with the same Larmor frequency (ω_o) and can migrate from one site (A) to the other (B). If exchange between the two sites is comparable to the diffusion time scale, the normalized intensity decay of the spin is a superposition of the exponential functions associated with each site. [127]

$$I(x) = p_A \exp(-x\alpha_A) + p_B \exp(-x\alpha_B) \tag{2-15}$$

where $x = \gamma^2 g^2 \delta^2 (\Delta - \delta\varepsilon)$, α_A and α_B are apparent decay constants containing information about the diffusion coefficients D_A and D_B, respectively. p_A and p_B are the apparent fractions of each site.

If the two-site exchange is fast compared to the diffusion time scale, equation (2-12) become a single exponential decay with a mean diffusion coefficient (D_M)

$$D_M = f_A D_A + f_B D_B \tag{2-16}$$

where f_A and f_B are the true molecular fractions in sites A and B. This suggests that the observed diffusion coefficient is a weighted average of the respective diffusion value in either site.

If the molecular exchange between the sites is slow compared to the relevant experimental time scale, the normalized PFG-NMR intensity decay can be written as a sum of the corresponding signal decay of both sites

$$I(x) = p_A \exp(-D_A x) + p_B \exp(-D_B x) \tag{2-17}$$

Also the influence of relaxation occurring during the delays (τ) in the STE pulse sequence (see Figure 2-1) needs to be considered. Thus, the apparent fractions in diffusion experiments are described by

$$p_A = f_A \exp[-(\frac{2\tau}{T_2} + \frac{\Delta - \tau}{T_1})] \tag{2-18}$$

where T_2 is the spin-spin relaxation time and T_1 is spin-lattice relaxation time which can be obtained by NMR relaxation measurements shown in the following subsections. Experimental results of exchange effects on PFG NMR results for TPA-silica and TMA-silica mixtures are shown subsection 3.3.2.

2.4 Dynamic Light Scattering (DLS)

DLS measures scattered light intensity changes at a fixed angle as a function of time. The thermal motion of the species in solution scattering light causes such time-dependent fluctuations. In this study, DLS measurements are performed under dilute concentration of silica nanoparticles to avoid multiple scattering. The single-scattered light was collected and characterized with an autocorrelator to generate a first-order autocorrelation function (ACF). For monodisperse spherical particles this can related to the diffusion coefficient by

$$g^{(1)}(\tau) = \exp(-Dq^2\tau) \tag{2-19}$$

where D is the diffusion coefficient of particles, q is the magnitude of scattering vector defined as:

$$q = \frac{4\pi n}{\lambda}\sin(\frac{\theta}{2}) \tag{2-20}$$

where n is the refractive index of the media, λ is the wavelength of the laser beam, and θ is the scattering angle (typically 90°). The diffusion coefficient (D) is related to the hydrodynamic radius (R_H) of the particles using the Stokes-Einstein equation assuming particle-particle interactions can be neglected for dilute solution.

$$R_H = \frac{k_B T}{6\pi\eta D} \tag{2-21}$$

This relation is consistent with equation 2-5 and equation 2-6. The autocorrelation function can be fitted by various algorithms to generate the mean particle size or size distribution. [128, 129]

2.5 Experimental Aspects

2.5.1 NMR Measurements

All NMR experiments in this thesis were performed on a Varian INOVA 500 MHz spectrometer equipped with a 5 mm broadband indirect detection probe and a z gradient coil (up to 32 G/cm). The temperature was regulated at 25 °C for all experiments and the temperature calibration was performed with methanol. Chemical shifts are reported relative to an internal reference of DSS at 0 ppm (sodium 2, 2-dimethyl-2- silapentane-5-sulfonate, Cambridge Isotopes). Approximately 500 μL of mixture was added to the 5-mm tube (Wilmad Labglass). The samples were allowed to thermally equilibrate for at least 15 min prior to analysis.

^{1}H PFG NMR experiments were carried out with static samples, using the BPPSTE sequence shown in Figure 2-2. The 90° pulse length was typically 7 to 9 μs. The gradient strength (g) was varied from 1 G/cm to 25, 30, or 32 G/cm. The bipolar pulse gradient duration (δ) was 2 ms (1 ms duration of individual pulses), the gradient recovery delay (τ) was 300 μs, and the diffusion period (Δ) was varied from 200 ms to 1s in order to attenuate the signal intensity to less than 10 % of the value obtained at 1 G/cm. At least 16 transients were collected for each increment step with a relaxation delay of 4 s. The field gradient strength was calibrated by measuring the value of self-diffusivity (D_s) of 10 mol % H_2O in D_2O (99.96% D atom, Cambridge Isotopes), D_s = (1.92 ± 0.06) × 10^{-10} m^2/s at 25 °C. [130] For the BPPSTE pulse sequence the resonance intensity (I) is related to the self-diffusion coefficient (D_s) described by equation 2-5. DOSY processing was used to resolve the overlapping resonances and was performed with the Varian VNMR, VnmrJ operating system. The sweep width of the attenuated stack spectra was manually adjusted to approximately 3-4 kHz for data storage purposes. In the 1H dimension, the free induction decays (FIDs) were zero filled to 32767 data points and processed with a decaying exponential apodization function equivalent to 0.2 Hz line broadening. A total of 128 complex increments were used in the diffusion dimension (plot of peaks corresponding to their diffusion coefficient values). Peak heights were utilized as signal intensity (I) in the analyses.

Spin-lattice relaxation time (T_1) measurements were determined using inversion recovery experiments [180^o_y - τ -90^o_x - Acq]. Spin-spin relaxation (T_2) measurements were performed with the Carr-Purcell-Meiboom-Gill (CPMG) pulse sequence, [$90°_x$-τ-($180°_y$-2τ)$_n$-Acq], which utilizes a 180° pulse train to attenuate signals from relaxing species. [113, 131 132] The T_2 delay (τ) is set to 1 ms and a half-echo was recorded every $4n\tau$. The relaxation delay was 20 s and the number of scans per sample was 4 or 16. When the experimental conditions were such that the signal-to-noise was poor (e.g., samples with very dilute concentration, long diffusion delay time (Δ), long pulse train length ($4n\tau$)), the spectra were carefully examined to include only clearly identifiable peaks.

2.5.2 DLS Measurements

The DLS experiments were performed with a BIC ZetaPALS with a BI-9000AT correlator. The wavelength of the incident laser beam (λ) was 660 nm and the detector angle (θ) was 90°. To eliminate any dust, the tested samples were filtered by using a 0.2 μm PES syringe filter (Corning Co.) prior to loading into the cuvette (VWR). For each sample, three measurements were performed and the elapsed time was 5 min to ensure good signal-to-noise. The sampling and analysis were carried out in the self-beating mode. The delay time increased from 2 μs to 20 ms and the measurement temperature was 25 °C. The intensity autocorrelation functions were analyzed with the non-negative constrained least-squares method (NNLS). NNLS fitting yields a particle size distribution for polydisperse and the largest population is set to 100%. Given the level of dilution in these mixtures (approximately 1.3 vol % silica in the C4 mixture) particle-particle interactions can be reasonably neglected. Thus to a reasonable first approximation the translational diffusion coefficient measured is approximately equal to the self-diffusion coefficient (D_s), which can be related to the particle hydrodynamic radius (R_H) via the Stokes-Einstein equation (2-14). The viscosity of the solution (η), is taken to be that of deuterated water (1.097 cP at 298 K). [133]

2.5.3 pH and Conductivity

Solution pH values were measured using a Fisher Scientific AB15/15$^+$ pH meter and an Accument glass body Ag/AgCl reference electrode (Pittsburgh, PA, USA). The pH meter was calibrated with standard pH7 and 10 buffer solutions. (Ricca Chemical Co.). Solution conductivity of was determined with a VWR model 2052EC meter, and the conductivity meter was tested on KCl standards at conductivity values of 700µS/cm.

2.5.4 Viscosity

Viscosity measurements were performed using a precalibrated tube viscosity meter (viscometer constant is 0.005095 cSt/s) emerged in a water bath and the measured values are averaged over total six measurements.

2.5.5 X-ray Diffraction (XRD)

Powder XRD measurements were performed on a Rigaku MiniFlex II (Cu KR radiation) in reflection mode from $2\theta = 5$ to $40\ ^{o}$ with a step size of 0.02^{o} and 2s per step.

2.5.6 Small Angle X-ray Scattering (SAXS)

SAXS measurements were performed using a Bruker-AXS Rotating-Anode NANO-STAR Small Angle X-ray Scattering Instrument with Cu Kα radiation (1.5417 Å). The sample was loaded into a 1-mm diameter Anton Paar quartz capillary and measured at 25 °C. The sample to detector distance 64 cm, corresponding to a q range of 0.02-0.3 $Å^{-1}$. The exact sample to detector distance was determined using a silver behenate standard. For obtaining the transmission coefficient of the sample, a piece of glassy carbon was inserted into the beam path as a second specimen after each measurement. The scattered intensity of the particles was calculated based on using water as the reference material for the background subtraction in data analysis.

2.5.7 Thermogravimetric Analyses (TGA) and Scanning Electron Microscopy (SEM)

TGA were performed using a NETZSCH TG 209 with a heating rate of 5 K/min from 298 to 973K under mixed O_2/N_2 environment. The O_2 and N_2 flow rates were 10 mL/min and 15 mL/min, respectively. Field emission SEM measurements were performed with a JEOL JSM-7500 microscope operating at 5 kV.

2.6 Materials

All compounds used in the thesis work were used as received. Tetramethylammonium hydroxide (TMAOH, 25% w/w), tetraethylammonium hydroxide (TEAOH, 35% w/w), tetrapropylammonium hydroxide (TPAOH, 40% w/w), tetrabutylammonium hydroxide (TBAOH, 40% w/w), and tetramethylammonium bromide (TMABr, 98%) were purchased from Alfa Aesar. Tetrapropylammonium bromide (TPABr, 98%) was purchased from Aldrich. Tetraethyl orthosilicate (TEOS, > 99%) was purchased from Fluka. Sodium hydroxide (NaOH, 99%) was purchased from BDH Chemicals. Ethanol (CH_3CH_2OH, > 99.5%) was purchased from Acros Organic.

Lithium chloride (LiCl, 99%) and cesium chloride (CsCl, 99%) were purchased from Alfa Aesar. Sodium chloride (NaCl, 99%) was purchased from EMD Chemicals. Deuterium oxide (D_2O, 99.96% D, Cambridge Isotopes) and sodium 2,2-dimethyl-2-silapentane-5-sulfonate (DSS) was used as received.

2.7 Sample Preparation

2.7.1 Samples Tested prior to Heating

Two different preparation methods were used to formulate the mixtures investigated. For one set of experiments it was desired to prepare samples of varying silica content at fixed TAAOH concentration. In this case solutions of molar composition 9TAAOH: xSiO$_2$: 9500H$_2$O: 4xEtOH (x varied from 0 to 120) were synthesized in two steps. First, the desired TAAOH was added to deionized water and the mixture was stirred for approximately 1 h. Then TEOS was added to the mixture, and the resulting solution was stirred for a minimum of 12 h to ensure the complete hydrolysis of TEOS. The solutions used for NMR measurements were prepared following the method above, but instead with deuterated water. To make a comparison with hydrolyzed TEOS solutions, mixtures with the equivalent amount of water and ethanol were prepared by first diluting TPAOH in deuterated water and then adding the desired amount of ethanol to yield a final composition of 9TPAOH: 4xEtOH: 9500D$_2$O (x =20-120).

The other series of samples with fixed silica content but varying the TAA content were prepared as follows. NaOH was dissolved in deuterated water, and TEOS was added to give a mixture composition of 9NaOH: *x* SiO_2: 9500D_2O: 4*x* EtOH (*x*= 0, 5, 20, 40, 80). These above solutions were stirred for at least 12 h to allow complete hydrolysis of TEOS, and are hereafter denoted as C0-C4 shown in Table 2-1. The viscosity of C0-C4 mixtures were also shown in Table 2-1. Increasing amount of TPABr or TMABr was added to these silica solutions, and the resulting mixtures are denoted as *y* TAA/C0, C1, C3, C4 (TAA= TMABr, TPABr; *y* was increased from 0.25 to 36). The compositions were chosen as they are representative of those used in silica precursor particle studies [62, 73] and silicalite-1 growth experiments.[78] Sodium hydroxide was used to set the solution initial pH when varying the TAA cation concentration, and thus control the nanoparticle formation. All samples used for NMR measurements were allowed to equilibrate for a minimum of 24 h before measuring.

Table 2-1. Mixture compositions and viscosity of silica solutions investigated.*

Sample	Composition	Viscosity (cp)
C1	9NaOH:5SiO_2:9500H_2O: 20EtOH	0.947 ± 0.037
C2	9NaOH:20SiO_2:9500H_2O: 80EtOH	0.980 ± 0.004
C3	9NaOH:40SiO_2:9500H_2O: 160EtOH	1.063 ± 0.003
C4	9NaOH:80SiO_2:9500H_2O: 320EtOH	1.296 ± 0.014

*SiO_2 was added as TEOS.

2.7.2 Samples Subjected to Heating

TPA-silica mixtures with molar compositions of 9NaOH: *x* TPABr: 40SiO_2: 9500 D_2O: 160 EtOH (*x* = 0.25, 0.5, 0.75, 1.0, 1.5, 3.0) were prepared as described in the above subsection 2.6.1, and are denoted as *x* TPA/C3. These TPA-silica mixtures were then placed in screw cap Teflon containers and heated at 90 °C. Particularly, 0.5 TPA/C3 sample were heated at 70, 90, and 100 °C to study the effects of heating temperature. Aliquots were taken from the above heated mixtures that were quenched at different time intervals. Despite that these experiments are not formally *in situ* measurements, the particle structure becomes more stable over time at elevated temperatures, which is irreversible, and thus the measurements are expected to capture the key feature of interest in the current work (TPA-silica interactions).

x TPA/C3 (*x*= 0.5, 1.5, 3.0, 9.0) mixtures were prepared as described above but in protonated water, and heated at 90 °C for two weeks. Nanosized silicalite-1 crystals were synthesized as a reference material as follows.[134] TPAOH was mixed with deionized water, and the desired amount of TEOS was added to yield a molar composition of 9 TPAOH: 25 SiO_2:1450 H_2O: 100 EtOH. This solution was stirred for 24 h at room temperature and placed into a sealed, Teflon-lined autoclave heated at 100 °C for 2 days. The collected solids from the above two mixtures were removed from their mother liquid by centrifugation at a rate of 13 000 rpm, washed with distilled water until pH = 7-8, and then dried overnight at 40 °C before being subjected to further characterization.

.

2.7.3 Samples with Mixed Organocations

TMA-TPA-silica mixtures with molar compositions of 9NaOH: y TPABr: *x* TMABr: 40 SiO_2: 9500 D_2O: 160 EtOH (*x* = 0.125-1.0; for a given value of *x*, *y* was varied between 0.125-1.25) were synthesized as described above. These above mixtures are denoted as *y* TPA/ *x* TMA/C3. To investigate the effect of hydrothermal treatment, 0.5TPA/ *x* TMA/C3 (*x* = 0, 0.5, 1.0, 1.5) mixtures were placed in screw cap Teflon containers and heated at 90 ^{o}C. Aliquots were taken from the heated mixtures that were quenched at different time intervals. In addition, these above TMA-TPA-silica mixtures were prepared in protonated water and heated at 90 ^{o}C for 2 weeks. The collected solids were removed from their mother liquid by centrifugation at a rate of 13 000 rpm, washed with distilled water until the pH was between 7 and 8, and then dried overnight at 40 ^{o}C.

2.7.4 Samples Added with Various Salts

Silica mixture C3 as mentioned above serves as a background solution. LiCl, NaCl, and CsCl were added to C3 solution with concentrations ranging from 1 to 50 mM. These mixtures were stirred for two hours to dissolve the added salt completely and are denoted as C3/*x* MCl (M=Li, Na, Cs and *x* =1, 2, 5, 10, 20, 50 mM). After that, desired amount of TPABr, and TMABr was dissolved in silica mixtures with added various salts, and the resulting mixtures were denoted as 0.25 TAA/ C3/ *x* MCl (TAA= TPA, TMA).

Another series of samples were also prepared with constant salt concentration where the TAABr content was varied to investigate the effect of electrolyte type on the TAA-silica interactions. Thus different amounts of TAABr were added to C3 mixtures with 5mM salt and denoted as *y* TAA/C3/5mM MCl (y represents the moles of TAA added and increases from 0.25 to 1.25). Mixtures were filtered with 0.45 μm membranes (Corning Co.) prior to analysis. For pH and conductivity studies, the silica solutions with added salt are prepared as described above but with protonated water.

CHAPTER III

TETRAALKYLAMMONIUM-SILICA PRECURSOR PARTICLE INTERACTIONS AT ROOM TEMPERATURE*

3.1 Introduction

^{1}H PFG NMR studies of tetraalkylammonium (TAA) cations in the presence of silica precursor particles at room temperature are complemented as necessary with dynamic light scattering. These results are consistent with the model of the nanoparticles having a core (silica)-shell (TPA) structure, and demonstrate the validity of PFG NMR for measuring TAA-silica nanoparticle interactions. Clear differences can be observed for different organocations and a detailed comparative study between tetramethylammonium (TMA) and tetrapropylammonium (TPA) is presented. The implications of these findings in terms of zeolite nucleation and growth are discussed.

3.2 Experimental

3.2.1 Sample Synthesis

TPA-silica-water mixtures tested in this chapter are prepared as described in subsection 2.7.1. The composition and viscosity of silica mixtures C0-C4 are shown in Table 2-1.

---

*Reproduced with permission from “PFG NMR Investigations of Tetraalkylammonium-Silica Mixtures” by Li, X and Shantz, D. F. *Journal of Physical Chemistry C*, **2010**, *114*, 8449-8458. Copyright 2010 American Chemistry Society.

3.2.2 Experimental

Solution pH, Viscosity, Dynamic Light Scattering (DLS), Relaxation NMR, and PFG NMR measurements were performed as described in subsections 2.2, 2.3, 2.4.

3.3 Results

3.3.1 Formation of Silica Nanoparticles in Silica Basic Solutions

Figure 3-1a shows the hydroxide concentrations of TAAOH-silica mixtures decrease rapidly and then level off with increasing silica concentration in these mixtures. Also initial scattering intensity of DLS measurements on sodium hydroxide silica mixtures (C1-C4) increase as addition of more silica above certain point (see Figure 3-1b). The results shown are in good agreement with previous work by Fedeyko and co-workers.[7, 73] When the silica concentration is below the critical aggregation concentration (cac) the solution pH decreases sharply upon increasing the silica concentration. After the cac point, there is only a very small decrease in the pH with increasing silica concentration. Previous work in the literature has described this behavior in detail. [13, 81] The results in Figure 3-1 are included here as baseline information, and also for comparison to the NMR relaxation and diffusion measurements described below.

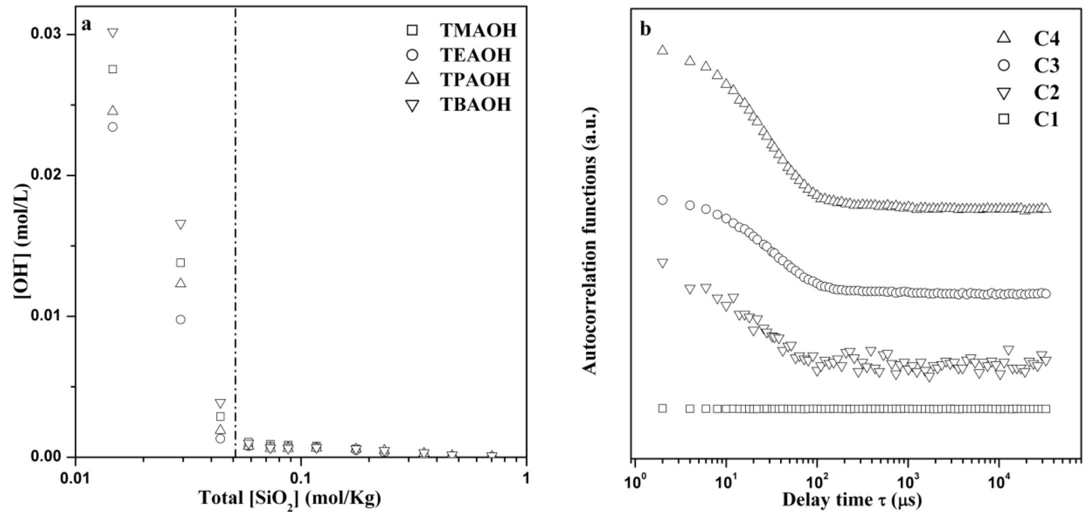

Figure 3-1. (a) Hydroxide concentration as a function of the total silica content in solution. (The dashed line denotes the approximate value of the critical aggregation concentration.) (b) Autocorrelation functions of C1-C4 silica solutions obtained by DLS.

3.3.2 NMR Analysis of TAA-silica Nanoparticle Interactions

^{1}H NMR spectra of 0.5TPA/C0-C4 mixtures are shown in Figure 3-2a. The ethanol resonances due to TEOS hydrolysis are at chemical shift values of 3.63 and 1.17 ppm, neither the line positions nor line widths change appreciably with increasing silica content. The resonances assigned to TPA cations in the C0 solution without silica are at 3.11, 1.68, and 0.92 ppm. The lines gradually lose their fine structure (i.e., *J* coupling) and the line widths increase monotonically upon increasing silica concentration. A simple explanation for the TPA line broadening observed is that there are interactions between the silica in solution and the organocations. The relative intensity ratios of the TPA and ethanol resonances are summarized in Table 3-1, and indicate nearly all the TPA is observable.

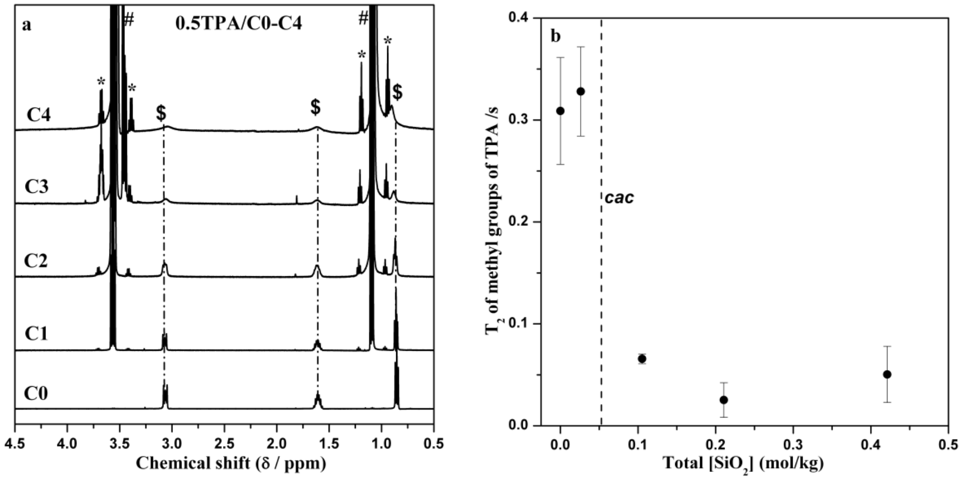

Figure 3-2. (a) ^{1}H NMR spectra and (b) Spin-spin relaxation time (T_2) of TPA in 0.5 TPA/C0-C3 and 1.0 TPA/C4 mixtures. (# Ethanol; $ TPA; * ^{13} C side band; T_2 values of the methyl group of TPA cation are reported here.)

Table 3-1. Relative intensities ratio (R) between TPA and ethanol resonances.*

	0.5 TPA/C3			1.0 TPA/C4	
Resonance assignment	Chemical Shift (ppm)	R_{exp}	R_{Theory}	R_{exp}	R_{Theory}
Ethanol	3.64	0.018	0.019	0.016	0.019
TPA	0.96				

*Average over six integrations for 0.5TPA/C3 and four integrations for 1.0TPA/C4; calculated from integration area of CH_3 group of TPA and CH_2 group of Ethanol.

To investigate this further, transverse relaxation measurements (T_2) were performed on the above TPA-silica mixtures, and shown in Figure 3-2b. The plot shows that TPA has a larger T_2 value when silica concentration above *cac* point than that below *cac* point. . The results in Figure 3-2b are consistent with the idea that the silica-TPA interactions are the origin of line broadening observed in Figure 3-2a. The fact that the value of the relaxation time is essentially constant after the cac seems to imply that increasing the number of nanoparticles does not lead to changes in the TPA-silica interaction. In other words, upon crossing the cac adding more silica leads to more nanoparticles until gelation occurs.

On the basis of the results above the addition of silica to these mixtures leads to a perturbation of the environment of the organociatons as manifested by the movement of certain resonances and the line broadening observed, which is reflected in the decreasing values of T_2. To study this in more detail PFG NMR was used to investigate these mixtures. Figure 3-3a shows the measured organocation diffusion coefficient for TAAOH-silica mixtures as a function of the silica content in the mixture. For all TAA cations it is clearly observed that the observed coefficient decreases (D_{obs}) with increasing silica content. The values of the diffusion coefficients at the lowest silica content are quite similar to those of the value of TAAOH in water. As shown in Figure 3-3b, the observed diffusion coefficient (D_{obs}) of TPAOH in TEOS hydrolyzed solution is smaller than that in the corresponding water/ethanol mixture, and the discrepancy between the two values becomes larger with increasing silica contents. A simple interpretation of the data in Figure 3-3b is that the organocation-silica interactions lead to a reduction in the observed diffusion coefficient. Our attempts to describe this in more detail have focused on a two-state model, wherein the organocation can be described as either “free” in solution or “bound” to the nanoparticle (see Figure 3-4). This simple physical model is chosen for several reasons. First, small molecule binding in macromolecular systems has been successfully described with this approach. The main points of this methodology have been explained in subsection 2.3.2. Second, this appears to be a reasonable physical model for physical adsorption of the organocation on the nanoparticle surface and is consistent with existing models of these systems which report these to be organocation-silica core-shell materials.

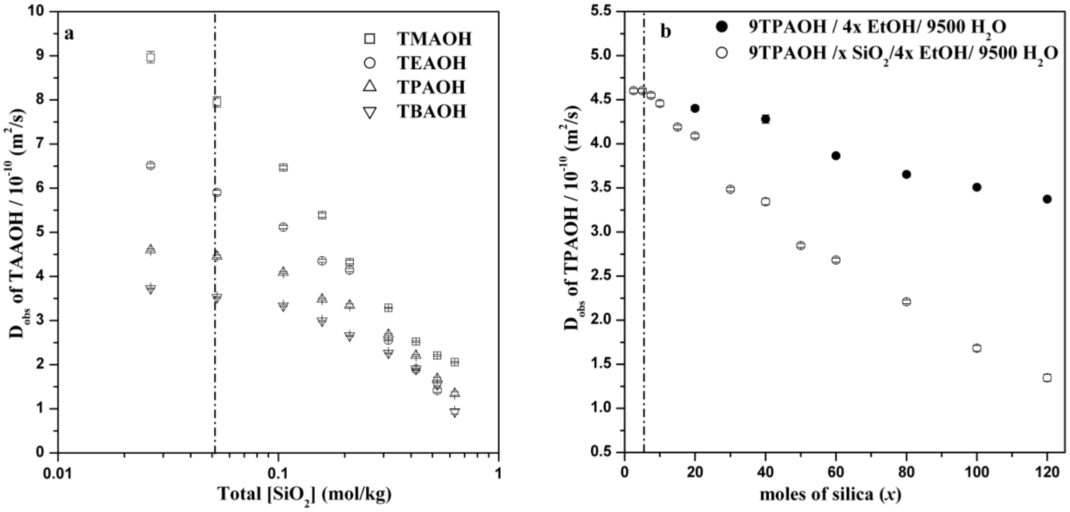

Figure 3-3. (a) Observed diffusion coefficients (D_{obs}) for a series of TAAOH-silica mixtures with constant TAAOH content but varying silica content. (b) D_{obs} of TPAOH in ethanol/water (solid circles) and TEOS/water (open circles) mixtures. (The dashed line denotes the approximate value of the critical aggregation concentration (cac).)

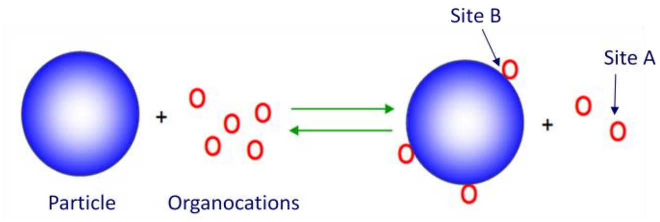

Figure 3-4. Schematic view of TAA cations adsorption on silica nanoparticles in solution.

In the following subsections, a quantitative analysis of TAA-silica nanoparticle interactions was performed through careful comparison experiments. TMA and TPA were chosen as probe molecules and added to C0-C4 silica solutions. This is motivated by TPA cations being widely used as an SDA for the synthesis of silicalite-1 from clear solutions, and TMA is a much more hydrophilic cation, incapable of making zeolites under these conditions (i.e., pure silica mixtures, low-temperature heating). Figure 3-5 shows the diffusion coefficient measured versus the organocations concentration for a variety of TMA-silica and TPA-silica mixtures, i.e. *y* TAA/C0-C4. The lowest concentration mixtures were chosen based on the detection limit of the NMR measurements. The high concentration mixtures were chosen based on the observed diffusion coefficient becoming insensitive to changes in concentration. Three key observations can be made. First, measurements of TMA/C0 and TPA/C0 water solutions show that the self-diffusion coefficient is nearly constant over the range of cation concentrations investigated. This allows us to conclude that TAA aggregation under these conditions is not significant. Second, for C1 solutions only with dissolved silica species (the silica concentration is below the cac point), the observed diffusion coefficients of TMA and TPA are essentially constant with addition of cations and only show a minor variation from the values in the C0 water mixture. Third, for mixtures having silica nanoparticles, i.e., C2-C4 solutions, the observed diffusion coefficients (D_{obs}) within low TAA concentration region was significant lower than the values of C1 solution. One explanation for this reduction in diffusion coefficients could be the changes of the silica solution viscosity with increasing silica content. However, the viscosity measurements of C1-C4 mixtures at 25 °C (see Table 2-1) show that viscosity variation of the silica mixtures is within 40 %. Also given the effect of ethanol due to TEOS hydrolysis on the motion of TAA (see Figure 3-3b), the diffusion coefficient of TPA and TMA were obtained from mixtures with equivalent amounts of ethanol and water as the C2-C4 silica solutions (see Figure 3-6). However, the presence of a large amount of ethanol only leads to a slight decrease in TPA diffusion coefficients. Therefore, in Figure 3-5, the significant reduction of D_{obs} observed within low TAA concentration region (1mM to 10mM) is mainly due to the binding of TAA cations onto the negatively charged silica nanoparticles.

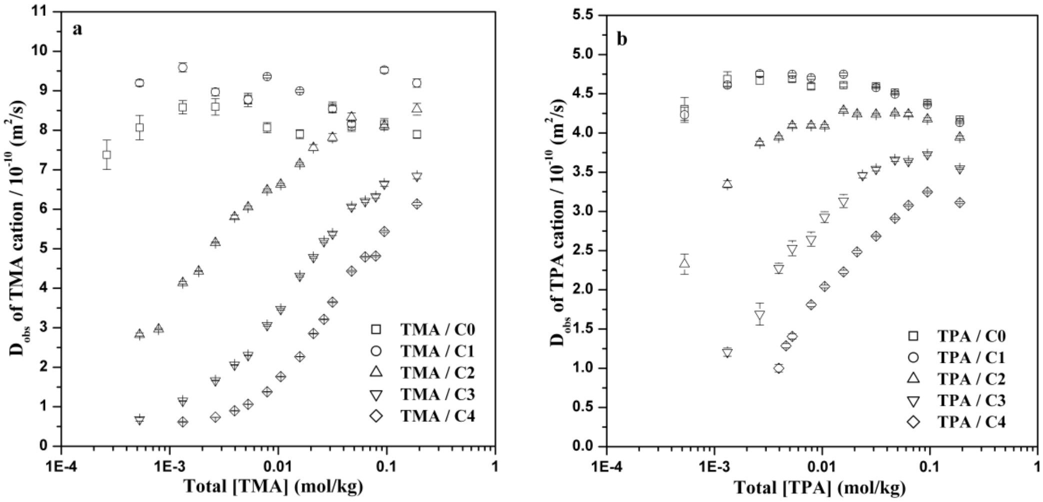

Figure 3-5. Observed diffusion coefficient (D_{obs}) of (a) TMA and (b) TPA as a function of the organocation concentration for several mixtures, which are indicated in the legend.

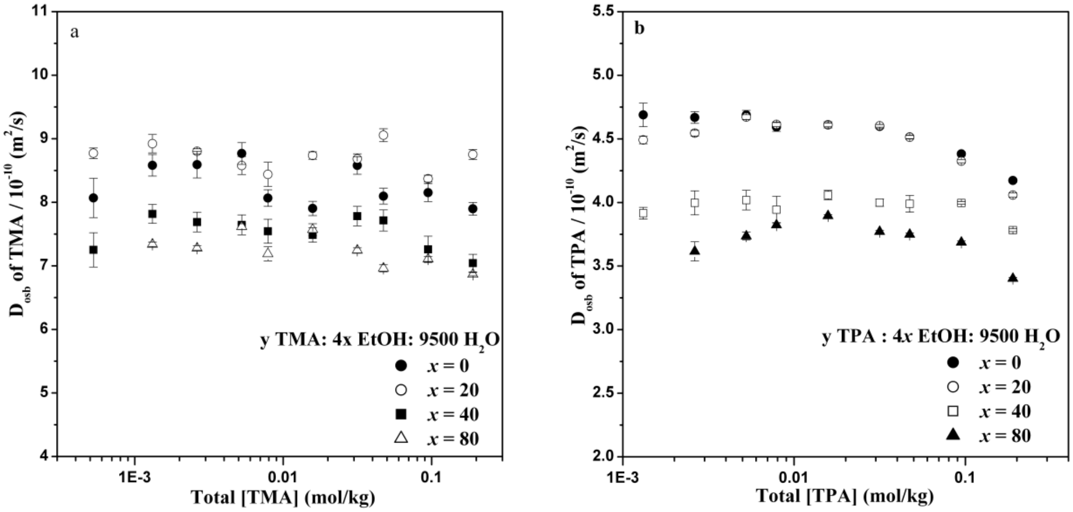

Figure 3-6. Observed diffusion coefficient (D_{obs}) of (a) TMA and (b) TPA in ethanol / water mixtures as a function of total cation concentration. (*y* TAABr/4*x* EtOH/9500 H_2O, *x* =0, 20, 40, 80 and for each *x*, *y* varies from 0.25 to 36.0).

Another noteworthy in Figure 3-5 is that the diffusion coefficients of TAA in C2-C4 mixtures increase rapidly upon addition of more TAA and reach a plateau at high TAA concentration region. This behavior is consistent with the two-state model demonstrated in Figure 3-4. The observed diffusion coefficient obtained by PFG NMR method is an averaged value between the value of free and bound TAA. As shown in Figure 3-5, upon increasing the total TAA concentration, the population of free TAA increases, leading to an increase in the observed diffusion coefficient towards the value of the free diffusion coefficient. The potentially confounding effects of chemical exchange on diffusion experiments must be considered, as mentioned in subsection 2.2.3.[127] To test this, PFG NMR experiments were performed on a series of TMA-silica and TPA-silica mixtures with various organocation concentration, and the diffusion time (Δ) ranging from 0.05 to 1.0 s $\Delta < T_1$. The T_1 values of the TPA-silica and TMA-silica mixtures studied were shown in Table 3-2. Figure 3-7 shows the observed diffusion coefficient (D_{obs}) of TPA and TMA as a function of diffusion time (Δ) in a series of silica mixtures.

Table 3-2. Spin-lattice relaxation time (T_1) of TAA in different silica mixtures.

Samples	C_{TPA} (wt %)	$T_1(s)$	Samples	C_{TMA} (wt %)	$T_1(s)$
1.0TPA/C4	0.14	0.89 ± 0.03	0.25TMA/C4	0.021	1.74 ± 0.05
3.0TPA/C4	0.43	0.82 ± 0.02	1.0TMA/C4	0.083	2.04 ± 0.03
6.0TPA/C4	0.86	0.81 ± 0.02	0.25TMA/C3	0.021	1.82 ± 0.05
0.5TPA/C3	0.07	0.99 ± 0.03	1.0TMA/C3	0.083	2.54 ± 0.02
1.0TPA/C3	0.14	0.85 ± 0.03	0.25TMA/C2	0.021	2.66 ± 0.01
3.0TPA/C3	0.43	0.89 ± 0.02	0.25TMA/C1	0.021	7.69 ± 0.02
6.0TPA/C3	0.86	0.94 ± 0.02	0.25TMA/C0	0.021	8.20 ± 0.11
0.5TPA/C2	0.07	1.03 ± 0.01			
0.5TPA/C1	0.07	1.17 ± 0.02			
0.5TPA/C0	0.07	1.15 ± 0.01			

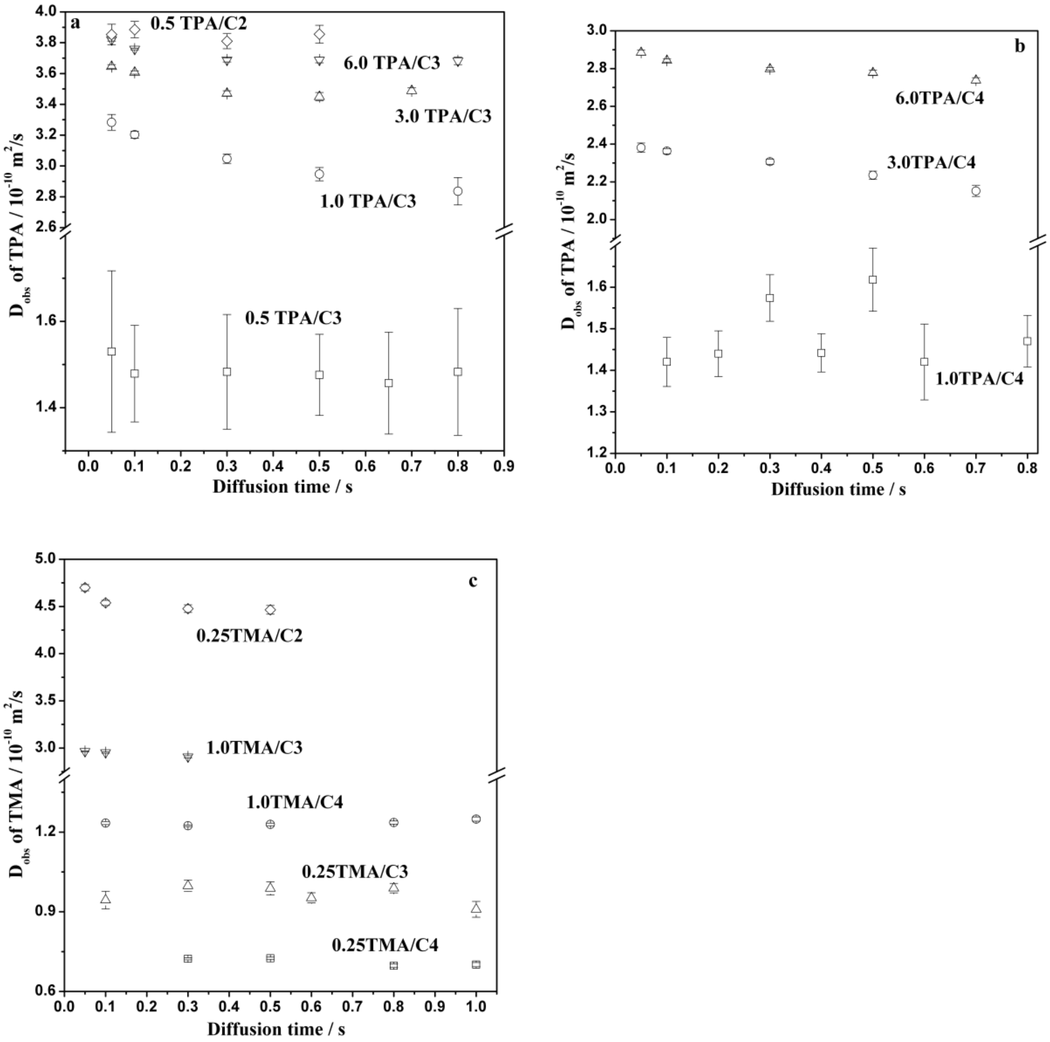

Figure 3-7. Observed diffusion coefficient (D_{obs}) of organocations in as a function of diffusion time (Δ/s) in (a) *x* TPA/C2-C3, *x* TPA/C4 (b) and (c) *x* TMA/C0-C4.

These experiments show that the diffusion coefficients measured within this diffusion time region are essentially independent of diffusion (no attenuation above 5-10%). This and the observation of single exponential intensity decay behavior are both consistent with the cation being in the fast exchange limit. Thurs the observed diffusion coefficient of TAA can be described by:

$$D_{obs} = f_b D_b + f_f D_f \qquad (3\text{-}1)$$

where D_b and D_f denote the diffusion coefficient of free and bound TAA; f_b and f_f denote the fraction of TAA in free and bound state, respectively.

Now with the results above in hand it is possible to determine the fraction of bound organocation (f_b) for the various TAA-silica mixtures. DLS was employed to estimate the diffusion coefficient of the bound state (D_b), as we assume the bound TAA diffuse at the same rate with theses silica nanoparticls. The particle size distribution of C2-C4 silica solutions are shown in Figure 3-8. Thesis mixtures have silica nanoparticles around 5-6 nm in size and a few large particles with size of around 100 nm. However, no large aggregates in silica mixture (C3) were observed from SAXS data (see Figure 3-9). The values of D_f were obtained from a series of TAA-water-ethanol mixtures shown in Figure 3-7.

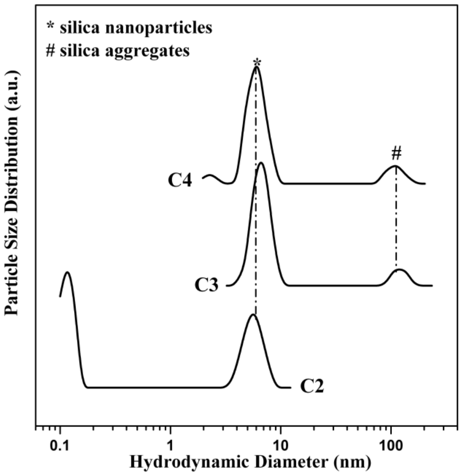

Figure 3-8. Particle size distribution of silica solutions C2-C4 obtained by NNLS fitting of corresponding ACFs shown in Figure 3-1b.

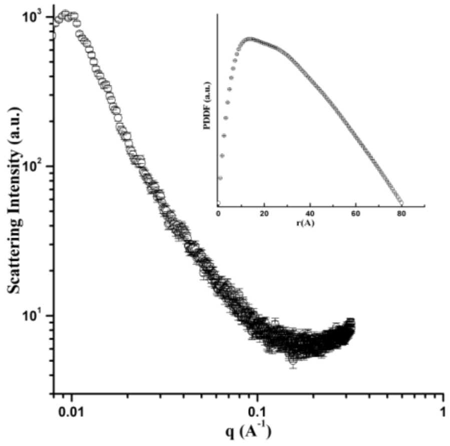

Figure 3-9. SAXS data of silica mixture C3 measured at RT. (Inset) Corresponding pair distance distribution function (PDDF).

Figure 3-10 shows that the fraction of bound TMA and TPA decreases rapidly upon addition of more organocation at first and gradually converges to a constant value in the high organocation concentration region. The concentration of bound TAA cation can then be determined by

$$[TAA]_{bound} = f_b[TAA]_{total} \tag{3-2}$$

Thus, the fraction of TAA bound shown in Figure 3-10 can be replotted as the concentration of bound cation versus total solution concentration, i.e., binding isotherms show in Fig. 3-11. The behavior observed in Figure 3-11 is consistent with classic monolayer (Langmuir) behavior. The strongest binding occurs at low concentrations of TAA and is characterized by a sharp rise in the amount of TAA adsorbed. Following this sharp increase in the amount of TAA bound the value plateaus as the total amount of TAA further increased above 31.5 mM/kg for TMA and 47 mM/ kg for TPA. Also noteworthy is that the maximum amount of TAA bound appears to scale with the silica concentration, implying the amount bound scales with the number of nanoparticles.

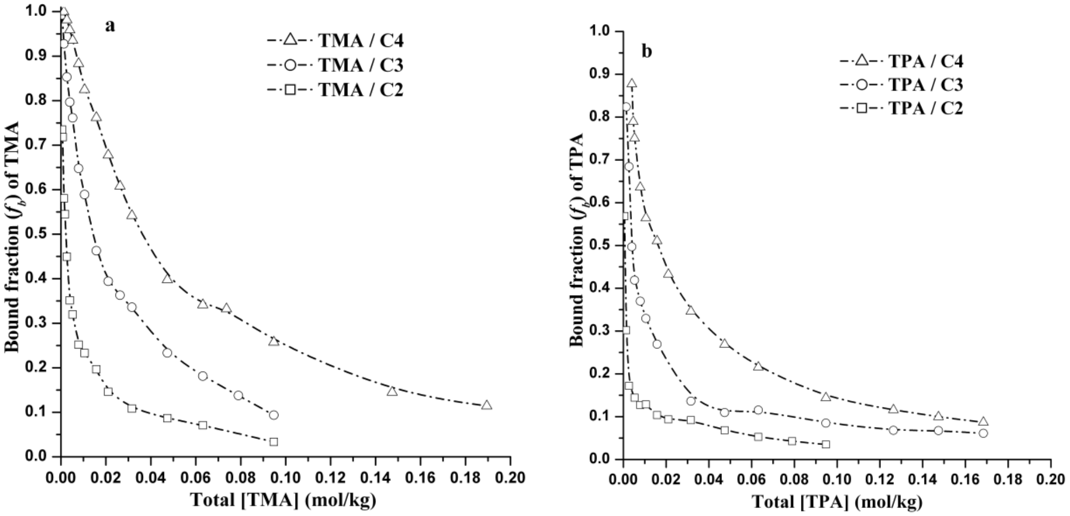

Figure 3-10. Fraction of (a) bound TMA and (b) bound TPA as a function of the organocation concentration in C2, C3 and C4 silica mixtures.

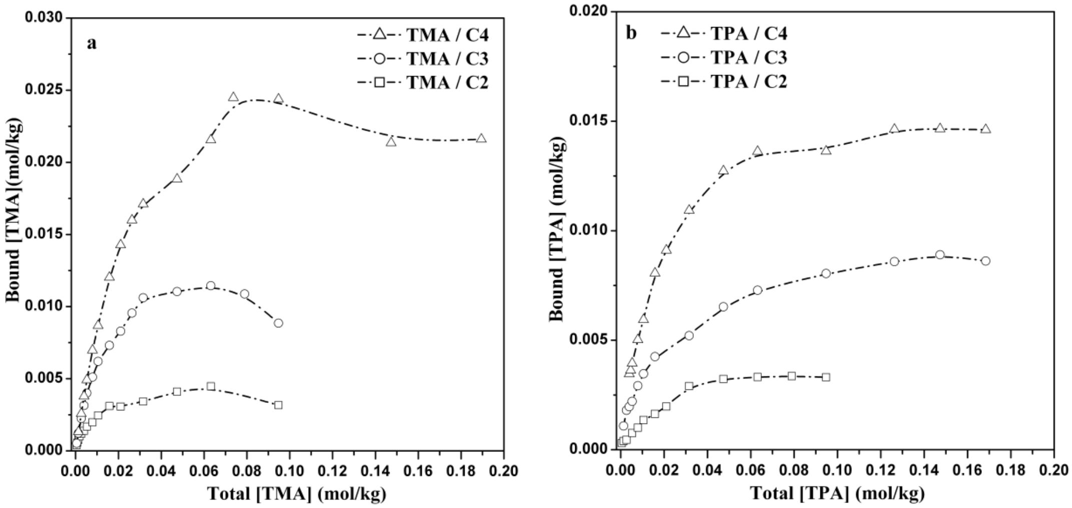

Figure 3-11. Binding isotherms of (a) TMA and (b) TPA in a series of silica mixtures.

If one is willing to assume that the nanoparticle surface is uniform and TAA cations adsorbed onto the surface form a monolayer coverage the Langmuir model can be used to describe the behavior observed in Figure 3-11. This is consistent with previous literature, which indicates that TAA cations form aggregates in water at molarities of approximately 1 mol/L, [101] which is well above the concentrations used in our studies (1.45 mM/L - 0.21 mol/L). For the dilute solutions of this study, the general equation for a Langmuir-type adsorption is similar to that for gas adsorption, expressed as [135, 136]

$$\frac{C_f}{X_b} = \frac{1}{K_{ad} X_b^m} + \frac{C_f}{X_b^m} \tag{3-3}$$

where X_b is the molar ratio of $[\mathrm{TAA}]_{\mathrm{bound}}$ versus $[\mathrm{SiO_2}]_{\mathrm{nanoparticle}}$ (the concentration of silica in the form of nanoparticles) and X_b^m is the ratio at adsorption saturation. K_{ad} is the adsorption equilibrium constant, and C_f is the concentration of free TAA cations in solution at equilibrium. From a plot of $(C_f)/(X_b)$ versus C_f one can obtain X_b^m from the slope and K_{ad} from intercept. The adsorption free energy ΔG_{ad}^o can then be calculated [137]

$$\Delta G_{ad}^o = -RT \ln K_{ad} \tag{3-4}$$

To fully analyze the data and calculate total adsorbed amount at saturation $[TAA]_b^m$ (mol/kg), we need an estimate of $[\mathrm{SiO_2}]_{\mathrm{nanoparticle}}$. On the basis of previous work we assume the dominant silica species are the dissolved monomers and nanoparticles. [13, 99] Using the work of Rimer and co-workers [78], we can describe the composition of silica species as:

$$[SiO_2]_{tot} = [SiO_2]_{monoer} + [SiO_2]_{nanoparticles} \tag{3-5}$$

Also from these previous works we can estimate the monomer concentration from the cac point

$$[SiO_2]_{cac} = 24.147[OH^-] + 0.016 \tag{3-6}$$

Figure 3-12a shows the results of these fits for the various TMA-silica solutions and (b) shows the fits for the TPA-silica solutions. R^2 values of all fits are between 0.969 (TMA/C2) and 0.998 (TPA/C4), showing that the experimental results fit the Langmuir adsorption model well. The deviations from the regression fits consistently appear at the lowest solution concentrations of TMA and TPA.

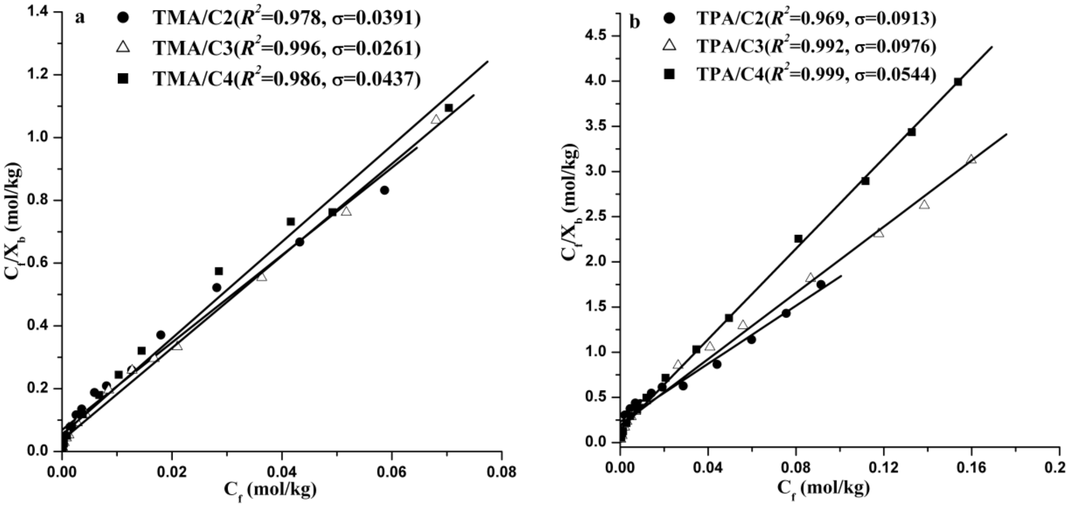

Figure 3-12. Data (circles) and fit (solid line) for (a) TMA-silica mixtures and (b) TPA-silica mixtures as described by the Langmuir isotherm model.

A simple interpretation of this result is that in the dilute solution limit nonhomogeneity of the surface can be detected, or alternatively that the first cations adsorbed bind at the strongest binding sites. Table 3-3 displays the Langmuir constants and derived thermodynamic parameters for TMA and TPA in silicate solutions with different silica content.

Table 3-3. Langmuir constants and derived thermodynamic parameters obtained for adsorbing TAA on silica nanoparticles.

		[b]TMA			[c]TPA		
Solution	[a]$[SiO_2]_{nanoparticle}$ (mol/kg)	$[TMA]_b^m$ (mol/kg)	K_{ad} (kg/mol)	ΔG_{ad}^o (kg/mol)	$[TPA]_b^m$ (mol/kg)	K_{ad} (kg/mol)	ΔG_{ad}^o (kg/mol)
C2	0.063	0.0045	202.27	-13.15	0.0039	69.81	-10.52
C3	0.169	0.0117	295.62	-14.09	0.0092	95.51	-11.29
C4	0.379	0.0243	284.35	-14.00	0.0152	148.64	-12.39

[a] calculated using the value of $[SiO_2]_{cac}$ (0.042mol/kg) obtained from the pH measurement of sodium silicate solutions using equation 3-5 and equation 3-6; [b] For TMA/C2-C4, the average uncertainty in $[TMA]_b^m$ is 3.33 %, and that in K_{ad} and ΔG^o_{ad} is 25.41%; [c] For TPA/C2-C4, the average uncertainty in X_b^m and $[TPA]_b^m$ is 2.96 %, and that in K_{ad} and ΔG^o_{ad} is 17.31%.

As can be seen in Table 3-3, all ΔG_{ad}^o values vary between -10 and -14 kJ/mol, indicating the nonspecific adsorption of TAA cations to silica particles. Comparing the ΔG_{ad}^o and K_{ad} values shown in Table 3-3, TMA displays larger values than TPA with approximately the same silica nanoparticle concentration, suggesting a stronger binding strength between TMA and silica particles. Another notable finding is that more TMA adsorbs on the nanoparticles than TPA for monolayer coverage. Considering the difference in surface charge density of organocations, TMA may have stronger electrostatic interactions with the nanoparticles than TPA. The other notable difference between the two cations is that TPA is more hydrophobic; however, work below, we believe, points to the differences observed being due primarily to electrostatic effects.

3.4 Conclusions

The interactions between TAA cations and silica nanoparticles in a series of clear solutions have been investigated by PFG NMR. The results confirm that binding of TAA cations to silica is a general phenomenon in these mixtures. The binding isotherm of TMA cations and TPA cations in silica mixtures demonstrated a nonlinear behavior and can be well described by the Langmuir adsorption model. From this model, we estimated the monolayer coverage of TAA cations on silica nanoparticles, as well as adsorption equilibrium constants (K_{ad}) and adsorption free energy ($\Delta G^\circ_{\mathrm{ad}}$) for different TAA-silica mixtures. The results indicate that TMA has a stronger adsorption strength and larger adsorption loading on the silica particles than TPA cations. A sharp decrease of T_2 values of organocations in the presence of silica implies that rotational motion of TAA is significantly reduced mainly due to binding. ^{1}H NMR spectral line broadening and the frequency shift of TAA cations with increasing silica content are consistent with the change of T_2. Taken together, the findings in this study have important implications for understanding the organic-inorganic interaction and further, the role of TAA-silica particles in zeolite nucleation. The following Chapter IV investigates how these properties change in TPA-silica mixtures upon hydrothermal treatment.

CHAPTER IV

TETRAALKYLAMMONIUM-SILICA PRECURSOR PARTICLE INTERACTIONS AT ELEVATED TEMPERATURES*

4.1 Introduction

The works shown in Chapter II characterized the organocation-silica nanoparticles interactions in TAA-silica mixtures and determined binding isotherms for these mixtures at room temperature prior to heating. In this chapter, we use PFG NMR to study the evolution of the tetrapropyl ammonium (TPA)-silica nanoparticle complexes as a function of temperature and TPA content. These data are further correlated with DLS to determine the primary nanoparticle evolution over time to provide kinetic information on silicalite-1 nucleation.

4.2 Experimental

4.2.1 Sample Preparation

TPA-silica mixtures (x TPA/C3, where x = 0.5-3.0) studied in this chapter were prepared as described in subsection 2.7.2.

---

*Reproduced with permission from "PFG NMR Investigations of Heated Tetraalkylammonium-Silica Mixtures" by Li, X and Shantz, D. F. *Journal of Physical Chemistry C*, **2010**, *114*, 14561-14570. Copyright 2010 American Chemistry Society.

4.2.2 Analytical

Solution pH and conductivity, powder X-ray diffraction (PXRD), Thermo gravimetric analyses (TGA), Field-emission scanning electron microscopy (FE-SEM), Dynamic Light Scattering (DLS) and NMR measurements were performed as described in subsections 2.2, 2.3, 2.4.

4.3 Results

The solids collected from 0.5 TPA/C3 synthesis mixtures heated for 2 weeks at 90 °C were analyzed by XRD and FE-SEM to verify phase purity. The organic free but otherwise identical silica mixture C3 did not form silicalite-1 under the same conditions. The 0.5 TPA/C3 sample was chosen for investigation as it is dilute in TPA, facilitating PFG NMR, yet mixtures with the same TPA/SiO_2 ratio are known to form silicalite-1.[90] For comparison, nanosized silicalite-1 crystals were synthesized following the protocol of Hedlund et al.[134] and used it as a reference. The XRD data in Figure 4-1 shows that the products obtained from the 0.5 TPA/C3 mixtures are pure MFI-type materials. Figure 4-1 also shows the weight loss curve of the reference sample and the products from 0.5 TPA/C3 in TGA measurements. For the 0.5 TPA/C3 sample, a weight loss of 11.8 wt % is observed over the temperature range of 360 - 650 °C due to the thermal decomposition of the organocations. Despite that the 0.5 TPA/C3 mixture is TPA-deficient (i.e., could not crystallize all silica in the solution), the amount of the organic template corresponds to four TPA molecules per unit cell, indicating that the zeolite forms with the ideal unit-cell composition $[(TPA)_4(SiO_2)_{96}]$. For the reference sample, the total weight loss was approximately 14 wt %, with 1.2 and 11.6 wt % in the temperature ranges 25-280 °C and 300-650 °C. The former weight loss is attributed to physically adsorbed water and organocation at crystal surfaces. The difference in weight loss curves is likely due to the very different size of the crystals, which may lead to more physically adsorbed water on the external surface of the crystals for the reference sample.

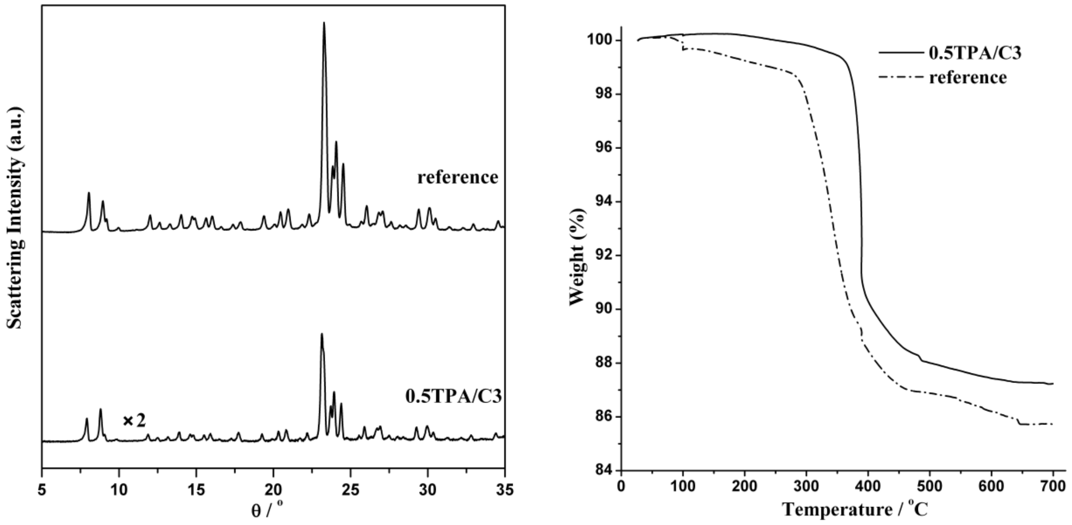

Figure 4-1. (Left) PXRD patterns and (right) TGA traces of the reference sample and solids obtained from 0.5 TPA/C3 synthesis mixtures.

SEM micrographs of the two samples are shown in Figure 4-2. The reference sample exhibits a spherical crystal shape with diameters of 500 nm, whereas the crystals from the 0.5 TPA/C3 solution are large (~10 μm) with high length/width ratios. It appears that fewer nuclei form in the TPA-limited synthesis solution, and hence relatively large crystals are produced. The results above indicate that silicalite-1 crystals can be synthesized from 0.5 TPA/C3 solution mixtures and the zeolite yield is limited by TPA availability (silicalite-1 yield is between 1-2 % based on silica). Also, the formation of elongated flat crystals from the dilute solution with high H_2O/SiO_2 ratio is in a good agreement with previous studies. [66, 138] Detailed measurements for the dilute synthesis mixture were performed to gain insight into how the organocation-silicate interactions evolve during initial heating.

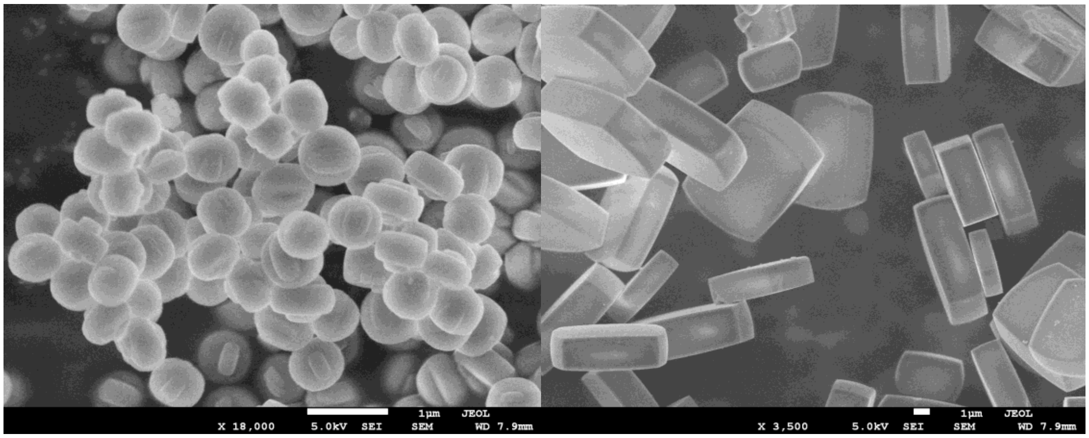

Figure 4-2. FE-SEM images of (left) a reference sample of silicalite-1 and (right) an as-synthesized 0.5 TPA/C3 sample. (Scale bar is 1μm in both images.)

The pH and conductivity (σ) were measured for 0.5 TPA/C3 heated at 90 °C over a 24-h period and is shown in Figure 4-3. It is observed that both of pH and conductivity increase within the first eight hour of heating and level off as time progresses. This change of solution properties indicate that a fraction of silica precursor particles might dissolve and/or aggregate during heating. Figure 4-4 shows the particle size distribution of the 0.5 TPA/C3 sample subjected to hydrothermal treatment (70-100 °C) for 48 h.

Particles with a radius of approximately 6 nm were observed in all samples prior to heating.

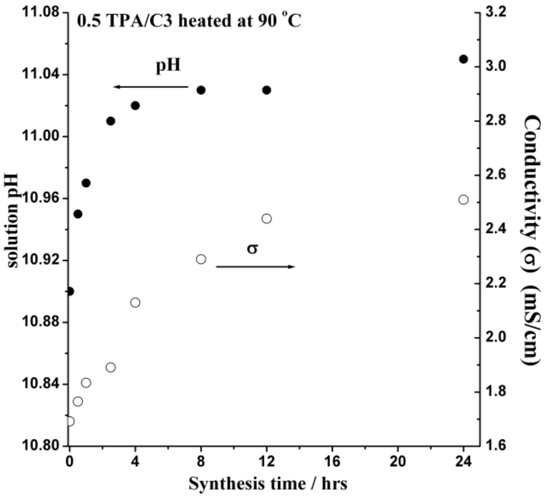

Figure 4-3. pH and conductivity (σ) of 0.5 TPA/C3 sample heated at 90 °C over 24 h period.

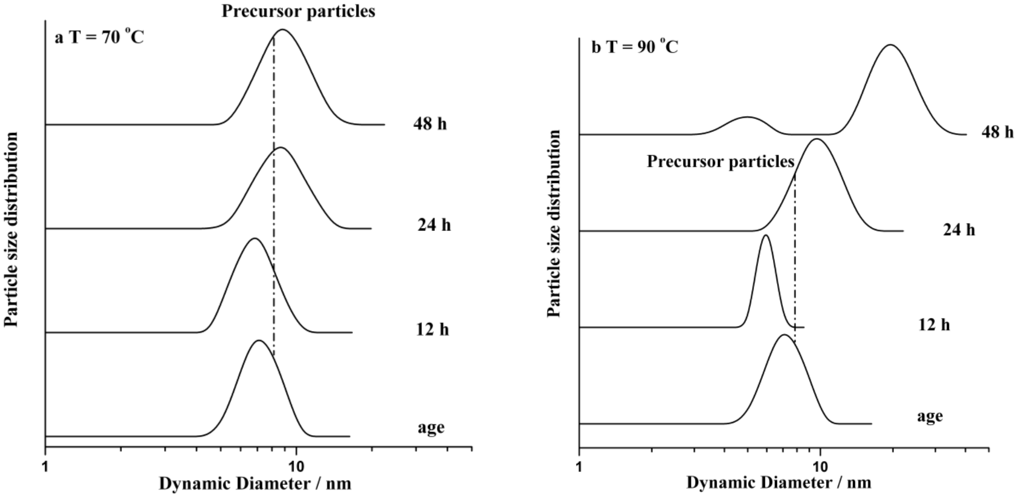

Figure 4-4. Particle size distribution obtained from DLS data of 0.5 TPA/C3 mixture prepared with deuterated water and heated at various temperatures for 48h (a-c): 70 °C, 90 °C and 100 °C.

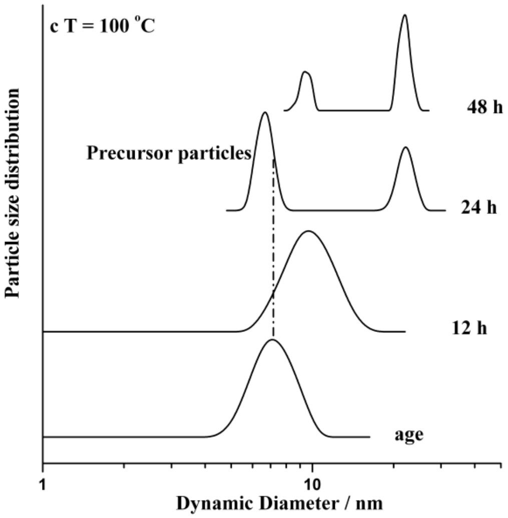

Figure 4-4. Continued.

As shown in Figure 4-4a, no significant changes were observed in the particle size upon heating at 70 °C after 48 h. Upon heating at 90 °C only a slight increase in the particle size is observed during the first 24 h (see Figure 4-4b). A clear difference is observed upon heating for 48 h, as most of the particles increase in size to approximately 20 nm, and a much smaller population of 5 nm particles is observed. For samples heated at 100 °C (Figure 4-4c), a second population of particles with a radius of approximately 20 nm is observed after 24 h of heating. The number density of these particles increases upon heating for an additional 24 h. In general, nanoparticles approximately 5-7 nm in diameter have been observed in the heated sample, and their number remains stable during the first 24 h of heating at 70-100 °C. These observations are consistent with previous studies.[78, 83, 85]

4.3.1 ^{1}H NMR

The previous chapter reported silica-organocation interactions in these mixtures prior to heating. Given the intense interest in understanding the evolution of these particles during heating and the steps involved in nucleation, here we focus on quantifying the silica-organocation interactions after these mixtures have been heated. Of particular relevance to the current work is a previously published study by Rimer and co-workers.[78] Their work suggested that the particles evolve via an Ostwald ripening process and that a fraction of them grow into larger and more stable particles while many dissolve during heating. Also noteworthy is that the nanoparticles are stabilized by a layer of organic cations and may evolve into viable nuclei with incorporated organic template upon hydrothermal treatment.

^{1}H NMR measurements were performed on 0.5 TPA/C3 mixtures to monitor the organocation during heating. These results are expected to provide information about the TPA-nanoparticle interactions and how they change upon heating. Figure 4-5 shows the ^{1}H NMR spectra of 0.5 TPA/C3 mixtures heated at 70, 90 and 100 °C over 48 h. The ethanol resonances due to TEOS hydrolysis are at chemical shift values of 3.63 (not shown) and 1.17 ppm, and the line positions do not change upon heating. The resonances assigned to TPA cations are at 3.13, 1.68, and 0.95 ppm. In previous work we showed that the TPA resonances broaden upon the introduction of silica due to binding of the cations onto the nanoparticles. No appreciable change of the chemical shift values is observed for the TPA resonances. However, the line widths and intensity vary with increasing temperature and heating time. At the lowest temperature (70 °C), neither the line widths nor the line intensities change appreciably with synthesis time (see Figure 4-

5a). However, the line intensity of the methyl group of the TPA cation at 90 °C gradually increases with heating time (see Figure 4-5b). Further increasing the temperature to 100 °C leads to a pronounced increase in the intensity along with a decrease in the line widths during heating. (see Figure 4-5c)

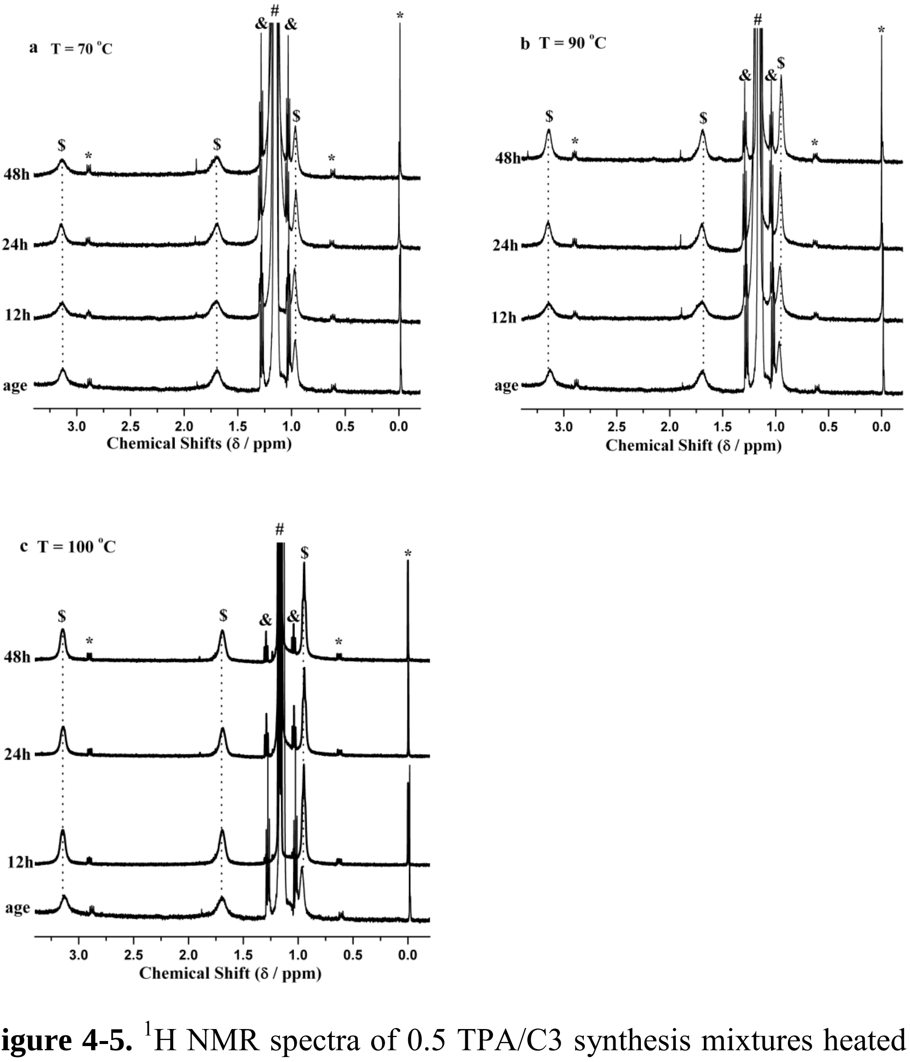

Figure 4-5. ^{1}H NMR spectra of 0.5 TPA/C3 synthesis mixtures heated at (a) 70 °C, (b) 90 °C and (c) 100 °C. (For clarity, the ethylene group (3.63 ppm) of ethanol is not shown, and the *y*-axis is on the same scale.)

To give a more quantitative analysis and avoid the effect of ethanol loss during heating, the relative intensity ratios (*R*) of the methyl group of TPA (0.95 ppm) versus the methyl group of DSS (0 ppm) (internal standard) in the sample upon heating are summarized in Figure 4-6. An increase in the intensity ratio for samples heated at 90 and 100 °C with time was observed, and the ratio increases with increasing heating temperature. This is not observed for the sample heated at 70 °C, which possibly indicates more TPA remains bound to the nanoparticles. It is not clear why the ratio increases above the theoretical maximum of 6.7, which is calculated based on the molar ratio of TPA/DSS (5) and total number of protons in their methyl groups. One possibility is that the DSS partially decomposes upon heating; the trend with temperature in Figure 4-6 would be consistent with this (i.e., lower heating temperatures lead to less decomposition and a lower ratio). However, the key conclusion from Figure 4-6 is that before heating the observed intensity ratio is within 10 % of the expected ratio. This implies that there is not a sizable population of unobservable TPA cations. A simple explanation of the changes in the line widths and intensity in Figure 4-6 is that the mobility of the TPA increases upon heating. PFG NMR is used to quantify this.

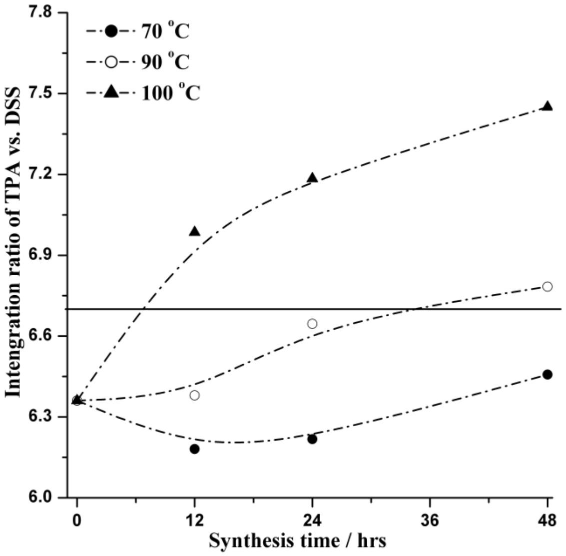

Figure 4-6. Relative intensity ratio (*R*) of TPA cations versus DSS in 0.5 TPA/ C3/ 0.1 DSS samples. (*R* is the ratio of integration area of the CH_3 group of TPA versus the CH3 group of DSS. The solid line represents the theoretical *R* value of 6.7. The estimated variability in the values is between 10 and 15% due to the low concentration of TPA and DSS.)

Figure 4-7 shows the observed self-diffusion coefficient (D_{obs}) of TPA in the 0.5 TPA/C3 mixtures as a function of heating time at different heating temperatures. As can be seen the observed self-diffusion coefficient rapidly increases upon heating, and in all cases effectively plateaus to a constant value after 16-24 h of heating. Of note is that the value at which the diffusion coefficient plateaus is temperature dependent. These systems are more complex than our previous work investigating the mixtures at room temperature, as during heating one can anticipate that the particle structures are dynamic in nature and that particle dissolution, growth, and particle restructuring are all occurring simultaneously. We have previously shown that these systems are in the fast exchange limit, and thus the data in Figure 4-7 can be analyzed with a two-state model, i.e., free and bound state. Thus, the measured diffusion coefficient (D_{obs}) is an averaged value of the two sites and described as equation 3-1.

$$D_{obs} = f_b D_b + f_f D_f \tag{3-1}$$

where D_{f} and D_{b} are the diffusion coefficient of free and bound cations and f_{f}, f_{b} are the free and bound fraction, respectively. The value of D_{f} was estimated from the diffusion coefficient of TPA in water/ethanol mixtures with compositions equivalent to C3 mixture but no silica ($(3.997 \pm 0.094) \times 10^{-10}$ m^2/s). The value of D_{b} has been estimated from DLS measurements (0.626×10^{-10} m^2/s) [139] and is considered as an average value for the nanoparticles with size in the 5-7 nm range. Therefore, the bound fraction (f_{b}) of TPA at various heating times can be calculated from the above equation, and the results are shown in Figure 4-8. This figure shows two key points: first, the fraction of bound cations trends downward over the first 16-24 h of heating and then plateaus. Second, the "final" fraction of bound cations is dependent on the heating temperature. Thus, upon heating a smaller fraction of organocations are associated with the nanoparticles.

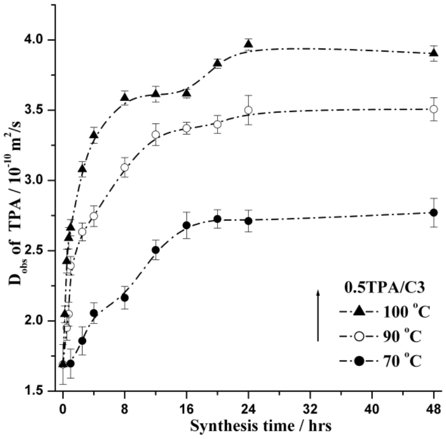

Figure 4-7. Observed diffusion coefficient (D_{obs}) of TPA as a function of time for 0.5 TPA/C3 samples heated at various temperatures.

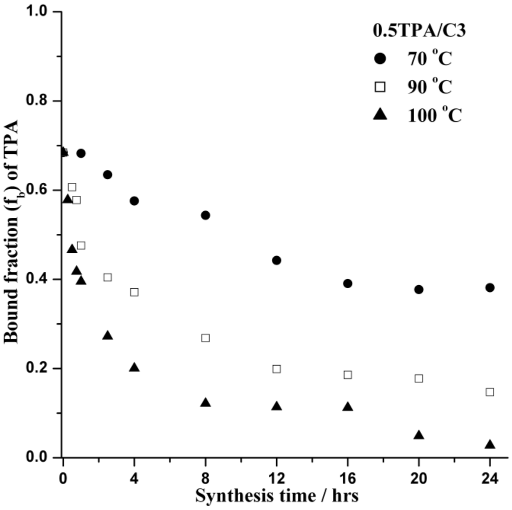

Figure 4-8. Bound fraction (f_b) of TPA cations as a function of time for 0.5 TPA/C3 mixtures heated at various temperatures.

There are several possible explanations for the above results. The first possibility is that the nanoparticles dissolve upon heating. This physically seems reasonable as the solubility of small silicate oligomers is temperature dependent. If there are fewer nanoparticles, all things being equal there will be fewer bound TPA cations. Another possible factor is that previous work has shown via neutron scattering that TPA becomes occluded in the nanoparticles upon heating. We have no evidence to believe that we can observe occluded TPA cations, as one would expect TPA encapsulated in silica to have a dramatic reduced T_2 due to restricted mobility and likely not contribute to the observed NMR signal. Consistent with this, experimentally we observe that the T_2 value of TPA in the C3 mixture heated at 100 ^{o} C is essentially constant (See Table 4-1). If there is a population of TPA cations that are not observable by NMR, we would expect to see the opposite trend than that observed in Figure 4-6. However, another possibility is that the likely small amount of TPA occluded in the silica nanoparticles would lead to small changes in intensity that are very hard to quantify within these experiments. The third possibility is that upon heating the number of TPA cations that can absorb per particle dramatically decreases. This last point may be possible but is very hard to ascertain analytically. Nevertheless, at the most cautious level, our results clearly show that upon heating there is a significant increase in the self-diffusion of the TPA cations in the mixture. This is consistent with the existing picture that some of the nanoparticles dissolve upon heating, and that in turn would imply more TPA is available to be released into solution. That the diffusion coefficients plateau at different temperatures after 16-24 h of heating would seem to imply that this dissolution process is by and large complete by that time. Also that the diffusion coefficient increases with heating temperature seems logical as one would anticipate that the largest number of nanoparticles would be dissolved at the highest heating temperature.

Table 4-1. Spin-spin relaxation time (T_2) of the TPA methyl group in 0.5 TPA/C3 samples heated at 100 °C.

Synthesis Time (h)	T_2 (s)	error
0	0.025	0.017
12	0.022	0.002
24	0.027	0.007
48	0.030	0.001

Presumably for nanoparticle dissolution to take place the organocations associated with the particles need to first desorb. This is consistent with our NMR data that show a pronounced increase in TPA diffusivity, even at the shortest heating times. To quantify this, a variety of models was used to assess this process. The bound faction of TPA decreases gradually with heating time and finally converges to a constant value after 24 h. Also the bound fraction decreases more rapidly with increasing heating temperature, indicating an obvious thermal effect on the desorption kinetics. With the results above it is now possible to obtain the amount of desorbed TPA as function of heating time from the following equation

$$[TPA]_{des}^{i} = [TPA]_{total}(f_b^o - f_b^i) \tag{4-2}$$

where f_b^i is the bound fraction shown in Figure 3-8 and $[TPA]_{des}^{i}$ is the amount of desorbed cations (mM/kg) calculated for each time (t). Three kinetic models were tested to find out the appropriate desorption rate expression: the pseudo-first-order (equation 4-

3a) [140, 141], pseudo-second-order (equation 4-3b) [142-144], and intraparticle diffusion model (equation 4-3c) [145]

$$\frac{1}{q_t} = (\frac{k_d}{q_e})(\frac{1}{t}) + \frac{1}{q_e} \tag{4-3a}$$

$$\frac{t}{q_t} = \frac{1}{k_d q_e^2} + \frac{1}{q_e} t \tag{4-3b}$$

$$q_t = k_d t^{0.5} + C \tag{4-3c}$$

where $q_t = [TPA]_{des}^{i}$, k_d is the desorption rate constant in (mM/ kg)$^{-1}$ h^{-1}, and q_e is the equilibrium desorption capacity with nits of mM/kg. The parameters obtained from fitting the models are shown in Table 4-2. R^2 values of the pseudo-second-order kinetic model fit are 0.94 for data at 70 °C and 0.99 for data at 90 and 100 °C, indicating that the model fits the data reasonably well. Additionally, R^2 values for the intraparticle diffusion model were between 0.83 and 0.92, suggesting that release of TPA cations mostly occurred on the nanoparticle surface and intraparticle hindrance for desorption was nearly absent. Figure 4-9 shows the linear plot of t/q_t versus time t for the second-order model at various temperatures, from which the values of k_d and q_e at each temperature were calculated and are shown in Figure 4-10.

Table 4-2. Fitting results for TPA desorption at various temperatures using different kinetic models.

	1^{st} order model			2^{nd} order model			Intraparticle diffusion model		
T(°C)	R^2	σ	P-value	R^2	σ	P-value	R^2	σ	P-value
70	0.948	0.5453	<0.0001	0.938	4.3497	<0.0001	0.835	0.1402	5.65×10^{-4}
90	0.952	0.3172	<0.0001	0.987	0.6845	<0.0001	0.924	0.1315	<0.0001
100	0.986	0.1107	<0.0001	0.991	0.4723	<0.0001	0.892	0.1726	<0.0001

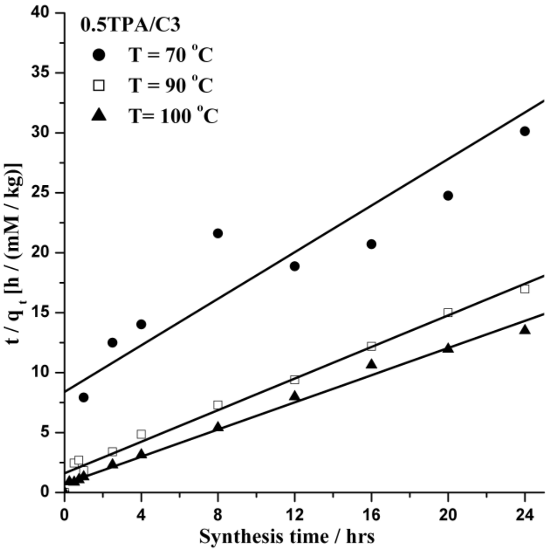

Figure 4-9. Pseudo-second-order kinetic plots of TPA desorption for 0.5 TPA/C3 sample heated at 70, 90 and 100 °C. (The solid lines represent the fit to the model).

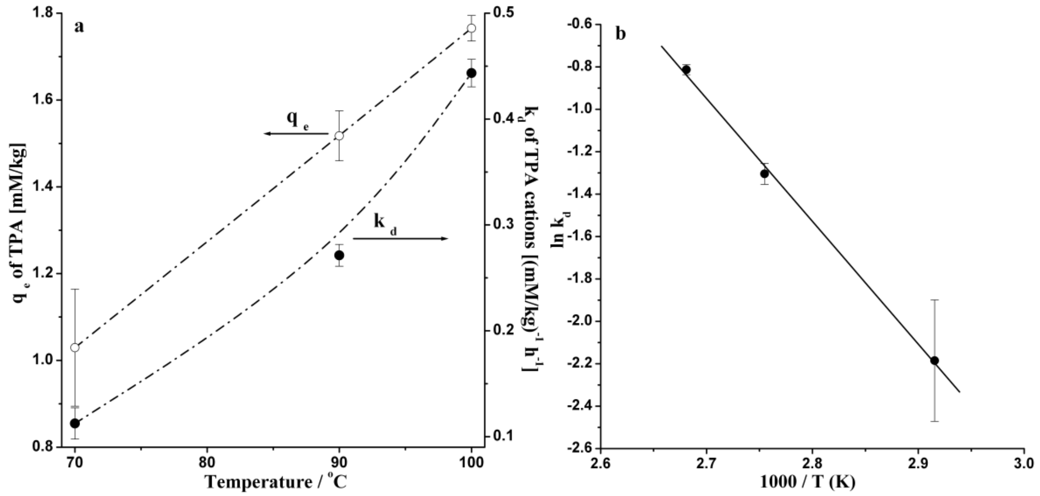

Figure 4-10. (a) Kinetic parameters for TPA desorption for 0.5 TPA/C3 mixtures subjected to various temperature. (b) Arrhenius plot of the TPA desorption kinetics of 0.5 TPA/C3 sample at 70 °C-100 °C. (R^2= 0.997) The solid lines represent the fit to the linear regressions.

Increasing the temperature leads to an increase in the rate constant (k_d), indicating that the desorption of TPA is kinetically controlled. Figure 4-10 also shows that the desorption amount (q_e) of TPA at equilibrium rises linearly with temperature. This conclusion seems consistent with the number density of nanoparticles decreasing with increasing temperature, and thus less surface area for TPA adsorption, leading to a shift in the system toward more desorbed TPA. Given that the structure and composition of the nanoparticles are dynamic duration heating, the concept of an "equilibrium" between adsorbed and desorbed cations is not quantitatively correct. Thus we believe that the values of q_e should be treated with some caution, but the values (Figure 4-10a) appear reasonable in that the value of q_e increases from the model as the fraction of bound cations decreases as determined by PFG NMR. Figure 10b shows the Arrhenius plot of rate constant (k_d). The activation energy (E_A) of TPA desorption for the initial heating stage is obtained from this plot and found to be 48.2 ± 2.1 kJ/mol. This value is comparable with previous results obtained from scattering measurements but is on the low end of E_A values for clear solution syntheses that range between 40 and 90 kJ/mol. [46, 57, 62, 90, 146] This suggests that TPA desorption is likely not the rate-limiting step at the initial heating stage for zeolite nucleation. Given that the NMR work above is analyzing the organocation and not the inorganic species (i.e., silica particle size versus time), this might explain the determination of a value on the low end of the reported values. Nevertheless, it provides kinetics information on the decrease in number of TPA-stabilized particles via ripening mechanism. [7, 11, 65, 76, 78, 84, 147]

4.3.2 Effect of TPA Content on TPA Desorption Kinetics

Many studies on silicalite-1 crystallization kinetics found a trend toward an increasing number of crystals as TPA content increases, indicating the influence of TPA upon nucleation rates. Also Figure 4-11 shows the effect of TPA content on silicatlie-1 crystal morphology. To investigate this effect further, PFG NMR measurements were performed on heated *x* TPA/C3 mixtures where *x* was varied from 0.25 to 3.0 to test the effect of TPA content on the time-resolved diffusion coefficient values. The moles of TPA (*x*) was chosen based on an ideal unit-cell composition of silicalite-1 ($[TPA]_4[SiO_2]_{96}$), and when $x > 1.67$, TPA present is in excess relative to the silica. Figure 4-12 shows the ^{1}H NMR spectra of TPA-silica mixtures with various TPA concentrations prior to heating. It is observed that the line intensity of TPA increases dramatically upon increasing the TPA content as expected. To address this in more detail, Figure 4-13 shows the observed diffusion coefficient (D_{obs}) of TPA as function of heating time for the same mixtures shown in Figure 4-12. The initial D_{obs} values systematically increase with increasing TPA content, indicating a decrease in the bound fraction of TPA cations based on the two-site model as described by equation 3-1. Also, D_{obs} values for all samples display a similar increasing trend with heating time whereas the increase becomes less apparent at higher TPA concentrations, which indicates a potential limit of PFG NMR method on probing the mobility change of TPA at high TPA concentration. It is likely due to the fact that the NMR signal is more sensitive to the free organocations, and there are more free TPA cations in the silica mixtures at higher TPA concentration.

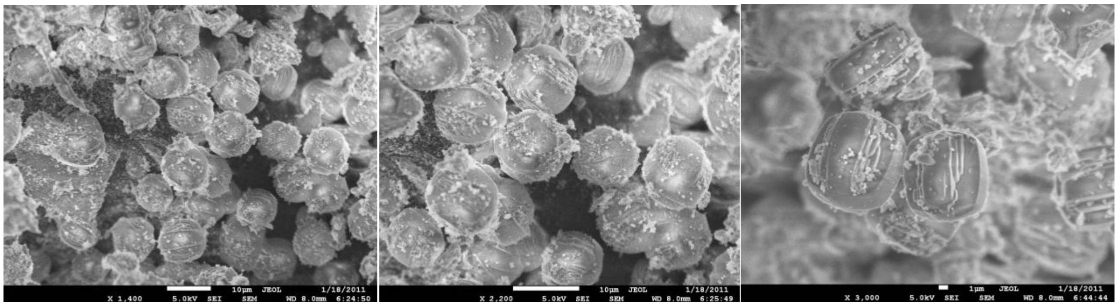

Figure 4-11. FE-SEM image of solids obtained from (left) 9.0 TPA/C3, (middle) 3.0 TPA/C3 and (right) 1.5 TPA/C3 samples heated at 90 ^{o}C.

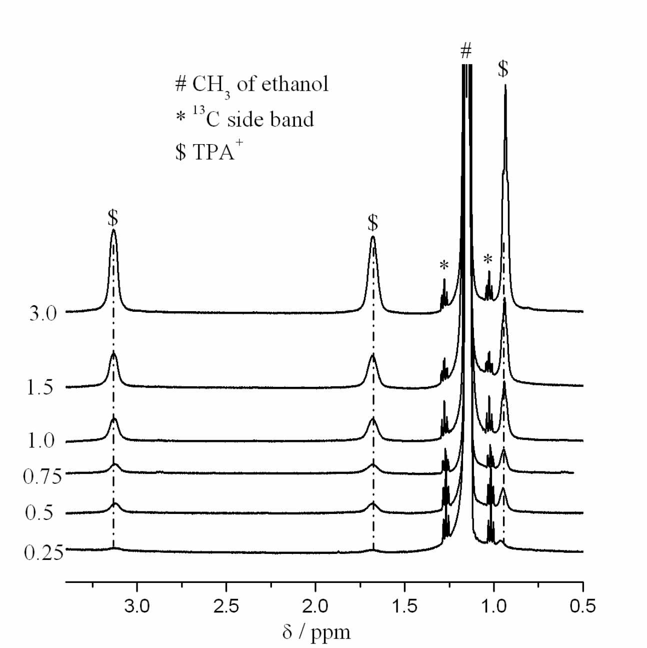

Figure 4-12. ^{1}H NMR spectra of ageing sample with increasing TPA content in *x* TPA/C3 samples (from bottom to top *x* increase from 0.25 to 3.0).

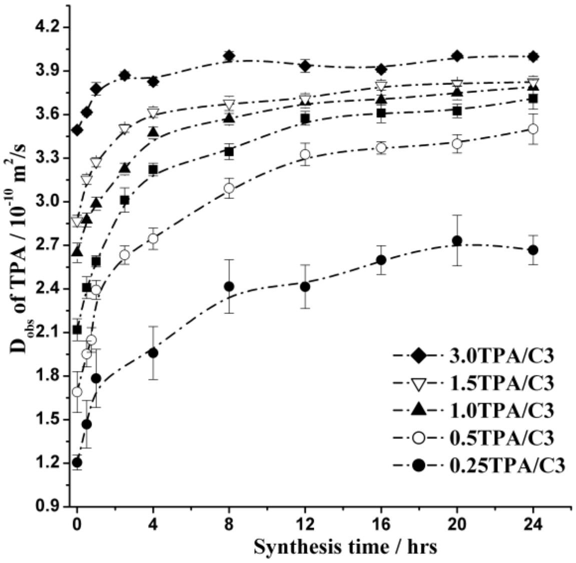

Figure 4-13. Observed diffusion coefficient (D_{obs}) as function of time at 90 °C for samples with increasing TPA content.

In order to analyze this effect of TPA content on the cation desorption kinetics, the amount of desorbed TPA as a function of heating time for the x TPA/C3 samples (x = 0.5-3.0) was calculated via equation 4-2 and fitted with the pseudo-second-order desorption model (equation 4-3b). All plots of t/q_t versus t for these TPA-silica mixtures yield straight lines (see Figure 4-14), and the fit results are shown in Table 4-3. The desorption rate constants (k_d) of TPA were calculated from these above linear plots and shown plotted against moles of TPA (x) in Figure 4-15.

Table 4-3. Fitting results for TPA desorption at different content in TPA-silica mixtures using pseudo-second-order kinetic model.

mole of TPA (x)	R^2	σ	P-value
0.75	0.991	0.42823	<0.0001
1.0	0.992	0.43506	<0.0001
1.5	0.995	0.20297	<0.0001
3.0	0.982	0.53589	<0.0001

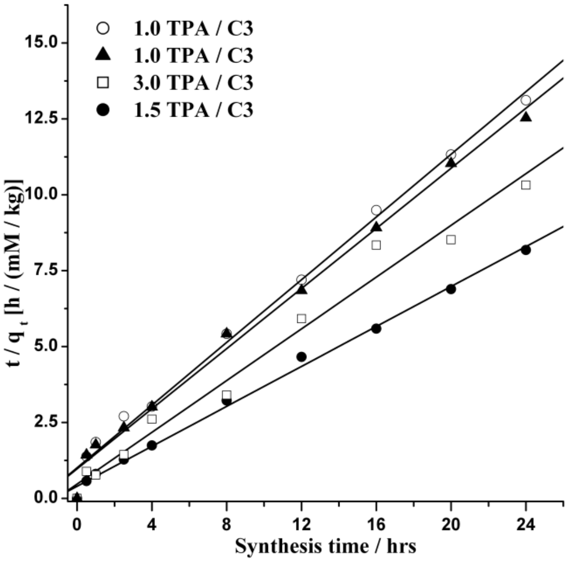

Figure 4-14. Pseudo-second-order kinetic plots of TPA desorption for *x* TPA/C3 samples heated at 90 °C. (The solid lines represent the fit to the model; *x*= 0.75, 1.0, 1.5, 3.0).

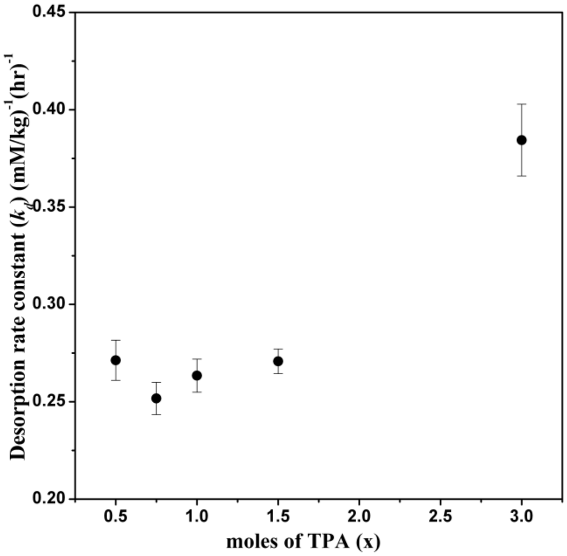

Figure 4-15. Desorption rate constant (k_d) of TPA as s function of TPA content in *x* TPA/C3 (*x*= 0.5, 0.75, 1.0, 1.5, 3.0) samples heated at 90 °C. k_d was obtained from the pseudo second order kinetic model.

k_d values of TPA-deficient mixtures ($x < 1.67$) are constant in spite of an increase in the TPA content, whereas the 3.0 TPA/ C3 mixture shows a much larger value. This could indicate that at these higher TPA concentrations the large excess of TPA results in the process no longer being dependent on TPA desorption. At a most conservative level, it is clear that at the highest level of TPA in these mixtures the desorption process appears very different than at the other TPA concentrations. This trend is also qualitatively consistent with the visual observations of these mixtures that indicate the turbidity onset is very rapid for the 3.0 TPA/C3 mixtures as compared to the others.

4.4 Conclusions

The PFG NMR results above show that the measured self-diffusion coefficient of TPA in these TPA-silica mixtures is sensitive to heating. The results imply that upon heating the nature of the silica-TPA association changes dramatically and occurs before significant particle growth/evolution is observed by scattering methods. While the self-diffusion coefficient increase could in part be attributed to the decrease in the number density of precursor particles, another likely contribution is that surface restructuring of the nanoparticles leads to a decrease in the amount of TPA bound. Unfortunately we do not have any evidence for the latter point, although it seems at least qualitatively consistent with previous work and consistent with the idea that upon heating the silica solubility and dissolution kinetics will likely lead to restructuring (and complete dissolution in some cases) of the nanoparticles. The current work shows PFG NMR to be a uniquely sensitive tool to changes in the chemical environment and binding of the TPA cations and their association with the nanoparticles. The next chapter investigates silica mixtures with mixed organocations, studying competitive binding of these organocations on silica nanoparticles.

CHAPTER V

COMPETITIVE ADSORPTION OF TETRAALKYLAMMONIUM CATIONS PRIOR TO AND DURING ZEOLITE FORMATION*

5.1 Introduction

Chapter III quantified organocation-silica nanoparticle interactions in tetraalkylammonium cation (TAA)-silica mixtures and obtained binding isotherms for these mixtures atroom temperature. That work showed that organocation exchange on and off the silica nanoparticles was rapid on the NMR time scale, and thus the obtained self-diffusion coefficient could be analyzed in the context of a simple two-state exchange problem. Chapter IV showed PFG NMR measurements on TPA-silica mixtures and studies of evolution of TPA-silica particles upon heating. The energy of TPA desorption from the silica nanoparticles was also determined. In this chapter, we expand the scope of that work by determining how the presence of tetramethylammonium (TMA) as a foreign ion affects TPA-silica interactions and nanoparticle evolution upon heating. The mixed organocation study was motivated by work from our lab [46] showing that a small perturbation of the TPA structure affects silicalite-1 nucleation significantly. Also, many researchers have speculated about how

---

*Reproduced with permission from "PFG NMR Investigations of TPA-TMA-Silica Mixtures" by Li, X and Shantz, D. F. *Langmuir*, **2011**, *27*, 3849-3858. Copyright 2011 American Chemistry Society.

the organocation properties (i.e., charge density/ hydrophobicity/geometry) impact zeolite phase selectivity.[4, 47, 148] However, this is still not well understood. Thus, studies of how precursor particles evolve in the presence of multiple organocations should provide insights on synthesizing zeolites in the presence of multiple organic molecules.

5.2 Experimental

5.2.1 Sample Preparation

TMA-TPA-silica mixtures were prepared as described in subsection 2.7.3.

5.2.2 Analytical

Powder X-ray diffraction (PXRD), Thermogravimetric analyses (TGAs), Field emission scanning electron microscopy (FE-SEM), Dynamic Light Scattering (DLS), and NMR measurements were performed as described in subsection 2.2, 2.3, 2.5.

5.3 Results

Mixed organocation-silica mixtures 0.5TPA/ *x* TMA/ C3 (*x* = 0.5, 1.0, 1.5) were heated at 90 °C to investigate the effect of TMA concentration on the growth of silicalite-1. Those mixtures were chosen as the dilute TAA content facilitates NMR measurements and the 0.5TPA/C3 mixture, i.e., in the absence of TMA, has been shown previously by our lab to form silicalite-1. After two weeks of heating, solid products were observed from the 0.5TPA/0.5TMA/C3 and 0.5TPA/1.0TMA/C3 mixtures, whereas the mixture with the highest TMA content (i.e., 0.5TPA/1.5TMA/C3) remained optically transparent, indicating suppression of zeolite formation due to the TMA. These collected solids were further analyzed to verify phase purity. The PXRD data in Figure 5-1a shows that the products obtained from TPA-TMA-silica mixtures are pure MFI-type materials. Figure 5-1b shows the weight loss curve of the products from 0.5TPA/ *x* TMA/ C3 (x = 0.5, 1.0) and 0.5TPA/C3 mixtures versus temperature. For all samples approximately 12 % weight loss in the temperature range 360-650 ^{o}C is observed due to the thermal decomposition of the organocation. The amount of the organic template corresponds to four TPA molecules per unit cell, indicating the zeolite forms with the ideal unit-cell composition $[(TPA)_4(SiO_2)_{96}]$. In addition, the two TPA-TMA-silica mixtures show a weight loss of approximately 2 wt % in the temperature range 25-350 ^{o}C. This weight loss is attributed to physically adsorbed water and organocation on the outer crystal surface. The results above indicate that silicalite-1 crystals can be synthesized from TPA-TMA-systems with limited TMA concentration. [149] Figure 5-2 shows the SEM micrographs of silcalite-1 formed in pure TPA-silica mixtures and TPA-TMA silica mixtures. All crystals are large (~10 μm) with high length/width ratio, consistent with previous reports on the growth of elongated flat crystals from synthesis mixtures with high H_2O/SiO_2 ratio and limited TPA concentration.[66, 138] The crystals formed in the mixed organocation systems are less uniform than those prepared from pure-TPA systems, indicating a possible influence of TMA on the crystal morphology beyond inhibiting the growth of silicalite-1. These TPA-TMA-silica mixtures were subjected to detailed measurements to study how the addition of TMA affects TPA silicate interactions before and at the early stages of heating.

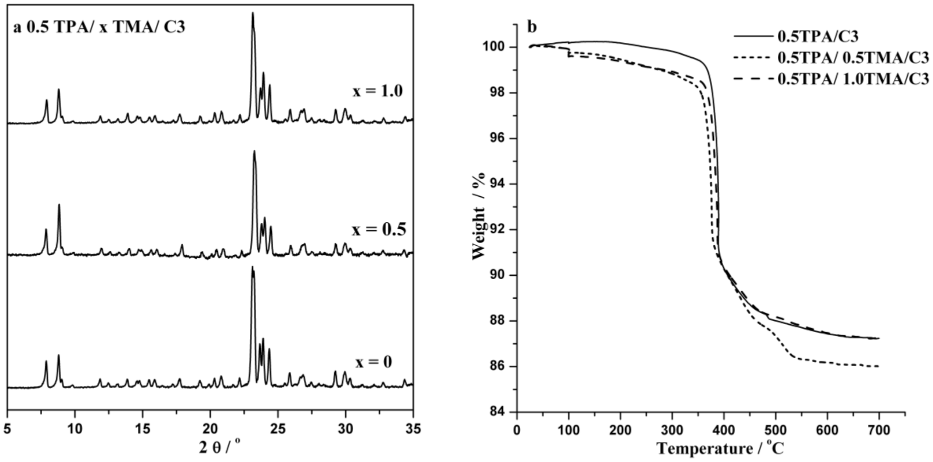

Figure 5-1. (a) PXRD pattern and (b) TGA traces of solids obtained from 0.5 TPA/ *x* TMA /C3 mixtures (*x*= 0, 0.5, 1.0) heatedat90 ^{o}C for two weeks.

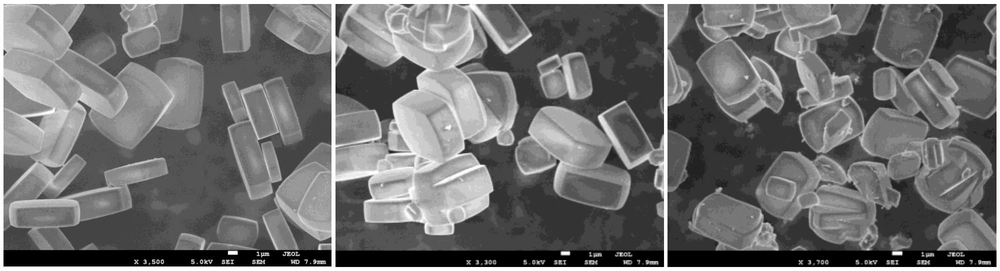

Figure 5-2. FE-SEM images of solids synthesized from (left) 0.5 TPA/C3, (center) 0.5 TPA/0.5 TMA/C3, and (right) 0.5 TPA/1.0 TMA/C3 mixtures. (Scale bar is 1μm in all images.)

Figure 5-3 shows the particle size distribution of the mixed organocation-silica mixtures and TPA-silica mixture heated at 90 °C for 24 hours.

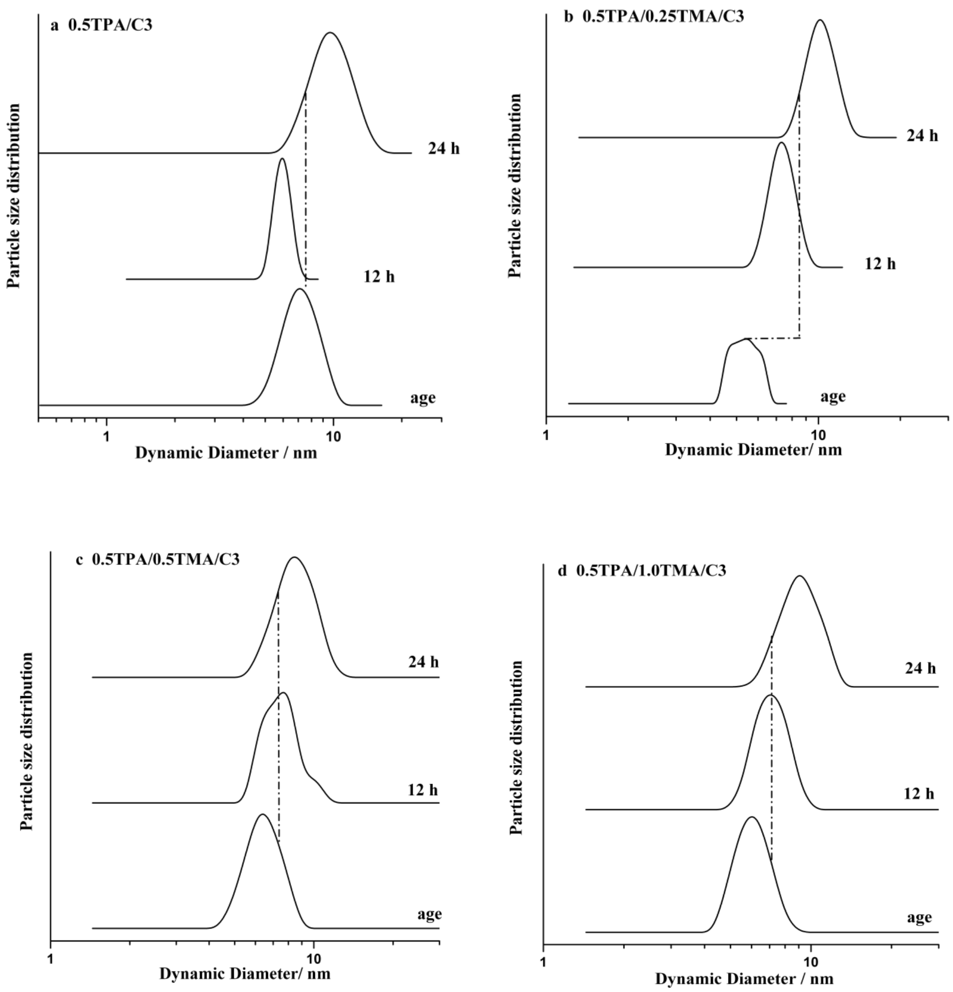

Figure 5-3. Particle size distribution obtained from DLS data of organocation-silica mixtures prepared with deuterated water and heated at 90 °C for 24h (a) 0.5 TPA/C3; (b) 0.5 TPA/0.25 TMA/C3; (c) 0.5 TPA/0.5 TMA/C3; (d) 0.5 TPA/1.0 TMA/C3.

As shown in Figure 5-3, the presence of primary particles with a diameter of approximately 6 nm was found in all samples prior to heating and a slight increase in the particle size to approximately 5-10 nm is observed during heating Also, the population of these heated primary particles remains high and stays stable for the first 24 hours.

These above observations are consistent with previous studies on TPA-TEOS-H_2O systems upon hydrothermal treatment. [78, 147]

5.3.1 ^{1}H NMR of TPA-TMA-Silica Mixtures at Room Temperature

The work reported in Chapter III investigated the silica nanoparticle-TPA interactions in TPA-silica and TMA-silica mixtures. The aim of the present chapter is to quantify how the addition of TMA to the TPA systems affects the TPA-silica interactions and thus zeolite formation. TMA was chosen as the additional cation because it is more hydrophilic and is incapable of making pure silica-zeolite from clear solutions whereas TPA can direct silicalite-1 formation after 24 hours of heating. It is expected investigations on the mixed organocation systems should provide insights related to how the silica-organocation interactions affect zeolite growth. Figure 5-4 shows the ^{1}H NMR spectra of the TPA/TMA mixtures with fixed TPA content at room temperature. No apparent changes in the TPA resonances (3.13, 1.68, 0.95 ppm) were observed. The only change in the TMA resonance (3.23 ppm) was the expected increase in intensity upon increasing the TMA content.

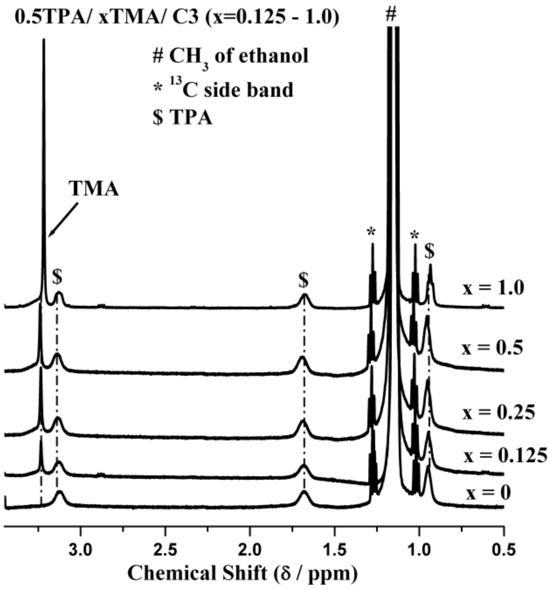

Figure 5-4. ^1H NMR spectra of 0.5 TPA/C3 and 0.5 TPA/*x* TMA/ C3 (*x* =0.125, 0.25, 0.5, 1.0) mixtures at room temperature prior to heating.

Given that PFG NMR data can be extended to 2D DOSY spectra with chemical shifts on one axis and self-diffusivity on the other, the diffusion coefficients of TPA and TMA in the same mixture can be obtained simultaneously (data processing and corresponding DOSY spectrum of the 0.5TPA/0.25TMA/C3 mixture at RT is shown in subsection 2.2. Also to simplify the data analysis, mixtures were chosen where the TPA content is less than the value at full surface coverage (~ 9.2mM) shown in Chapter III. Figure 5-5 shows the observed diffusion coefficient (D_{obs}) of TPA and TMA versus moles of TPA for various TPA-TMA-silica mixtures. As can be seen in Figure 5-5a, the diffusion coefficients of TPA increase with increasing TPA concentration and ultimately plateau at the highest TPA amount (*y* = 1.25). Also, the observed diffusion coefficient systematically increases for a given TPA content as the TMA content increases. This result is consistent with the TMA displacing TPA from the nanoparticle surface. The

TMA results (see Figure 5-5b) indicate the TMA self-diffusion coefficient is relatively insensitive to the TPA content. The diffusion coefficients of TPA and TMA in water-ethanol mixtures are 4.0 x 10^{-10} m^2/s and 7.6 x 10^{-10} m^2/s, respectively (see Chapter III). Thus the results in Figure 5-5 indicate that TMA has a significantly reduced diffusion coefficient in the presence of silica and TPA as compared to TPA.

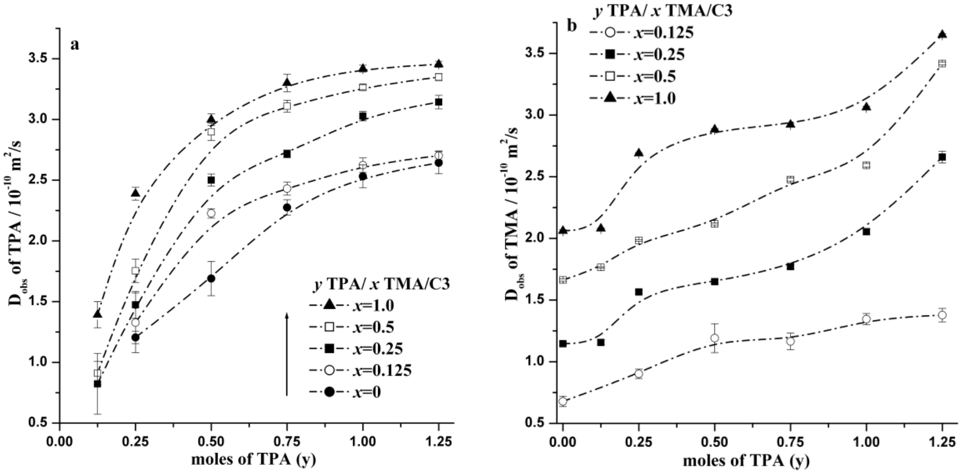

Figure 5-5. Observed diffusion coefficients (D_{obs}) of (a) TPA and (b) TMA in a series of TPA-TMA-silica mixtures as function of TPA content.

Since the chemical exchange of organocations between the free and bound state is fast compared with the diffusion time (see Figure 3-7), the measured diffusion coefficient (D_{obs}) is an averaged value of the two sites and can be described as equation 3-1shown in Chapter III:

$$D_{obs} = f_b D_b + f_f D_f \tag{5-1}$$

where the subscripts *b* and *f* denote the bound and free species, respectively. The value of the free diffusion coefficient (D_f) was estimated from the diffusion coefficient of TAA cations in water/ethanol mixtures with a composition equivalent to the C3 mixture without silica. The bound diffusion coefficient (D_b) can be estimated from DLS measurements of silica mixtures C3 (0.626 ± 10^{-10} m^2/s). The PFG NMR combined with the DLS results above can be used to calculate the fraction of bound TAA and thus the concentration of bound TAA can be calculated by equation 3-2 show in Chapter III:

$$[TAA]_{bound} = f_b [TAA]_{total} \tag{5-2}$$

Figure 5-6 shows the bound fraction (f_b) of TPA and TMA as a function of TPA content of the mixtures shown in Figure 5-5. An approximately 20 % decrease in the bound fraction of TMA is observed for 1.0TMA/ *y* TPA/ C3 mixtures whereas the bound fraction of TPA decreases significantly. A simple interpretation of Figure 5-5 and Figure 5-6 is that TMA displaces TPA from the nanoparticle surface.

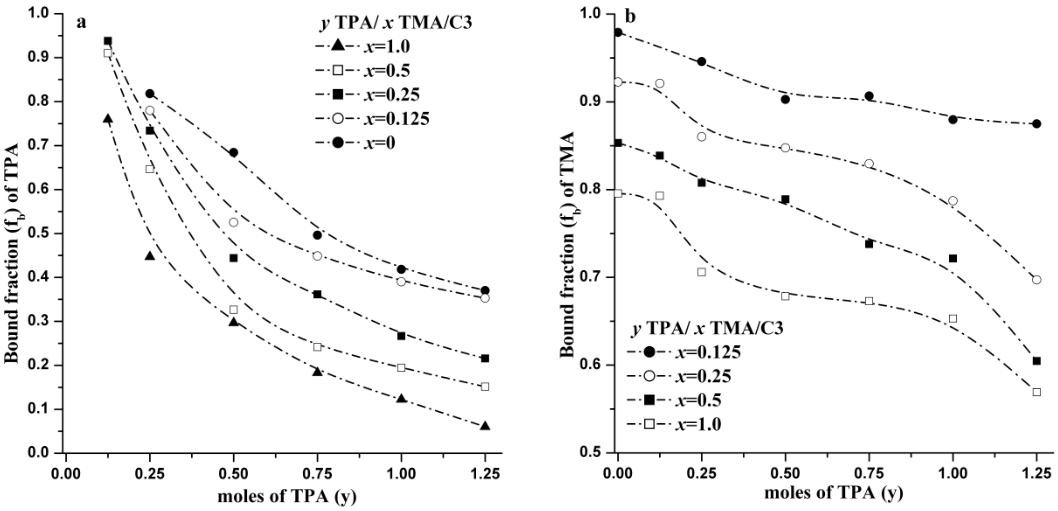

Figure 5-6. Bound fractions (f_b) of (a) TPA and (b) TMA in a series of TPA-TMA-silica mixtures as a function of TPA amount.

Figure 5-7a shows the concentration of bound TPA versus total TPA concentration (i.e. binding isotherms) for the TPA-TMA-silica mixtures. The addition of more TMA significantly decreases the amount of TPA adsorbed compared with pure TPA systems (*y* TPA/C3) having the same total TPA concentration, which is reflected in the initial slope of the isotherms. While silicate speciation is known to depend in part on the organocation identity, [150, 151] the most likely effect of the added TMA is to compete with TPA for adsorption sites on the nanoparticle surface. This would be consistent with DLS data that does not show any substantive differences between the particle size distributions/populations for the various samples. To quantify this effect, the binding isotherm data in Figure 5-7 was analyzed using the Langmuir isotherm model:

$$\Gamma = \frac{\Gamma_{\max} K C_f}{1 + K C_f} \tag{5-1}$$

where Γ and Γ_{max} are the amount of adsorbed TPA in mixtures shown in Figure 5-7a and the value at maximum coverage, C_f is equilibrium concentration of free TPA in solution, and K is the adsorption equilibrium constant. The details of the model fits are shown in Figure 5-7b.

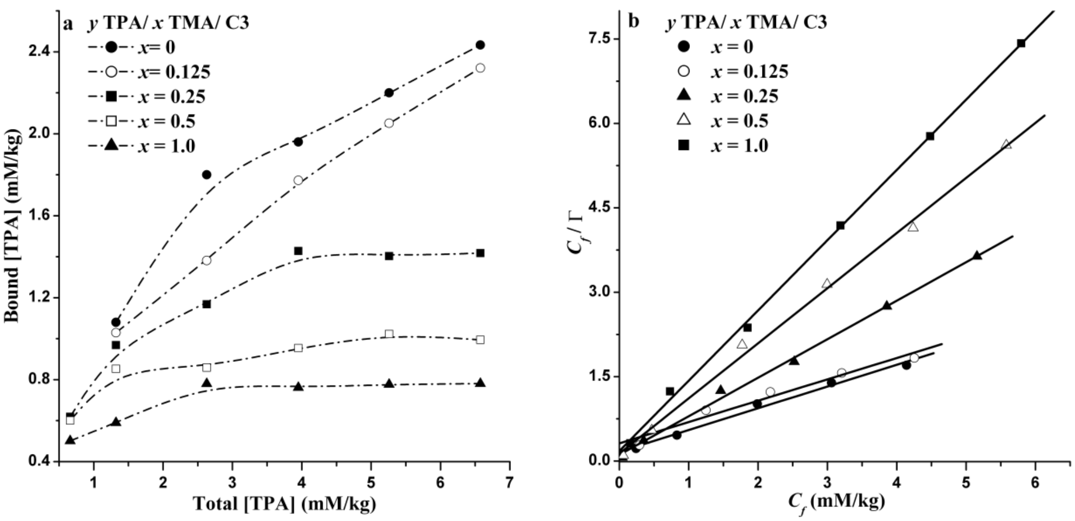

Figure 5-7. (a) Binding isotherms of TPA in a series of TPA-TMA-silica mixtures at room temperature and (b) the corresponding Langmuir isotherm fit.

Figure 5-8 shows a plot of Γ_{max} and K as a function of the amount of TMA added. As can be seen the Γ_{max} of TPA decreases rapidly with addition of TMA and gradually converges to a constant value. This result is consistent with less TPA being adsorbed on the nanoparticles with increasing TMA content. This indicates that TMA is displacing TPA off the nanoparticle surface, consistent with our previous results that indicate TMA binds more strongly than TPA. However, the adsorption constant K displays the opposite trend by increasing with increasing TMA content. While this result at first appears counterintuitive, one interpretation is that the TPA which remains on the surface is the most strongly bound TPA, and that leads to an increase in *K*. In the most cautious interpretation, the results in Figure 5-8 indicate that TMA can effectively displace TPA off the surface of the nanoparticles, which shows that the TMA-silica complexes are more stable than TPA-silica complexes.

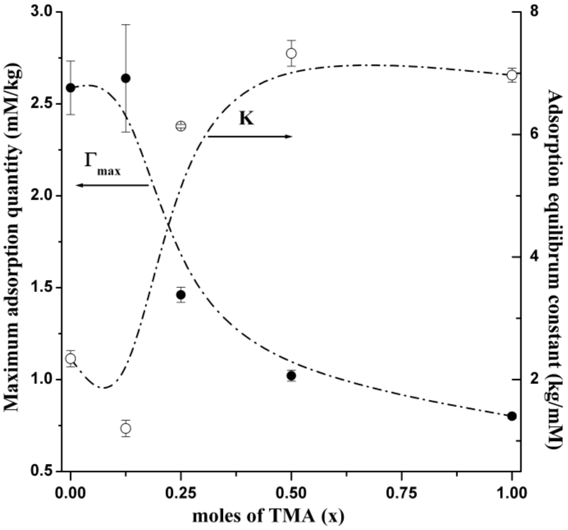

Figure 5-8. $\Gamma_{\max}$ and K for TPA as a function of the TMA concentration in TPA-TMA silica mixtures.

5.3.2 ^{1}H NMR of TPA-TMA-Silica Mixtures upon Heating

To investigate the stability of these systems further mixtures were heated at 90 °C and then analyzed by PFG NMR. Figure 5-9 shows the observed diffusion coefficient (D_{obs}) of TPA and TMA as a function of heating time for 0.5TPA/ *x* TMA/ C3 mixtures

(x = 0-1.0) shown in Figure 5-4. As shown in Figure 5-9a, the diffusion coefficients of TPA as a function of time for the TPA-TMA-silica mixtures are qualitatively similar to the 0.5TPA/C3 sample, with the difference that the diffusion coefficient of TPA in the mixed organocation mixtures increases with increasing TMA content. While there is an increase of the TMA diffusion coefficient observed (see Figure 5-9b), the increase relative to the diffusion coefficient of free TMA (7.5×10^{-10} m^2/s) is much smaller than that for TPA, implying that a much higher fraction of TMA remains associated with the nanoparticles upon heating. Consistent with this the TPA diffusion coefficient after 24 hours heating is above 90% of the TPA free value (~ 4×10^{-10} m^2/s), whereas for TMA the diffusion coefficient of the same mixtures is below 50% of its free value (~7.25-7.82× 10^{-10} m^2/s). Also noteworthy is that the diffusion coefficient of TPA at a given time increases due to the addition of more TMA since the TPA content is fixed in these heated mixtures. In contrast, after a sharp increase in the first few hours of heating, the diffusion coefficient of TMA is relatively constant.

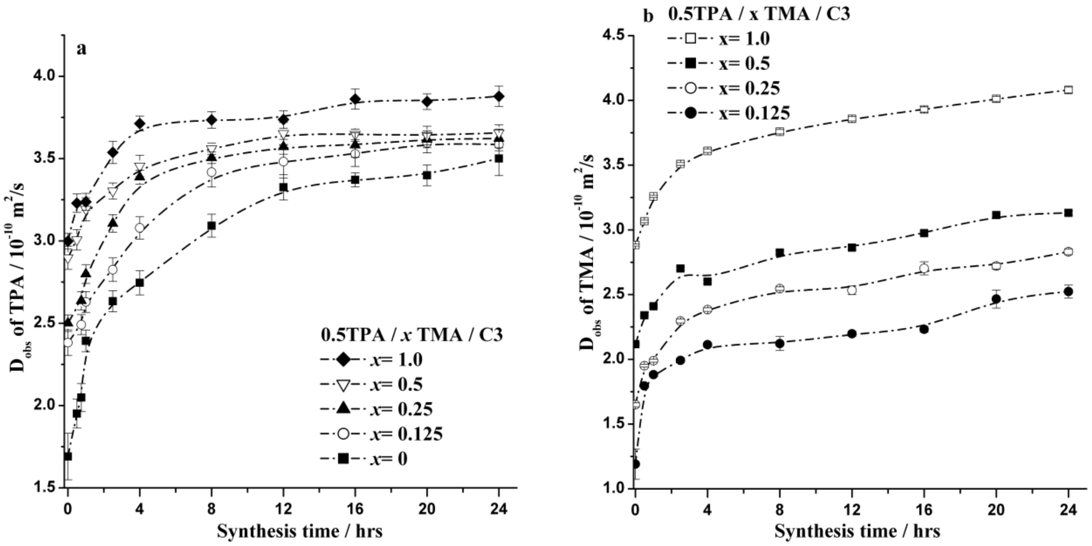

Figure 5-9. Observed diffusion coefficients (D_{obs}) of (a) TPA and TMA (b) as a function of heating time for TPA-TMA-silica mixtures.

The fraction of bound TPA and TMA as a function of time could be calculated through analyzing these heated mixtures using the two-site model. Given the increasing precursor particle sizes shown in the DLS results, how the particle size (which changes from approximately 6 to approximately 10 nm during) influences this analysis was studied. The results are shown in Figure 5-10, and perhaps surprisingly the fraction of bound cation (f_b) is insensitive to variations of D_b over this size range.

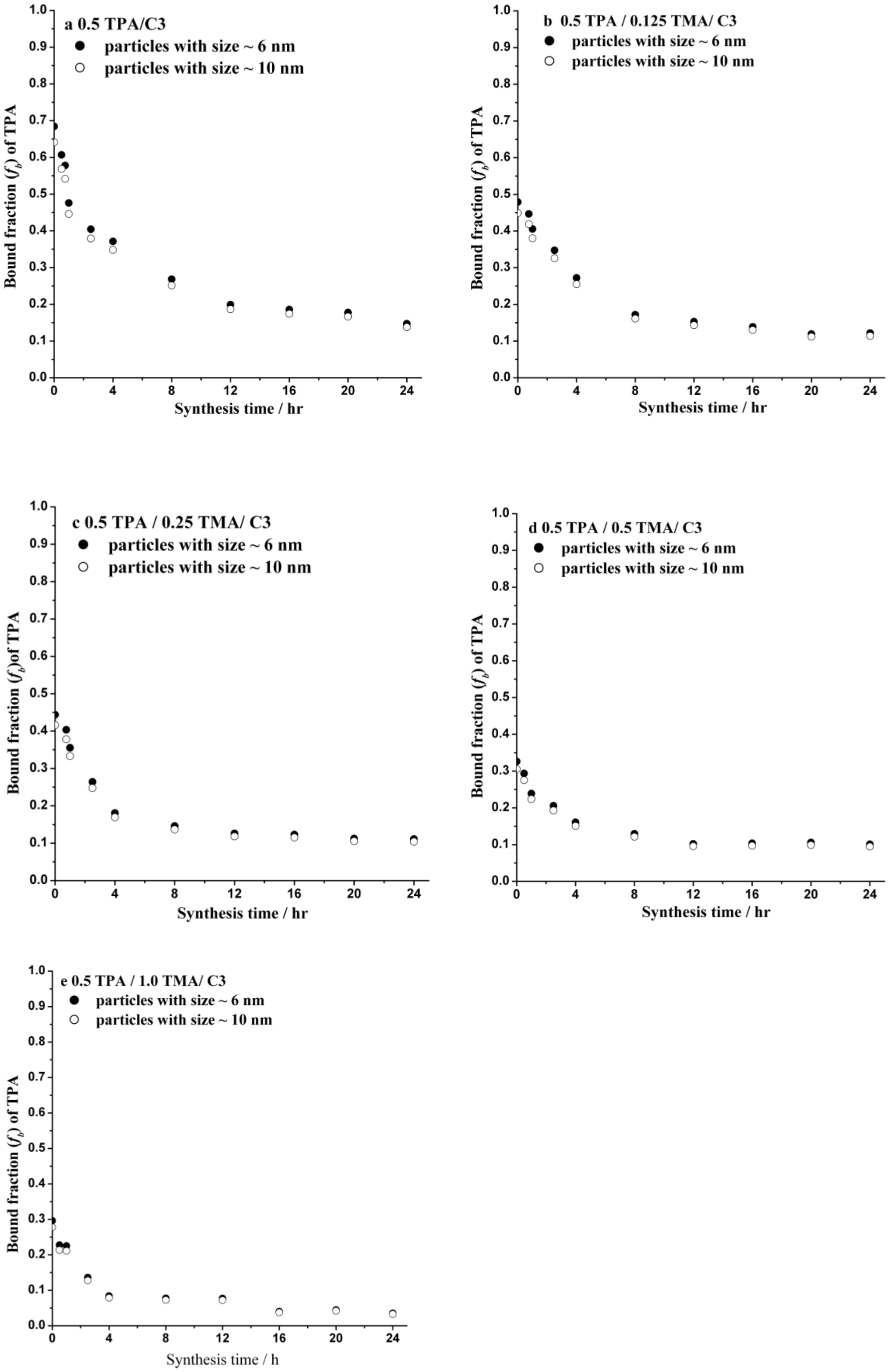

Figure 5-10. Comparison of Bound fraction (f_b) of TPA calculated on the basis of different particle sizes in 0.5 TPA/ *x* TMA/ C3 mixtures (clock wise from left to right) *x* = 0, 0.125, 0.25, 0.5 and 1.0. (Solid circle denote analysis if all particles are ~6 nm in diameter, and the hollow circle denote analysis if all particles are ~ 10 nm in diameter.)

Figure 5-11 shows the fraction of TPA and TMA bound to the precursor particles as a function of heating time for the mixtures shown in Figure 5-9. This analysis indicates that in the absence of TMA, there is a pronounced decrease in the fraction of bound TPA upon heating. In the presence of TMA the decrease in the fraction bound is not as pronounced given that the initial fraction bound is much lower. The latter point is consistent with fewer bound TPA cations before heating in the presence of TMA. The f_b value of TMA decreases with time yet the decrease only varies between 15% and 20%, far less than that of TPA (note scales in Figure 5-11). This difference indicates the TPA cations are less strongly associated with the nanoparticles and thus are more easily displaced than adsorbed TMA cations upon heating.

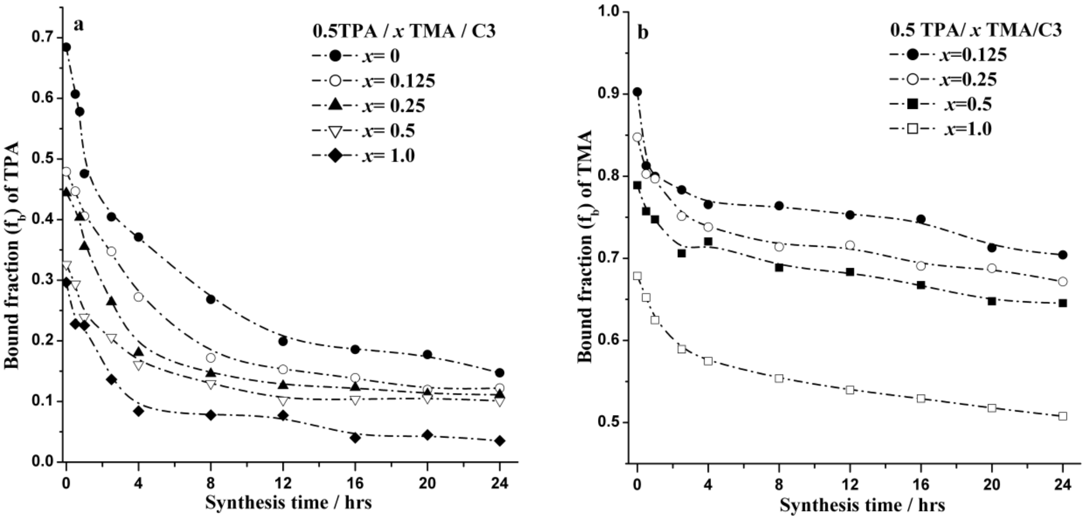

Figure 5-11. Bound fraction (f_b) of (left) TPA and (right) TMA as a function of heating time in TPA-TMA-silica mixtures.

Upon heating the nanoparticles undergo a complex process of dissolution, aggregation, and restructuring. One would anticipate that for these events to take place that the organocations must first desorb. The work above indicates that TMA can effectively displace TPA from the nanoparticle surface, and that more TMA remains bound to the particles upon heating. With the results above it is now possible to obtain the amount of desorbed TPA in these TMA-TPA-silica mixtures as a function of heating time from equation 4-2 as described in Chapter IV:

$$[TPA]_{des}^{i} = TPA_{total}\,(f_b^o - f_b^i) \qquad (4\text{-}2)$$

where f_b^i is the bound fraction shown in Fig. 5-10 and TPA_{des}^{i} is the desorbed amount of cations (mM/kg) calculated for each heating time (t). To further quantify the effect of added TMA on TPA desorption process, the amount of desorbed TPA as a function of heating time for 0.5TPA/ *x* TMA/C3 samples (*x* = 0-1.0) was calculated via eq 4-2 and fitted with the pseudo-second-order kinetic model (equation 4-3b).

$$\frac{t}{q_t} = \frac{1}{k_d q_e^2} + \frac{1}{q_e} t \qquad (4\text{-}3b)$$

where $q_t = TPA_{des}^{i}$, k_d is the desorption rate constant in $(\text{mM/kg})^{-1}$ h^{-1} and q_e is the equilibrium desorption capacity with units of mM/kg. The parameters obtained from fitting these models are shown in Table 5-1. R^2 values of the pseudo-second-order kinetic model fit vary between 0.97 and 0.99, indicating that the experiments results fit this model well. Figure 5-12 shows the linear plots of t/q_t versus time t of TPA-TMA-silica mixtures heated at 90 ^{o}C, from which the TPA desorption rate constant (k_d) as a function of added TMA concentration can be obtained. Given that the structure and composition of the nanoparticles is dynamic during heating, the concept of an ‘equilibrium’ between adsorbed and desorbed cations upon heating must be treated with some caution.

Table 5-1. Fitting results for TPA desorption in TPA-TMA-silica mixtures using pseudo-second-order kinetic models.

mole of TMA (*x*)	R^2	σ	P-value
0	0.987	0.684	<0.0001
0.125	0.966	1.574	<0.0001
0.25	0.969	1.675	<0.0001
0.5	0.990	1.429	<0.0001
1.0	0.990	1.292	<0.0001

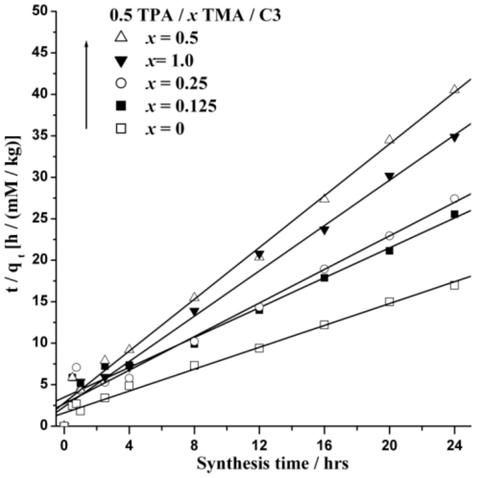

Figure 5-12. Pseudo-second-order kinetic plots of TPA desorption of TPA-TMA-silica mixtures.

To remove potential artifacts related to different TAA concentrations, TPA-silica mixtures with TPA content equivalent of the total moles of organocations in mixed TPA-TMA systems were used as a comparison and the desorption rate constant (k_d) of desorbed TPA for pure TPA-silica mixtures are shown in Figure 5-13. As can be seen, the k_d value for TPA-TMA mixtures increases with addition of more TMA whereas the values for pure TPA-silica mixtures are insensitive to TPA concentration over the measured range. This observation is consistent with the premise that the TMA cations effectively displace TPA from the nanoparticle surface, and is also consistent with the Langmuir analysis. There are several possible origins for this. Perhaps the simplest explanation is that TMA has a higher charge density than TPA and thus electrostatic effects are responsible for the observed preferential adsorption of TMA. Alternatively, given the dynamic structure and composition of heated primary particles, steric effects or the more hydrophilic nature of TMA is responsible for the observed results. Perhaps the most significant observation is that TMA appears to stabilize the nanoparticles during heating more strongly than TPA, and that may be one of explanations for the failure to make silicalite-1 from the mixed organocations samples with moles of TMA (x) above 1.0. More generally, the kinetic analysis of TMA and TPA in the same heated mixture using PFG NMR could be applied for studying porous materials formation assisted by dual-surfactant templates in a noninvasive way. One possible contribution to the difficulty of making siliceous zeolites in nanoparticle form from clear solution could be that some of the organocations stabilize the precursor particles too strongly, and thus the type of aggregation invoked by others cannot take place.

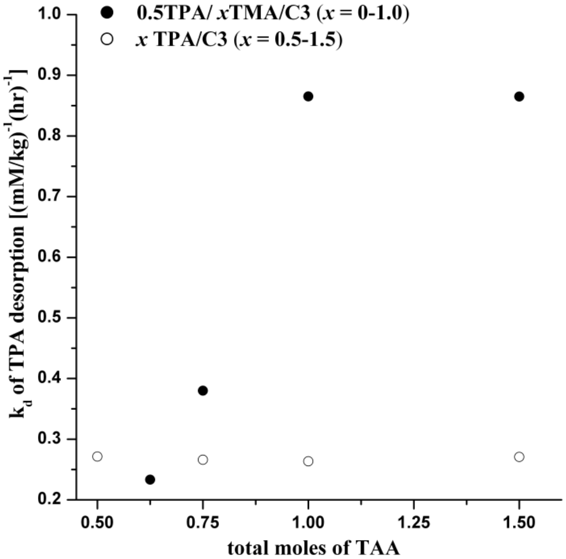

Figure 5-13. Comparison in TPA desorption rate constant (k_d) in TPA-TMA-silica mixtures and TPA silica mixtures.

5.4 Conclusions

^{1}H PFG NMR results of TMA-TPA-silica mixtures at room temperature show that the measured self-diffusion coefficient of TPA increases significantly with TMA addition whereas the effect of TPA content on diffusion coefficient of TMA is minor. Analysis of the PFG data with a two-site model and Langmuir adsorption formalism shows a decrease in the adsorbed amount of TPA upon increasing TMA content, indicating the TMA displaces TPA from the nanoparticle surface. Upon heating the diffusion coefficient of TPA increases in both pure TPA-silica and TPA-TMA-silica mixtures, suggestion less bound TPA and a kinetically controlled desorption of TPA from the nanoparticles. However, TPA desorption rate increases with TMA addition whereas this value remains constant upon increasing TPA content in the absence of TMA. This result indicates that TMA has a promoting effect on the desorption kinetics of TPA. Taken together, the PFG NMR results present a quantitative comparison of TPA-silica nanoparticle interactions in mixed organocation systems to that in pure TPA-silica mixtures. These findings should further advance knowledge in the field of zeolite synthesis.

CHAPTER VI

SPECIFIC ION EFFECTS ON TETRAALKYLAMMONIUM (TAA)-SILICA NANOPARTICLE INTERACTIONS*

6.1 Introduction

In this chapter, the effects of salt on the stability of TAA-silica nanoparticles and further on the organic-inorganic interactions were investigated. Also a comparison of the adsorption equilibrium of tetramethylammonium (TMA) and tetrapropylammonium (TPA) on the silica particles during salt-induced aggregation is presented and various responsible interactions are discussed. The corresponding results provide implications for the colloidal properties of these primary particles and chemistry of aqueous silica involved in the aggregative growth mechanism for formation of zeolite crystals.

6.2 Experimental

6.2.1 Sample Preparation

Siliica mixture C3, TPA-silica and TMA-silica mixture added with various LiCl, NaCl, CsCl are prepared as described in subsection 2.7.4.

---

*Reproduced with permission from “Specific ion effects on nanoparticle stability and organocation-particle interactions in Tetraalkylammonium-Silica mixtures” by Li, X and Shantz, D. F. *Langmuir*, **2010**, *26*, 18459-18467. Copyright 2010 American Chemistry Society.

6.2.2 Analytical

Solution pH and conductivity, Dynamic Light Scattering (DLS) and NMR measurements were performed as described in subsection 2.2-2.5.

6.3 Results

6.3.1 pH and Conductivity

The addition of electrolytes can induce particle aggregation by screening the electrostatic repulsion between the charged nanoparticles in silica mixtures, leading to variations of solution conditions. The pH and conductivity of nanoparticle solutions (C3) with chlorides of Li^+, Na^+, Cs^+ were measured and the results are shown in Figure 6-1. A slight decrease in pH value with increasing salt concentration was observed for all three salts, consistent with previous studies that show a decrease of pH in sodium silicate mixtures with salt addition.[90] The drop of hydroxide concentration could be caused by silanol dissociation of soluble silica in the aqueous phase to form large polysilicates or nanoparticles with more SiO_2 units. Also shown in Figure 6-1 is the ionic conductivity of the mixtures increases monotonically upon addition of salts.

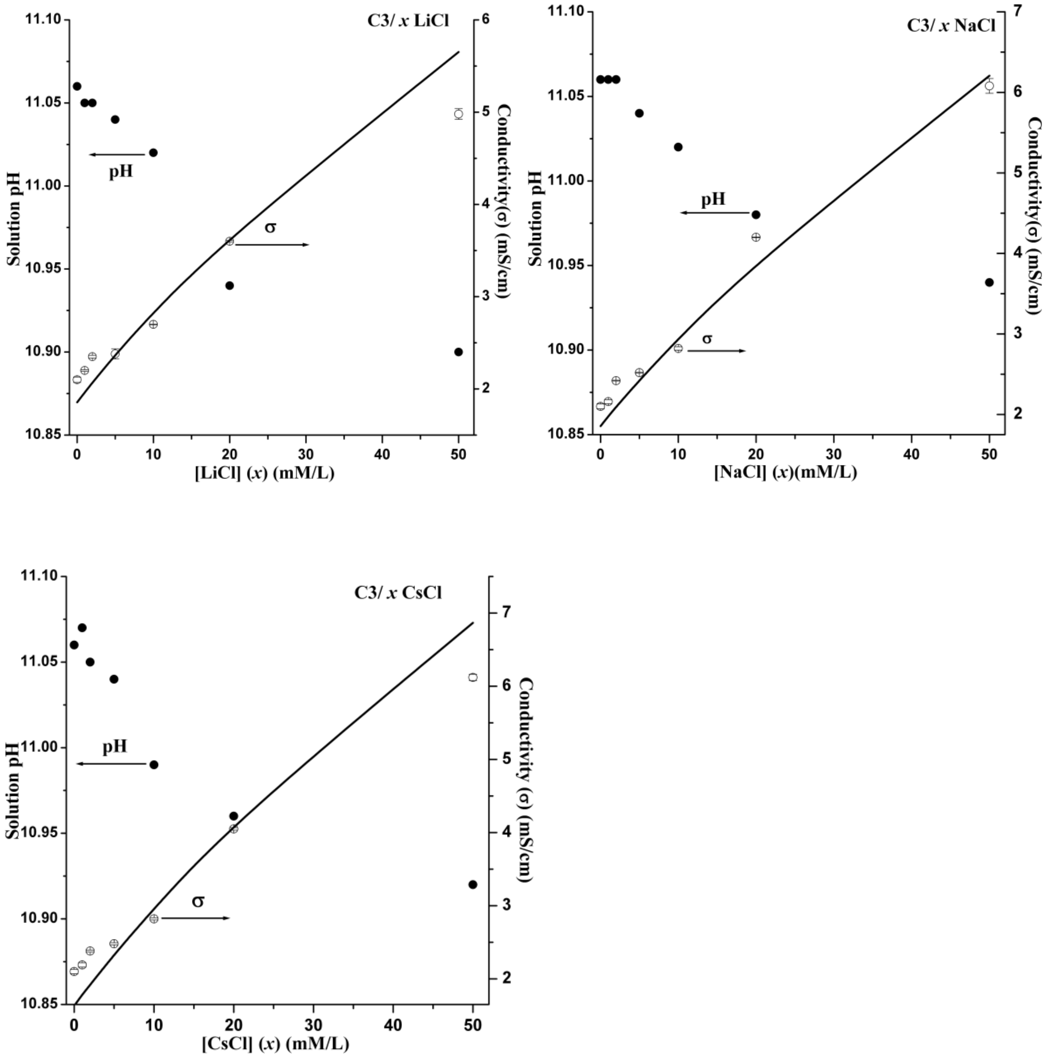

Figure 6-1. pH and conductivity of silica mixtures with various salts as a function of salt concentration. The solid curve represents the predicted conductivities obtained from equation 6-1 using the measured pH values.

To quantify the change in conductivity, the predicted conductivity for various salts is calculated from a variation of the Shedlovsky equation using the measured pH value.[152, 153]

$$\sigma = \sum \lambda_i C_i - \sum (A + B\lambda_i) C_i^{1.5} + \sum D \cdot C_i^{\alpha} \qquad (6\text{-}1)$$

where C_i is the concentration of a charged ion and λ_i is the corresponding limiting molar conductivity. The value of λ for charged silica is difficult to determine experimentally due to the presence of various oligomers as well as their low mobility.[154] Thus only OH^- and the monovalent ions, i.e, Li^+, Na^+, Cs^+ and Cl^-, are considered for analysis and their λ values are shown in Table 6-1. The constants A and B are the Debye-Huckel-Onsager coefficients for an aqueous solution with values of 60.2 (mS/cm)$(\text{mol/L})^{-1.5}$ and 0.23 $(\text{mol/L})^{-1.2}$ respectively. [155] The empirical constants D and α are obtained from fitting conductivity values of NaOH solutions with various salts (see Figure 6-2) using equation 6-1 and pH value of these solutions (see Table 6-2). The obtained constant D and α values for the C3 mixtures with NaCl and LiCl are -90.6 (mS/cm)$(\text{mol/L})^{-2.2}$ and 2.2, respectively, and for CsCl samples the values are -426.7 (mS/cm)$(\text{mol/L})^{-2.4}$ and 2.4. As shown in Figure 6-1, the deviations of experimental conductivity from calculated values at low salt concentration (2 mM) are likely due to a few charged soluble silica components, which are not expected to cause systematic errors in the measurements.

Table 6-1. Limiting molar conductivities of selected inorganic ions. [156]

Ion	λ_i ($mS \cdot M^{-1} \cdot cm^{-1}$)
Li^+	38.90
Na^+	50.10
Cs^+	77.26
OH^-	198.30
Cl^-	76.40

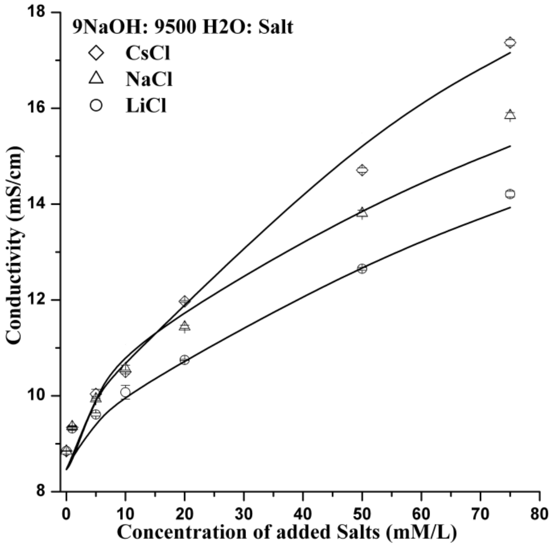

Figure 6-2. Nonlinear regression fits for conductivity of NaOH solution as a function of added salt concentration.

Table 6-2. pH values of NaOH solution with added salts.*

Added salt concentration (mM)	pH (LiCl)	pH (NaCl)	pH(CsCl)
0	12.59	12.59	12.59
1	12.60	12.6	12.59
5	12.62	12.62	12.67
10	12.63	12.63	12.67
20	12.62	12.63	12.70
50	12.62	12.62	12.72
75	12.62	12.62	12.74

*Solution temperature of pH measurements varies between 24.3 ~ 24.9 °C.

6.3.2 DLS Measurements

Dynamic light scattering (DLS) was performed on silica mixtures with differing concentrations monovalent salt to monitor the onset of particle aggregation. Figure 6-3 shows the particle size distribution of silica mixtures in the absence of salt and with salt concentrations of 5, 10, 50 mM. As shown in Figure 6-3, primary particles with a size of approximately 6 nm were observed, consistent with previous studies.[7, 73] No significant changes were observed in the size of the primary particles at 5mM salt concentration but a fraction of particles with a diameter of ~20 nm appears in 5mM CsCl sample. Upon addition of salt to 10 mM a second population of particle aggregates with size around 100 nm is observed in NaCl (Figure 6-3b) and CsCl (Figure 6-3c) samples and their number density rises significantly as the salt amount increases to 50mM. In addition, DLS results of LiCl samples (Figure 6-3a) show an increase in the primary particle size to 15 nm at 10 mM and a fraction of aggregates with a radius of approximately 50 nm in the sample with 50mM LiCl. Taken together, the above results indicate addition of the three salts above 5 mM can induce the aggregation of primary particles. The extent of aggregation is salt and concentration dependent as one would expect. According to the Hofmeister series [157], the ability of electrolytes to destabilize charged colloidal particles increases with increasing ionic size. Thus the silica nanoparticle stability should increase as $Cs^+ < Na^+ < Li^+$, which is confirmed by the particle size distribution shown in Figure 6-3. Despite the clear trend of salt-induced aggregation, it is difficult to distinguish the subtle salt effects at the beginning of aggregation using DLS. PFG NMR measurements were performed to measure the diffusion coefficients of TAA in these mixtures with various salts and the corresponding results are complemented with DLS, giving a quantitative analysis of the nanoparticle stability as well as TAA-nanoparticle interactions as functions of the type and amount of added salts.

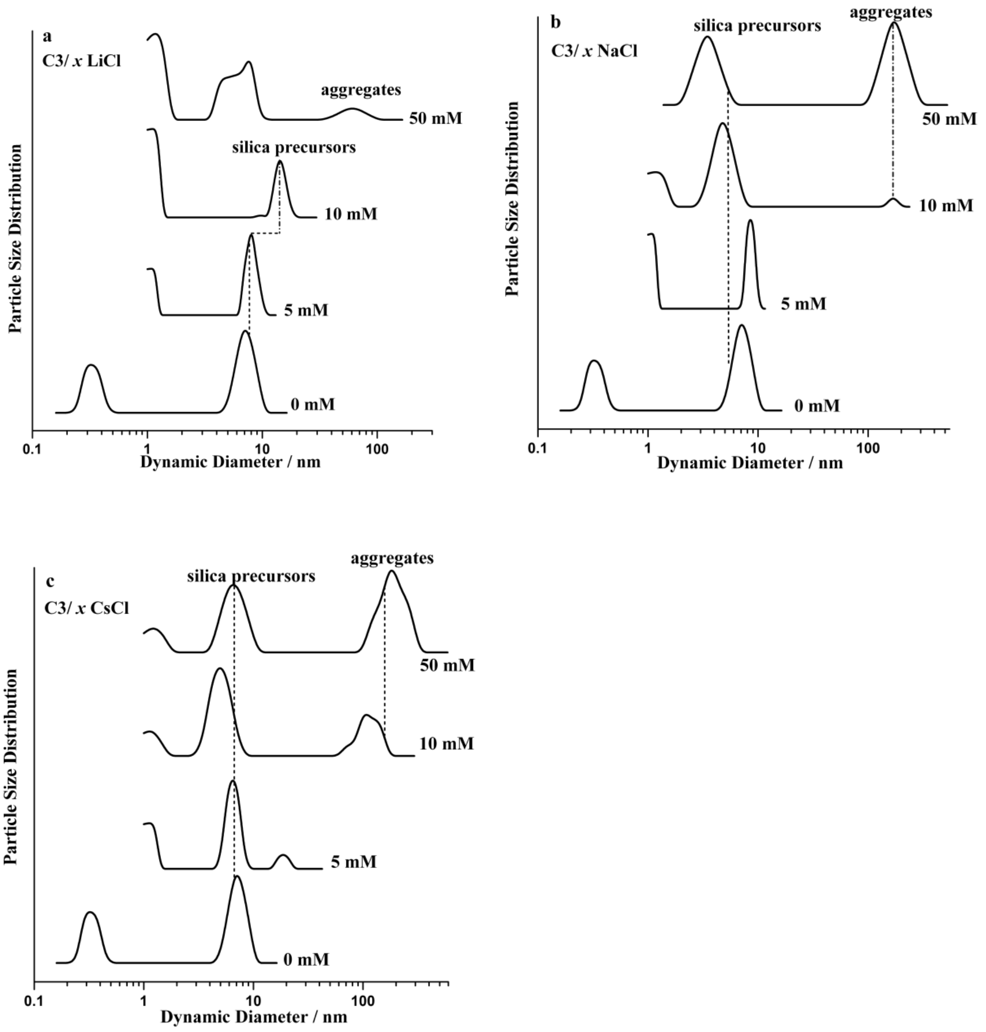

Figure 6-3. Particle size distributions obtained from DLS data of silica mixtures with (a-c) LiCl, NaCl and CsCl without organocations.

6.3.3 ^{1}H NMR

NMR measurements were performed on 0.25TPA/C3 and 0.25TMA/C3 mixtures to monitor the organocation upon addition of different electrolytes. TPA and TMA were chosen given the pronounced discrepancy in hydrophobicity/charge density of the two organocations, the TPA-particle interactions are expected to be quite different from the TMA-particle interactions under the same solution environment. The molar ratio of TAA versus silica is minimized in the silica mixtures based on the detection limit of NMR to maximize the bound fraction of organocations and hence the noticeable variation of the cation diffusion coefficient with addition of various salts. Another reason to investigate dilute TAA mixtures is that effect of the dilute TAA cations concentration (1.45mM/L) on total ionic strength of the solution mixtures is negligible compared with the effects of electrolytes. Figure 6-4 shows the ^{1}H NMR spectra of 0.25TAA/C3 samples with varying amount of salt. The resonances assigned to TPA cations in the mixtures are at 3.13, 1.68, and 0.95 ppm and TMA cations show a singlet at 3.25 ppm. As shown in Figure 6-4, the TAA resonances broaden due to binding of the organocations onto the silica nanoparticles. No pronounced change in the line widths and line intensity is observed upon addition of all three salts.

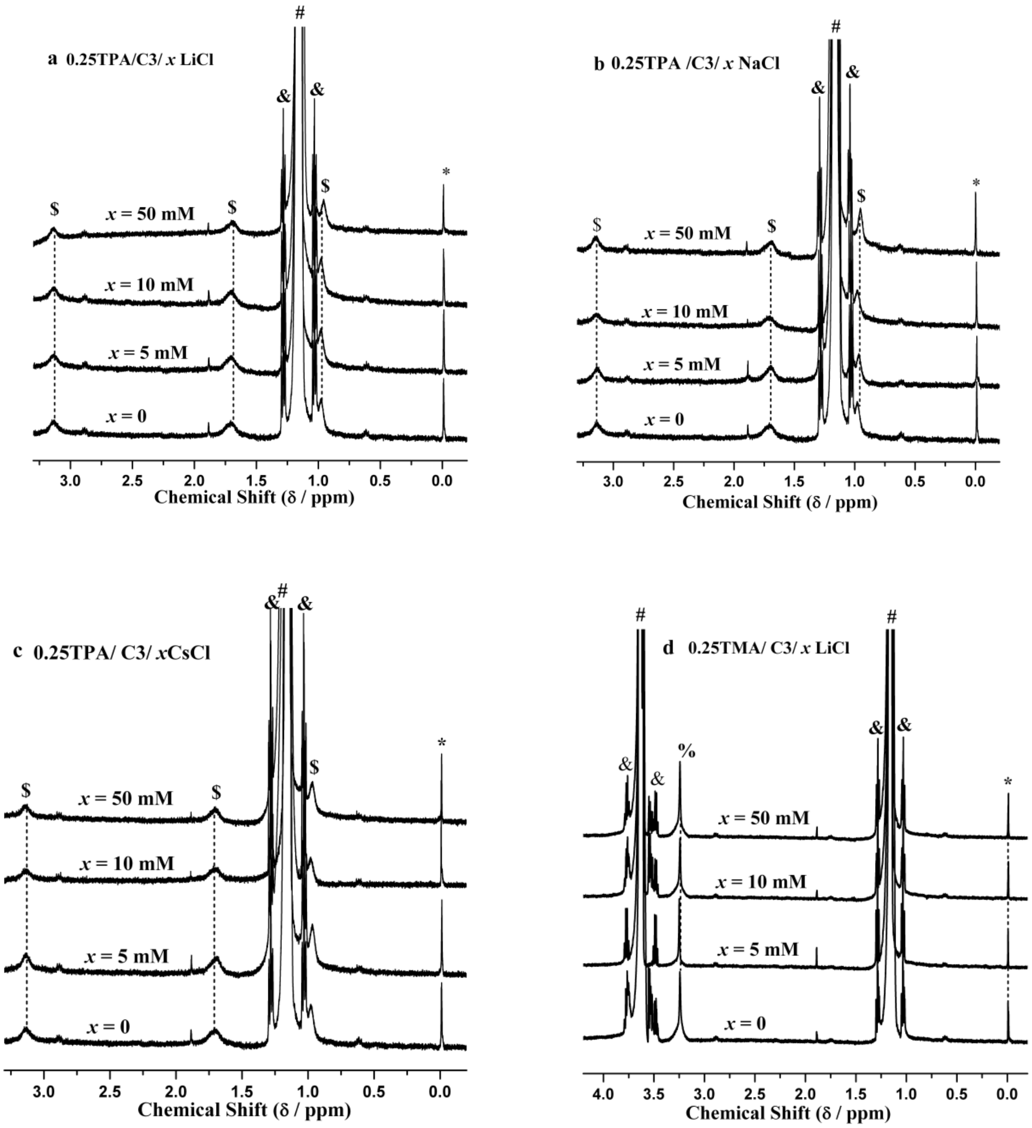

Figure 6-4. ^{1}H NMR spectra of 0.25 TAA/C3 mixtures in absence of salt and with salt concentration at 5, 10, 50mM. The *y*-axis is on the same scale. (a) ~ (c) 0.25 TPA/C3 with LiCl, NaCl and CsCl, respectively. For clarity, the ethylene group (3.63 ppm) of ethanol is not shown. (d) ~ (f) 0.25 TMA/C3 with LiCl, NaCl and CsCl (# ethanol; $ TPA; % TMA; & ^{13}C side band; * DSS).

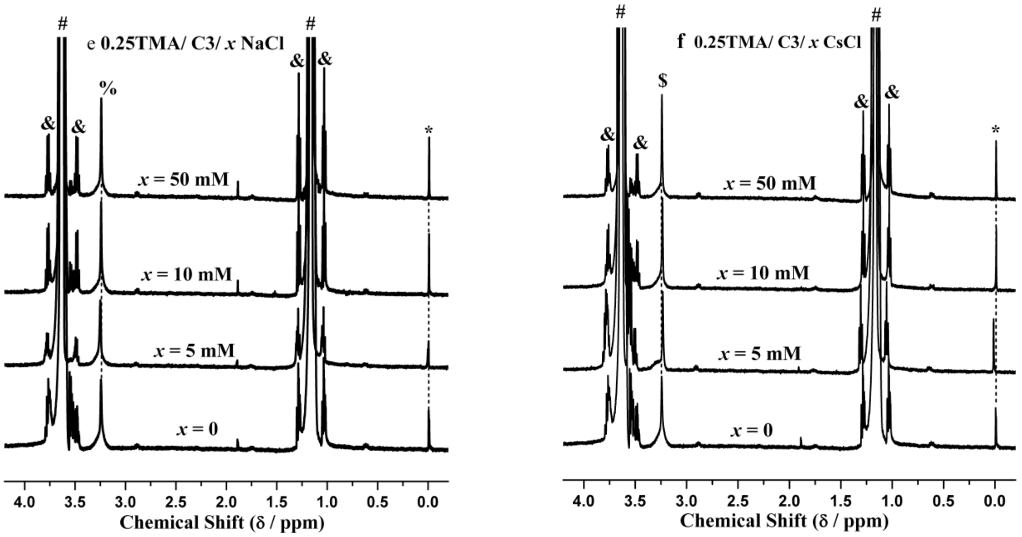

Figure 6-4. Continued.

The relative intensity ratios (R) of the methyl group of TPA (0.95 ppm) and TMA (3.25 ppm) versus the methyl group of DSS (0 ppm) (as internal standard) are plotted against various salt concentrations and shown in Figure 6-5. For the mixtures in absence of salt, the observed intensity ratios of TPA and TMA are 87 % and 97 % of their expected ratio, respectively, which indicates a negligible population of unobservable organocations. In general, the intensity ratios of both TMA and TPA increase upon addition of salt to 10 mM and then levels off. However the change in the measured intensity ratio is comparable to 10-15 % experimental error of NMR integration. Therefore, it is not clear why the ratio increases above the theoretical maximum of 3.3 for TPA and 5.0 for TMA, which is calculated based on the molar ratio of TAA/DSS and total number of protons in their methyl groups. One simple explanation would be the reduction of particle surface area and surface charge as a resultof salt induced aggregation that causes release of some adsorbed organocations to the solution. Therefore, an increase in the number of TAA cations not associated with the nanoparticles can lead to the increase of the NMR signal. PFG NMR is used to quantify the effect of added salt on TAA adsorption.

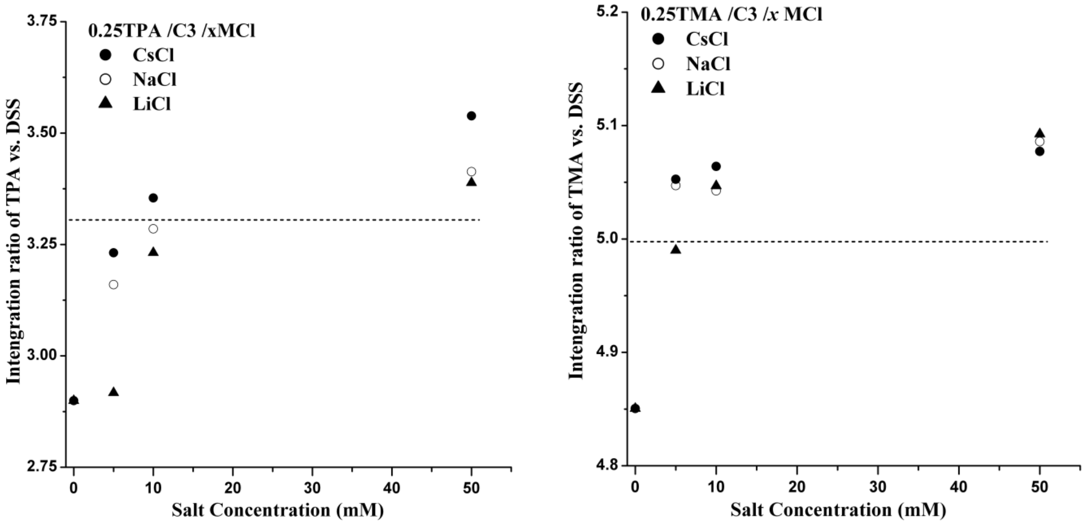

Figure 6-5. Relative intensity ratio (*R*) of TAA cations versus DSS in TAA/C3 mixtures as a function of added salt concentration. (Left) 0.25 TPA/C3/0.1 DSS samples and (right) 0.25TMA/C3/0.05DSS samples. (*R* is the ratio of integration area of the CH_3 group of TAA versus the CH_3 group of DSS. The dash line represents the theoretical *R* value (3.3 for TPA and 5.0 for TMA. The estimated variability in the values is between 10 and 15% due to the low concentration of TAA and DSS.)

Figure 6-6 shows the observed diffusion coefficient (D_{obs}) of TAA in 0.25TAA/C3 mixtures as a function of salt concentration. The figure shows that the observed self-diffusion coefficients both for TMA and TPA increase with increasing salt. It is also clear from Figure 6-6 that the self-diffusion coefficient of TPA is much more sensitive to added salt than TMA. Figure 6-6 also shows the diffusion coefficient is dependent on the identity of the salt at a fixed salt content with $Li^+ < Na^+ < Cs^+$. This correlates with the DLS results that showed CsCl led to the most silica aggregation, indicating a larger decrease in the number of nanoparticles in CsCl samples. A simple explanation for this is that the TPA is more effectively displaced from the nanoparticles than TMA in the presence of salt. The results in Figure 6-6 are not due to a dramatic difference in the aggregation state of the silica. DLS on 10 mM NaCl C3 mixtures containing 0.25 TMA and 0.25 TPA (Figure 6-3) indicates further aggregation of the nanoparticles as compared to the solutions without TMA or TPA, and so to a first approximation the number of aggregates in the TMA and TPA are similar. Thus the differences observed in Figure 6-6 are most likely due to the fact that TMA interacts more strongly with the silica nanoparticles than TPA.

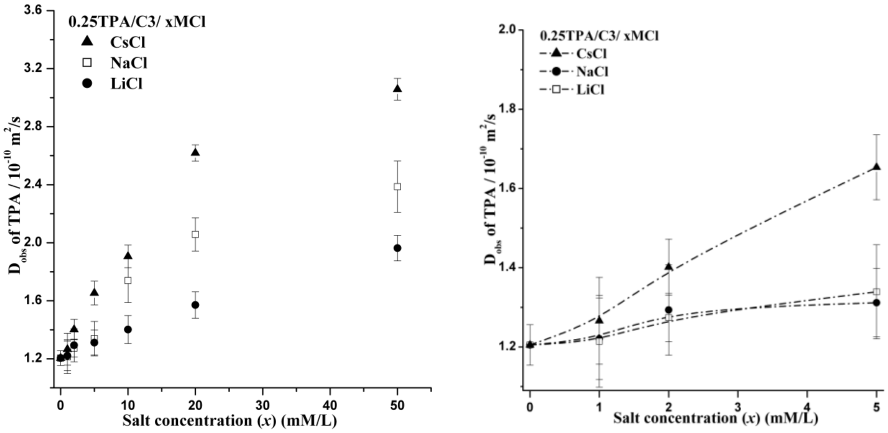

Figure 6-6. Observed diffusion coefficient (D_{obs}) of (top left) TPA and (bottom left) TMA as a function of salt concentration. (Top right) and (bottom right) are enlargements of the low salt concentration region of TPA and TMA.

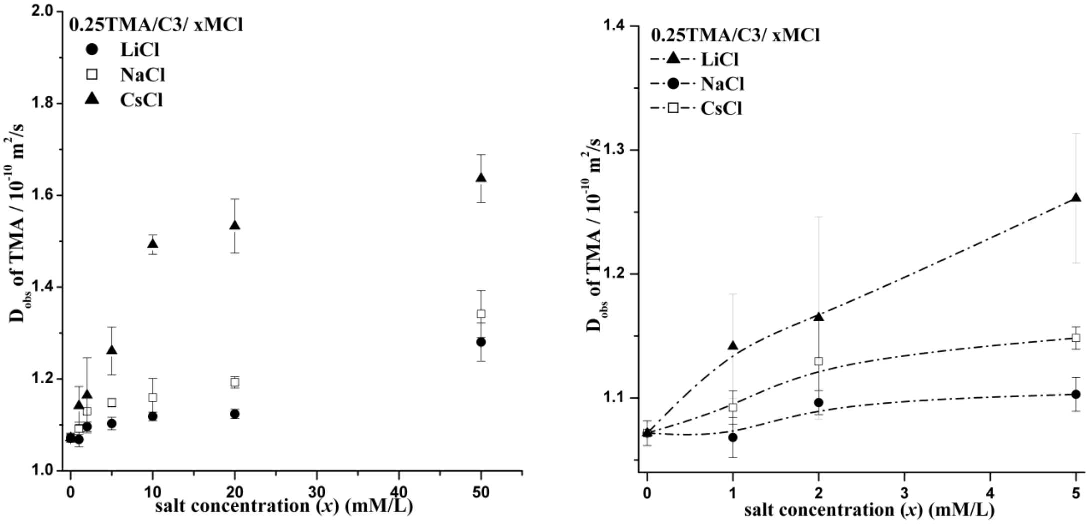

Figure 6-6. Continued.

Upon addition of salt based on the DLS results aggregation takes place. Further, particle restructuring could also be occurring given that the pH is changing. These factors potentially complicate the analysis of the NMR results in Figure 6-4. There are several factors that lead us to conclude that a two-state model of free cation and cation bound to the 5 nm nanoparticles will appropriately describe these systems. The first has to do with the fact that the rotational diffusion coefficient of 100 nm aggregates is slow on the NMR time scale. Thus we do not believe that organocations bound to the large aggregates will contribute to the NMR signal observed. This is consistent with the data in Figure 6-5, and also with the observation that these aggregates have a small surface to volume ratio as compared to the 5 nm particles (see Figure 6-3). Based on these points the analysis of the data in Figure 6-6 focuses on primary particles 5-10 nm in size. We have previously described the interactions between nanoparticles and organocations by a two-state model, wherein the organocation can be either free in solution or bound to the nanoparticle. PFG NMR measurements show that the diffusion coefficients of TAA measured as a function of Δ are essentially independent of diffusion time (within 5-10%) (see Table 6-3). Thus, exchange is fast on the NMR time scale and the measured diffusion coefficient (D_{obs}) is an average value of the two sites as described by equation 3-1 shown in Chapter III.

$$D_{obs} = f_f D_f + f_b D_b \tag{6-1}$$

where D_{f} and D_{b} are the diffusion coefficient of free and bound cations, and f_{f} and f_{b} represent the free and bound fraction, respectively. The value of D_{f} was estimated from the diffusion coefficient of TAA in water/ethanol mixtures with compositions equivalent to C3 mixture but no silica. These values for TPA and TMA are $3.915\ (\pm 0.046) \times 10^{-10}$ m^2/s and $7.817\ (\pm 0.149) \times 10^{-10}\ \text{m}^2/\text{s}$, respectively. The value of D_{b} has been estimated from DLS measurements ($0.626 \times 10^{-10}\ \text{m}^2/\text{s}$) and is an average value for the nanoparticles in C3 mixtures. Therefore, the bound fraction (f_{b}) of TAA as a function of added salt can be calculated from equation 3-1 and the results are shown in Figure 6-7. As can be seen the TPA bound fraction decreases systematically with addition of more salt and the amount of TPA bound trends as LiCl > NaCl > CsCl. The bound fraction of TPA decreases much more rapidly than the bound fraction of TMA.

Table 6-3. Observed diffusion coefficient (D_{obs}) of TPA and TMA as a function of diffusion time (Δ/s) in silica mixtures.

Samples	0.25TMA/C3		0.25TPA/C3		
Δ (s)	$D_{obs}\times10^{10}$ m^2/s	H_{min}/H_o*	Δ (s)	$D_{obs}\times10^{10}$ m^2/s	H_{min}/H_o*
0.05	0.883 ± 0.048	0.882	0.1	1.198± 0.296	0.542
0.1	0.944 ± 0.033	0.747	0.2	1.216± 0.150	0.228
0.5	1.108 ± 0.013	0.194	0.3	1.205± 0.051	0.283
0.8	0.989 ± 0.018	0.109	0.5	1.202± 0.093	0.176
			0.8	1.206± 0.136	0.171

* H_{min}/H_o is the ratio of peak height of methyl group of TAA obtained at 32 G/cm versus the one obtained at 1G/cm applied in PFG NMR measurements. The accurate diffusion coefficient can be measured within 10-15% decay of peak height at 1 G/cm.

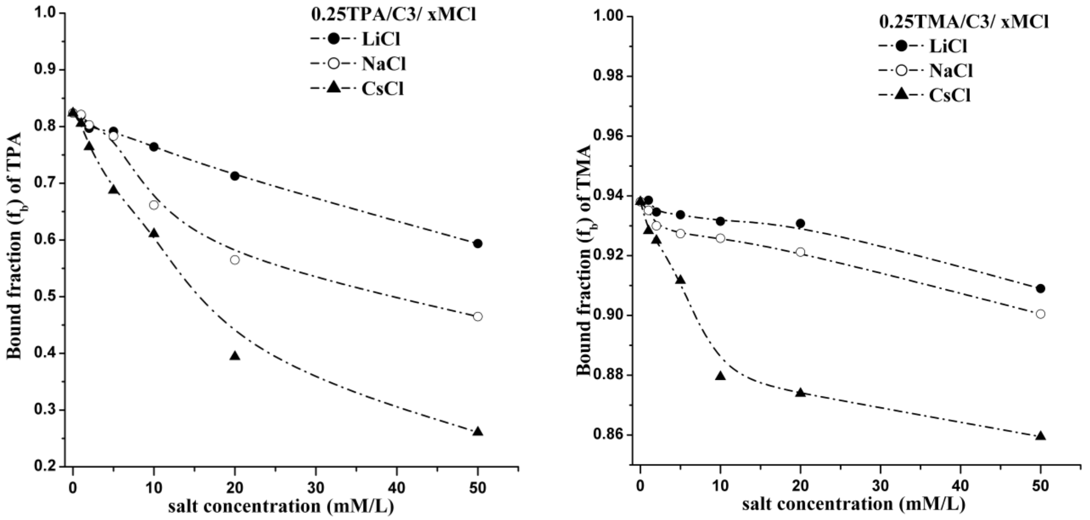

Figure 6-7. Bound fraction (f_b) of (left) TPA and (right) TMA as a function of salt concentration and salt identity in 0.25 TAA/C3 mixtures.

The simplest conclusion from the results in Figure 6-7 is that TPA binding is much more sensitive to the presence of salt than TMA. This is analogous to the behavior observed previously where, upon heating TPA/silica and TMA/silica mixtures, the bound fraction of TPA was found to drop rapidly, whereas the change in the bound fraction of TMA is much less pronounced. That these binding fractions appear to be cation sensitive while the DLS data in Figure 6-3 does not makes us confident that what is being observed in the diffusion NMRis the more effective displacement of the TPA cations from the nanoparticle surface due to salt. While the 0.25 TMA and 0.25 TPA C3 mixtures with 10 mM NaCl possess very similar particle size distributions, i.e., the salt appears to control nanoparticle aggregation, it is clear that the salt is much more effective in displacing the TPA from the nanoparticle surface. Given the results above, it was desired to understand how the mobility of TPA and TMA depended on concentration at a fixed (and low) salt content. Determining the fraction of bound cation as a function of organocation concentration will potentially give insight into the role of alkali-metal cations and soluble salts in the synthesis of microporous and mesoporous materials. [90, 158, 159]

The key finding from the results in Figure 6-6 and Figure 6-7 is that the stability of the precursor nanoparticles is clearly dependent on salt. The PFG-NMR results of salt effect on TAA-silica mixtures have not been reported previously, but are consistent with work by others in the field of colloidal science. [96, 160] Also, it was observed that the TPA cations are much more easily displaced from the nanoparticle surface than TMA. These finding potentially have important implications for zeolite synthesis. For instance, one challenge for the field is that, while silicalite-1 readily forms from such mixtures, it has proven difficult to form other siliceous zeolites using this route. Given that as-made high-silica zeolites appear to be comparable from a thermodynamic point of view, it is unclear why it should not be possible to make others siliceous zeolites using this approach. On the basis of the work by Tsapatsis's lab, oriented aggregation is a likely route for silicalite-1 formation in clear solution. [11, 12, 71] In that mechanism, it is essential for a small number of the precursor nanoparticles to aggregate. Our lab has shown previously that in the presence of many organocations these precursor particles are extremely stable. [77] While large-scale aggregation of the nanoparticles may not be desirable, the current work indicates that the addition of salt is clearly one route for tuning the stability of the particles. Given the discrepancy between theories, which suggests salt should influence growth rates, and experiments, which do not report such an influence, [91] the results in Figure 6-7 indicate future work in this area is warranted.

Another issue of importance is to understand how the bound fraction of organocation changes as a function of concentration at a given electrolyte content. Figure 6-8 shows the diffusion coefficient measured versus the moles of organocation added for TMA silica and TPA-silica mixtures with different salts at 5 mM concentration. As can be seen, the diffusion coefficient of both TPA and TMA increase with increasing cation, which can be described by the two-state model mentioned above. The diffusion coefficient measured increases as a result of the increasing number of free TAA cations. Also for a given TAA content, the diffusion coefficient increases with the ionic radius of the alkali cation, Li < Na< Cs. These results are consistent with the results in Figure 6-6. While the self-diffusion coefficient of TPA plateaus at the highest TPA content, the TMA value does not over the concentration range studied. Given the lack of aggregation at this salt content, the use of the two-state model is unambiguous. Figure 6-9 shows the fraction of TPA and TMA bound in these mixtures. As expected, the amount of bound TPA decreases much more rapidly than the amount of bound TMA as a function of organocation content. Also cesium chloride leads to the most organocation displaced, and lithium chloride leads to the least. These trends are consistent with both the DLS results and the PFG-NMR results where the salt content was varied.

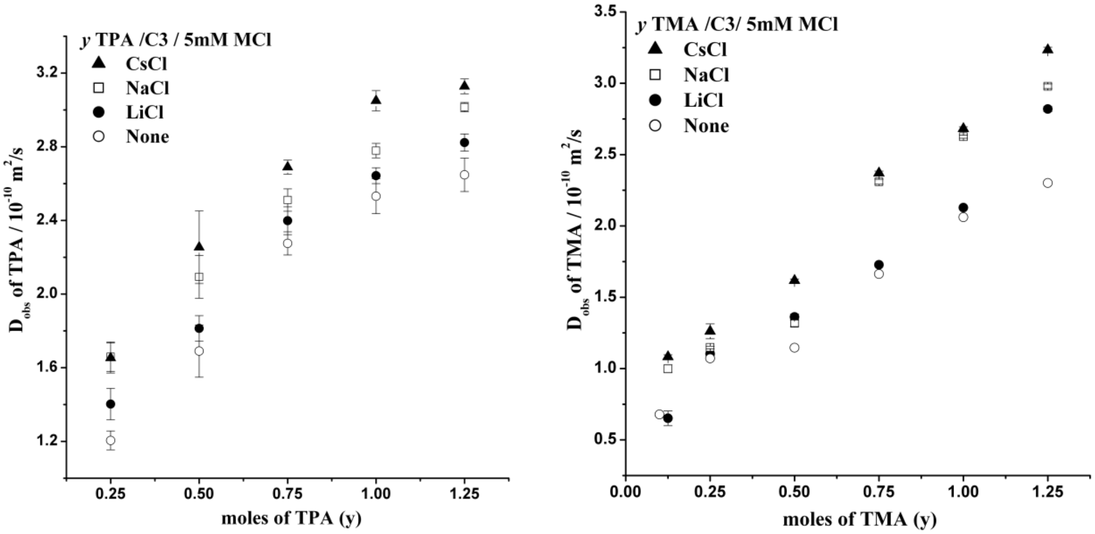

Figure 6-8. Observed diffusion coefficients of (left) TPA and (right) TMA in silica mixtures with 5mM salt as a function of organocation content.

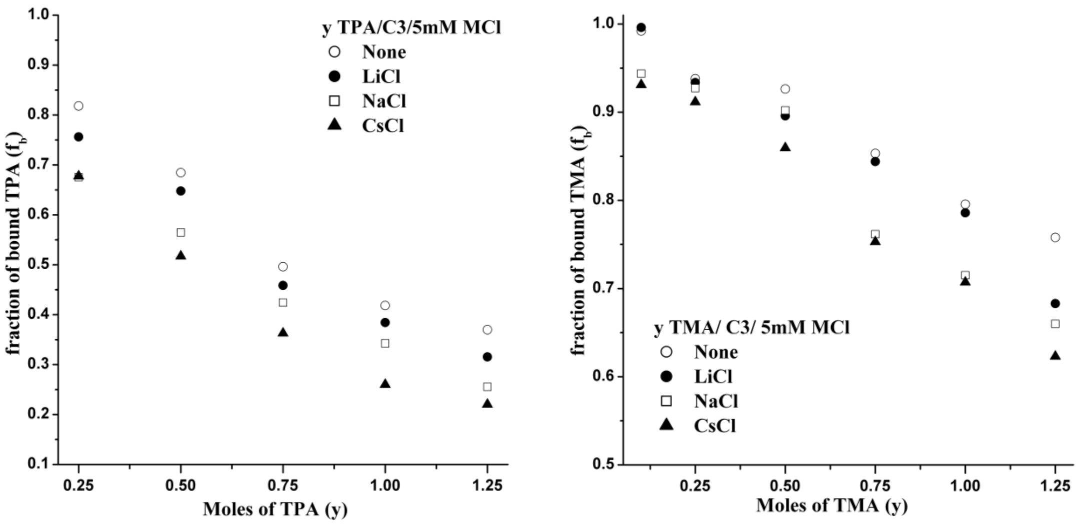

Figure 6-9. Bound fraction of (left) TPA and (right) TMA as a function of organocation content for a series of C3 mixtures with 5 mM salt.

From the variable TAA concentration data shown in Figure 6-8 and Figure 6-9, it is possible to calculate the binding isotherms of TMA and TPA. This enables the determination of the amount of TMA and TPA adsorbed and the adsorption strength onto nanoparticles under the same solution ionic strength. Given that the bound fraction is known, the corresponding binding isotherms were obtained from the equation 3-2 shown in Chapter III.

$$[TAA]_{bound} = f_b[TAA]_{total} \tag{6-2}$$

Figure 6-10 shows the concentration of bound TAA versus total solution concentration (i.e, binding isotherms) derived from the data in Figure 6-8 and Figure 6-9 using equation 3-1 and equation 3-2. This data was then fit to the Langmuir isotherm model as described in subsection 5.3. [161]

$$\Gamma = \frac{\Gamma_{\max} K C_f}{1 + K C_f} \tag{6-1}$$

where Γ and $\Gamma_{\max}$ are the amount of adsorbed TAA and the value at maximum coverage, C_f is the equilibrium concentration of TAA in solution, and K is the adsorption equilibrium constant. The Langmuir model fit results are shown in Table 6-4. R^2 values of all fits are between 0.967 (TMA/C3) and 0.998 (TPA/C3/5mM LiCl), indicating that experiment results fit this model well. To simplify the data analysis, the organocation content in the mixtures is kept less than the value at full surface coverage (9.2mM/kg for TPA and 11.7 mM/kg for TMA).

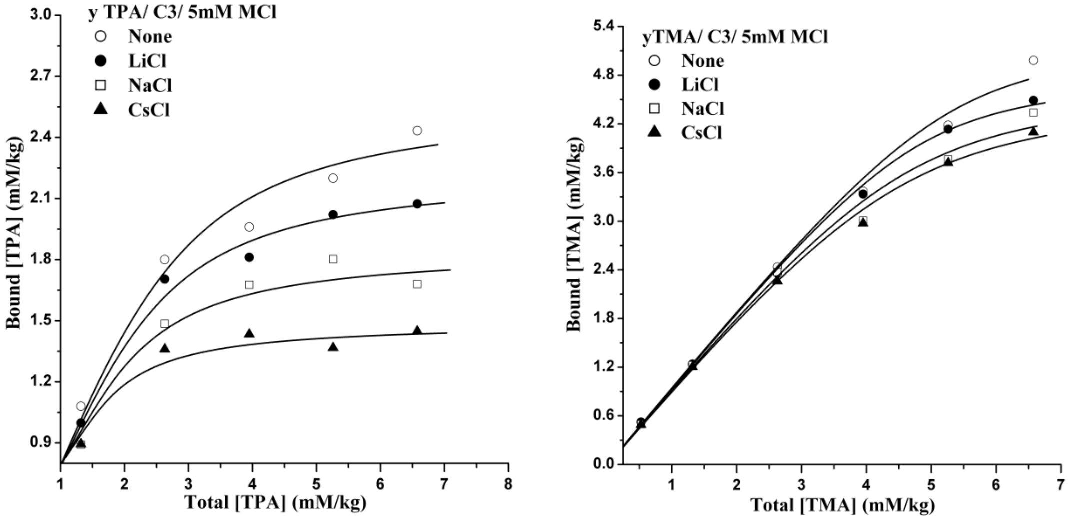

Figure 6-10. Binding isotherms for (left) TPA-silica mixtures and (right) TMA-silica mixtures with 5mM various salts. (The solid curves represent the Langmuir fits.)

Table 6-4. Langmuir isotherm model fit results for TAA binding isotherms in silica mixture with added salt.

	TPA			TMA		
Salt	R^2	σ	P-value	R^2	σ	P-value
None	0.991	0.06925	3.87×10^{-4}	0.967	0.02423	3.94×10^{-4}
LiCl	0.998	0.04105	<0.0001	0.984	0.02359	1.01×10^{-4}
NaCl	0.991	0.10409	3.41×10^{-4}	0.981	0.02930	1.34×10^{-4}
CsCl	0.997	0.08539	<0.0001	0.992	0.02093	<0.0001

Figure 6-11 shows plots comparing the Langmuir constants obtained from fitting binding isotherms of TAA-silica mixtures with various salts. The identity of the three monovalent salts affects TMA and TPA adsorption very differently. Particularly, two key points are observed. First, the maximum adsorption capacity (Γ_{max}) decreases as the ionic size of the added inorganic cations increases but shows a much stronger effect for TPA relative to that of TMA cations. Second, the adsorption constant K for TPA increase as Li < Na < Cs, whereas it displays an opposite trend for TMA. There are several possible interpretations. Given the two-fold decrease in the maximum amount adsorbed (Γ_{max}) for TPA-silica mixtures, the TPA remaining on the surface is likely more strongly bound, resulting in an increase in the K value. Another view of this is that the surface binding sites have a distribution of energies, and the TPA displaced leaves low energy sites preferentially. Another possibility is that the solubility of the TPA associated with the nanoparticles decreases as water activity changes due to the salt, which drives stronger adsorption. As the surface charge of the silica particles is increasingly screened with increasing ionic strength, the particle surface may become more hydrophobic, and the electrostatic forces may not be the dominant factor. The maximum amount of TMA adsorbed decreases slightly and is much larger than TPA. TMA cations have a decreasing potential for strong adsorption because of their stronger partitioning into the aqueous phase as the result of their larger charge to size ratio. Taken together, the results above show a quantitative comparison of nanoparticle stability in the presence of various monovalent salts and how the adsorption of organocations varies at the onset of particle aggregation. The results in Figure 6-8 to Figure 6-11 indicate that TPA is more easily displaced from the surface of precursor nanoparticles than TMA. Moreover, this is clearly dependent on the salt used, consistent with Hoffmeister series effects.

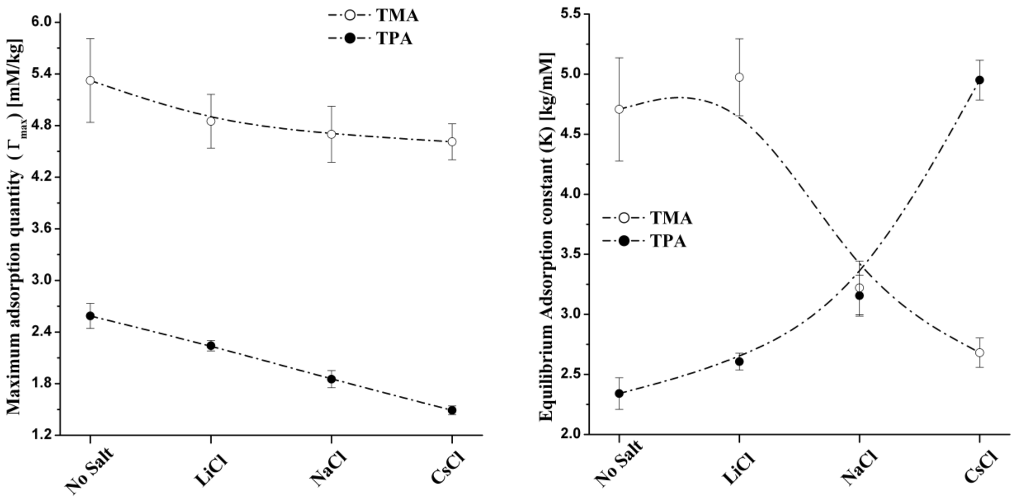

Figure 6-11. Plots comparing (left) K and (right) Γ_{max} of TAA-silica mixture with 5mM various salts (TAA=TMA, TPA).

6.4 Conclusions

The silica nanoparticle precursors present in TAA silica mixtures can be rapidly driven to aggregate in the presence of simple electrolytes. Cesium chloride destabilizes the particles at much lower salt content than sodium or lithium chloride, consistent with Hoffmeister series. The PFG-NMR results of salt effect on TAA-silica mixtures have not been reported previously, but are consistent with work by others in the field of colloidal science. [160, 161] It is also observed that TPA binding to the nanoparticles is sensitive to the presence of small (<10mM) amounts of salt, where asTMA binding is on the whole much less sensitive. The current work highlights the complexities of these systems and potentially points to a route to modifying clear solution preps with the addition of monovalent salts, and possibly suggesting synthetic routes for accessing other siliceous zeolites via clear solution syntheses.

CHAPTER VII

CONCLUSION AND FUTURE WORK

7.1 Conclusions of Current Studies

Chapters III to V reported quantitative analyses of TAA-silica precursor nanoparticle interactions prior to and during silicalite-1 synthesis. During aging at room temperature, such organic-inorganic interactions occur via binding of TAA cations onto the negatively charged surface of silica particles and the corresponding binding isotherm curves can be calculated. Furthermore, binding energetics of TPA and TMA with respect to different silica nanoparticle content was obtained by the Langmuir adsorption model fitting. TMA, with the highest surface charge density (C/N) the organocations, has a stronger adsorption strength and larger adsorption amount than TPA, which indicates electrostatic forces are likely the dominate forces controlling binding equilibrium. Chapter IV extended the NMR studies to monitor the mobility change of TPA in synthesis mixtures that have been heated and the results indicate a fraction of TPA adsorbed at room temperature dissociate from growing silica precursor nanoparticles, from which TPA desorption kinetic profiles were obtained. Furthermore, various kinetic models were introduced to describe the TPA desorption, from which rate constants at different heating temperatures were calculated and the resulting activation energy is at the lower end of the values obtained from scattering measurements. Given the limit of NMR on detecting TPA assumed to be gradually occluded in the growing silica precursors, these kinetic studies were preformed during the early stages of silicalite-1 nucleation.

Given that the organic SDA appears to control some kinetics of zeolite formation, addition of TMA as "competitors" to TPA adsorption onto silica precursor at RT and ultimately in directing silicalite-1 upon heating was discussed in Chapter V. The results showed the presence of TMA promoted TPA desorption and hindered silica particle growth via strong association between TMA and the particles. Increasing TMA amount above a certain point results in suppression of silicalite-1 formation in mixed orgnocation syntheses. Chapter IV determined how addition of monovalent salts impacts silica precursor particle stability and TAA-silica interactions. The extent of salt-induced aggregation increases with the ionic size of added alkali-metal cations, consistent with the Hoffmeister series. PFG NMR analysis indicates TPA adsorption is much more sensitive to the presence of salt and the resulting particle aggregation than TMA. Also noteworthy is that the TPA adsorption strength increases with increasing ionic size of added salt whereas this property of TMA shows an opposite trend. (see Figure 6-11 (right)) This finding suggests one route for tuning the organic SDA-precursor particle interactions and thus possible affects some steps in the synthesis mechanism. Figure 7-1 shows the XRD pattern of solid products obtained from 0.5TPA/1.5TMA/C3 mixtures added with 5 mM NaCl and in absence of salt this mixtures cannot produce silicalite-1.

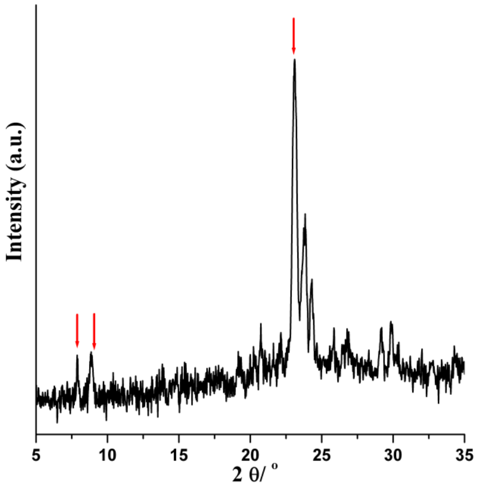

Figure 7-1. XRD pattern of solids prepared from 0.5 TPA/1.5 TMA/C3 mixtures with 5mM NaCl.

7.2 Future Work

Developing a comprehensive understanding of zeolite synthesis mechanism relies on detailed information on structure and composition of primary units, characterization of primary unit-SDA interactions, and elucidation of how these properties are affected by synthesis conditions. This thesis studied silicalite-1 formation from clear solutions with silica nanoparticles as primary units and tetraalkalyammonium (TAA) as SDA. Thermodynamic and kinetic studies on silica particle-TAA interactions were performed using combined scattering and NMR techniques. Also the impact of varied heating temperature, TPA contents and solution ionic strength on this inorganic-organic interaction were examed. Since pure-silica zeolites comprise a small fraction of the entire zeolite framework class, studies on silicalite-1 formation are a starting point for conducting mechanistic investigations of porous materials syntheses. The following subsections summarize further experiments for expanding the scope of this thesis.

7.2.1 PFG NMR Analysis of Inorganic-Organic Associations

Indentifying organic-inorganic associations in porous silicate growth provides implications for developing novel materials as well as fundamental aspects of self-assembly. [124, 162, 163] PFG NMR is a powerful technique to studying such association via changes in the molecule self-diffusion value.[164] In Chapter II and Chapter III, we showed organic SDAs bind to the negatively charged silica particles to form a complex and the binding involved fast exchange on the time-scale of PFG NMR measurements. Thus the measured diffusion coefficient of SDA is a weighted averaged of diffusion of free and bound SDA, and the weighting factors being the relative number of the individual states. This methodology can be generally applied to numerous material synthesis assisted by organic molecules. The formation of uniform sized silica nanoparticles catalyzed by amino acid is a typical example. Yoki et al introduced a modified Stöiber method for synthesizing silica spheres with tunable size via TEOS hydrolysis using lysine instead of ammonia. [165, 166] An important observation is that the lysine-nanoparticle composites can be redispersed, indicating a possibly critical role of lysine in the particle assembly and arrangements Figure 7-2 shows the SAXS data of lysine-silica mixtures hydrolyzed at 70 ^{o}C for 24h. The results indicate that no large (> 50 nm) particles were observed at any appreciable level as the intensity versus scattering vector plateaus at approximately 0.1–0.12 nm^{-1}. The PDDF (inset) indicates the particle radius is approximately 1.3 nm, and no large aggregates are observed.

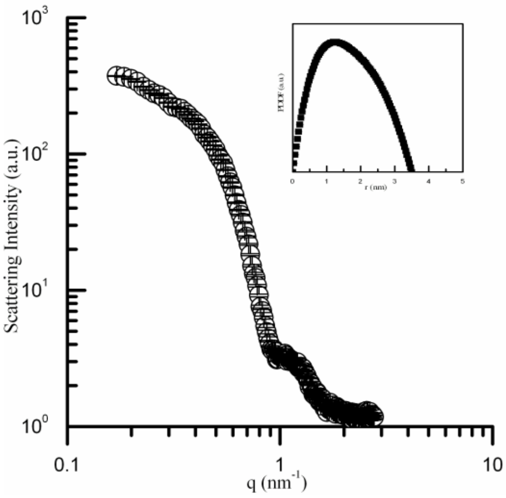

Figure 7-2. SAXS data for lysine-silica mixtures hydrolyzed for 24h at 70°C. (Inset) Corresponding pair distance distribution function.

The NMR analysis of the dynamics of lysine involved in nanospheres formation would provide insights into this process. Figure 7-4 shows the ^{1}H NMR spectra of lysine-TEOS-water mixtures hydrolyzed at different temperatures for 48 h. The resonances at 3.00 ppm and 2.90 ppm are assigned to the 2-H proton of lysine and the a-H proton of DSS as internal standard, respectively (See Figure 7-3).

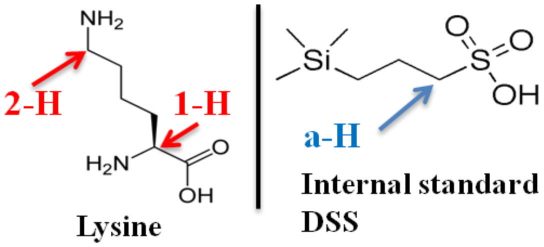

Figure 7-3. Molecular structures of lysine (left) and DSS (right).

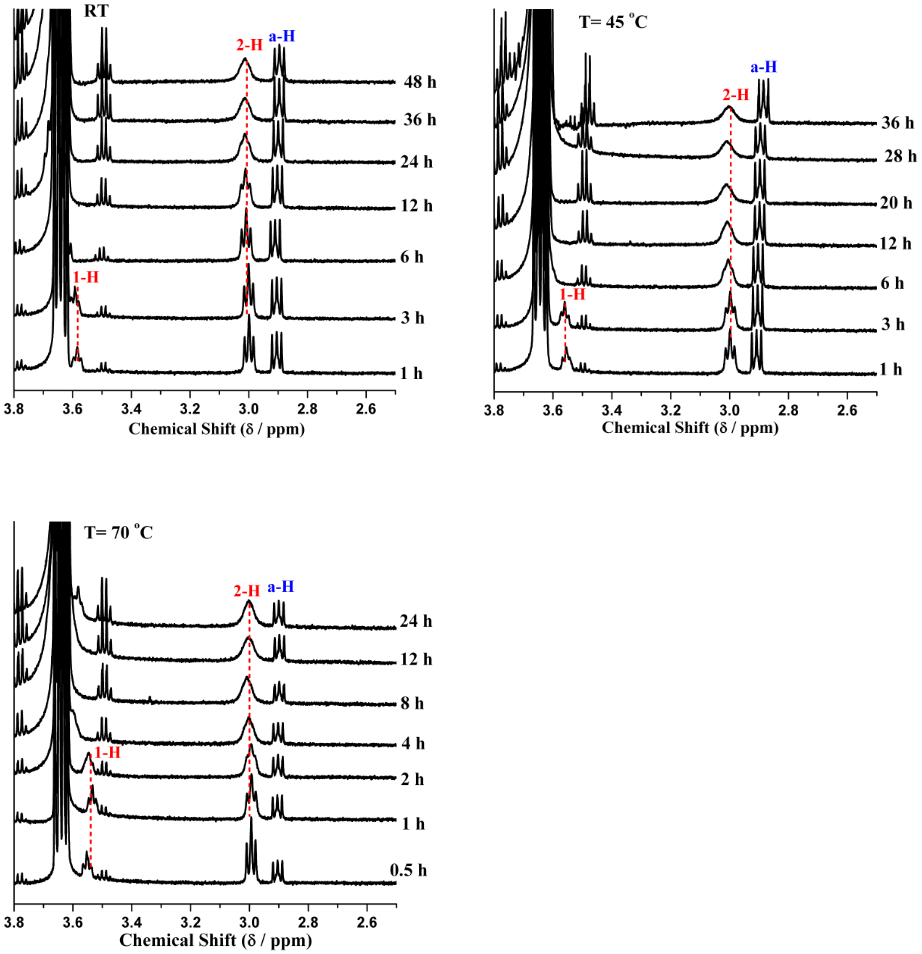

Figure 7-4. ^{1}H NMR spectra of lysine-TEOS-water mixtures hydrolyzed at (clockwise) room temperature, 45 °C and 70 °C. (For clarity, spectral region corresponding to the 2-H resonance of lysine and a-H resonance of DSS are shown, and the y-axis is on the same scale.)

As can be seen in Figure 7-4, no appreciable changes in the chemical shift values of lysine and DSS were observed except that for the 1-H of lysine, originally at 3.55 ppm which merged progressively into the increasing ethanol signal due to TEOS hydrolysis. More important, the line width of the DSS resonance at 2.90 ppm remains unchanged whereas the 1-H of lysine gradually broadens as hydrolysis proceeds. Also increasing the hydrolysis temperature leads to the observed broadening of the lysine signal occurring more quickly. A simple interpretation is that interactions between lysine and the formed nanoparticles lead to line broadening. Figure 7-5 (left) shows the observed diffusion coefficient (D_{obs}) of lysine in same mixtures shown in Figure 7-4, as a function of hydrolysis time. As can be seen the diffusion coefficient value decreases with hydrolysis time and in all cases plateaus to a nearly constant value after 12-36h. A decrease in translational mobility of lysine suggests binding of lysine with the nanoparticles formed as TEOS hydrolyzes. One mode of interaction could be electrostatic attraction between the protonated amino group of lysine and anionic nanoparticle surface (pH~ 9.0). Thus we describe the lysine-silica interactions using the two-site model shown in Chapter II, wherein the lysine can be either 'free' in solution or 'adsorbed' to the formed silica particles. Figure 7-5(right) shows the kinetic profiles of lysine adsorption at different hydrolysis time. As can be seen in this figure, the amount of lysine adsorbed appears to plateau at nearly the same value, suggesting that the particles formed are insensitive to temperature. However, the increase in lysine adsorption is very dependent on increasing hydrolysis temperature, indicating temperature dependent TEOS hydrolysis (and thus nanoparticle formation).

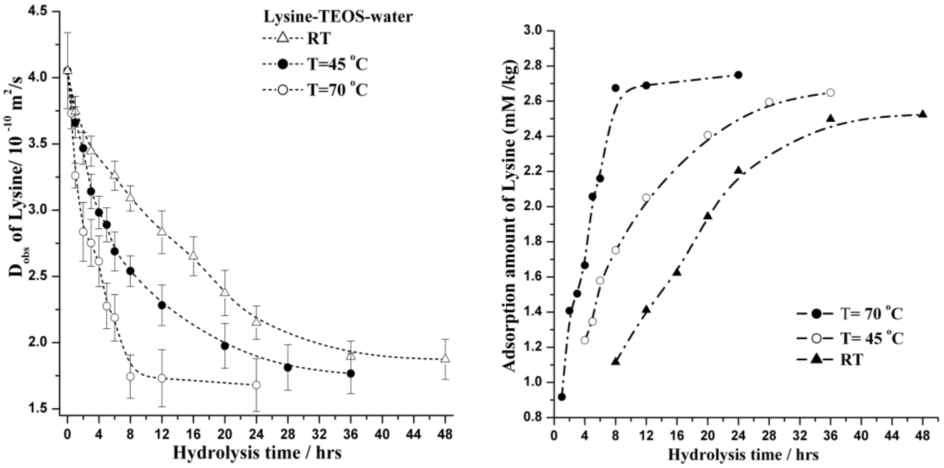

Figure 7-5. (Left) Observed diffusion coefficient (D_{obs}) of lysine as a function of hydrolysis time for lysine-TEOS-water mixture hydrolyzed at various temperatures. (Right) corresponding lysine adsorption kinetics at different temperatures.

The pseudo-second-order kinetic model (equation 4-3b) can be used to describe the lysine adsorption kinetics in Figure 7-5 and fit the adsorption rate at various temperatures. The linear regression plots for this kinetic model fit are shown in Figure 7-6 (left) and resulting R^2 values range from 0.98 to 0.99 for the temperature studied, indicating lysine adsorption data were well described by this model. On the basis of the adsorption rate constants (k_{ad}) at different temperatures an Arrhenius plot can be developed and shown in Figure 7-6 (right). The activation energy (E_A) for lysine adsorption during the reaction is found to be 38.3 ± 3.5 kJ/mol. This value is relatively low, indicating weak interactions between the silica spheres and lysine. Thus the above work shows that kinetics studies of particle – stabilizer (here lysine) can be performed non-invasively using PFG NMR, and give insights into understanding in the case of organic molecule stabilization of silica nanoparticles.

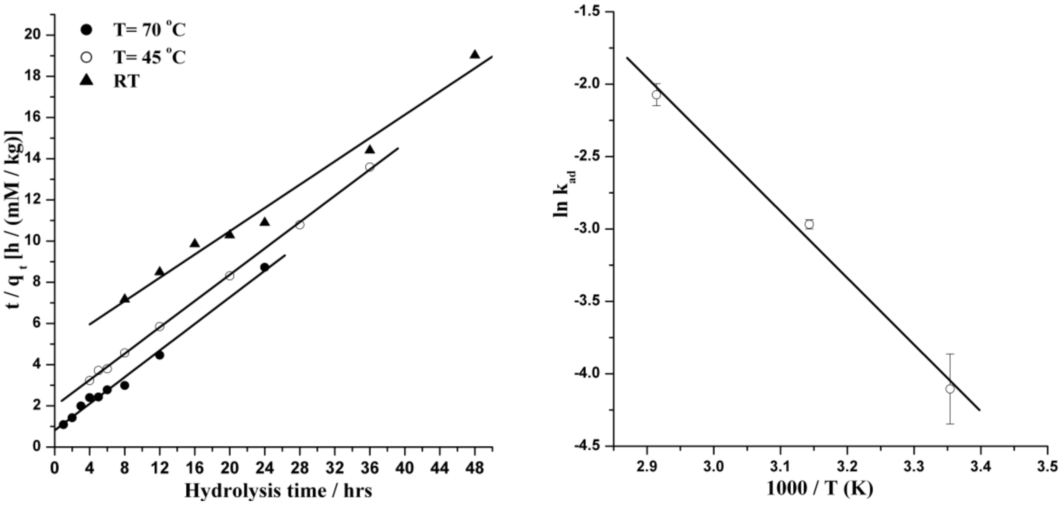

Figure 7-6. (Left) Pseudo-second-order kinetic plots of lysine adsorption at various temperatures shown in Figure 7-5. (Right) Arrhenius plot of the lysine adsorption kinetics ($R^2 = 0.991$). (The solid line represents the fit to the linear regression.)

7.2.2 Study of Heteroatom Substituted Zeolites Synthesis

Silicalite-1 from clear solutions has merged as an ideal model for mechanistic studies. However, it is desired to make zeolites with elements beside silicon in the framework. Control of zeolite frameworks for creating catalytic sites in zeolite can be performed either through varying organic SDA or through substituting silicon with different atoms (Al, B, Ge, Ga, etc.) in the frameworks. Also various zeolite frameworks can be obtained given a same organic SDA. [167-174] Despite an empirical understanding of synthesis of heteroatom substituted zeolites, this is a unsolved problem. To approach this, three principal aspects regarding to the mechanistic study should be considered: 1. how these heteroatoms partition into silica precursors and affect their structures, 2. how the properties of organic SDA-silica precursor interactions change in the presence of heteroatoms, and 3. the transformation of organic-inorganic complex containing SDA, silicon and heteroatoms into zeolite nuclei.

Quantitative analysis of organic SDA during zeolite synthesis using PFG NMR could provide thermodynamic and kinetics of organic-inorganic interactions with regards to the second aspect. Figure 7-7 shows the PFG NMR measurements of TPA in synthesis mixtures with varying Si/Ge or Si/B molar ratio. Figure 7-8 shows the XRD pattern for B-silicalite-1obtained from the mixtures shown in Figure 7-7, and mixtures with Si/B ratio below 25 cannot produce zeolites. On basis of diffusion coefficient change of TPA during MFI zeolite synthesis, one can determine the faction of adsorbed TPA as function of synthesis time, and relate the kinetic profiles in growth energies.

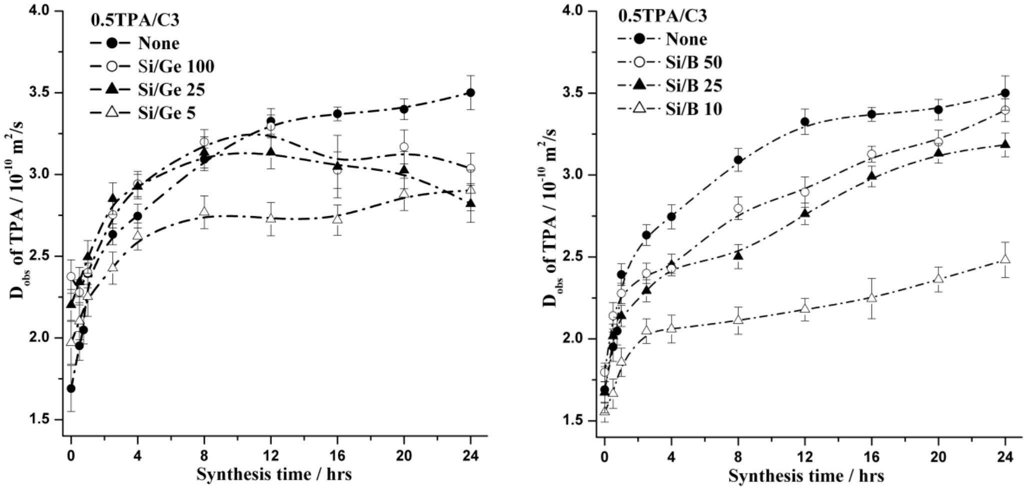

Figure 7-7. Observed diffusion coefficient (D_{obs}) of TPA in 0.5 TPA/C3 mixture with varying (left) Si/Ge and (right) Si/B molar ratios. (Ge was added as $Ge(OEt)_4$, and B was added as $B(OEt)_3$.)

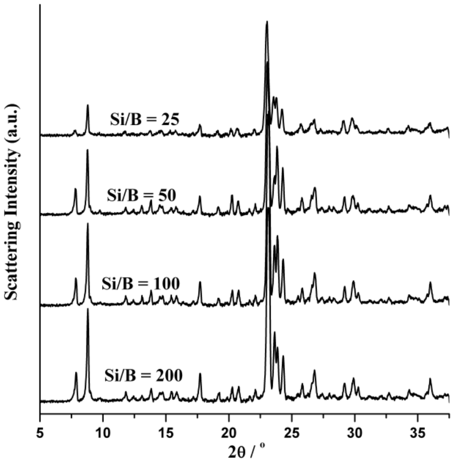

Figure 7-8. XRD pattern of B-silicalite-1solids obtained from 0.5 TPA/C3 synthesis mixtures with Si/B molar ratio ranging from 25 to 200.

Given the complex chemistries involved in presence of heteroatoms, instruments for measuring aqueous solution and solid products should be introduced to analyze the precursors, intermediate species and final products present in synthesis processes. For instance, the structures of inorganic complex with heteroatoms can be indentified using electrospray ionization mass spectrometry (ESI-MS) and MS techniques. [175] Also small-angle scattering (SAXS and SANS) is one useful tool for quantifying the compositional properties of precursors. In addition, ^{27}Al, ^{11}B and ^{29}Si solution state NMR are appropriate methods to characterize the dissolved species including oligomers in precursor solutions yet the careful interpretation must be made. [6, 176] Furthermore, if the precursor solids could be separated at specific stages of zeolite synthesis, solid-state NMR and XPS, XRF analyses of their structures and compositions would offer insightful information for elucidating evolution of these precursors.

7.2.3 Effect of Synthesis Conditions on Zeolite Formation

Since zeolite synthesis parameters can have a profound effect on the resulting zeolite growth, developing a universal mechanism to describe zeolite nucleation and crystallization is not difficult, so is the design of zeolite synthesis routes. Despite most of the advances in making novel zeolite come from trial-and-error discoveries, mechanistic studies on self-assembly, inorganic-organic complex involved in zeolite formation provides useful knowledge for rational design. The NMR results from Chapter V shows that the fraction of organocations (TAA) bound to silica precursors can be manipulated through control of added monovalent salts, leading to changes of the organic-inorganic interaction strengths. Since one would expect increasing ionic strength via addition of salts would decrease Debye length of the colloidal precursors, organic SDA's binding strength and amount would be affected. Thus, on the basis of Chapter V, tuning the binding energy of organic SDA-inorganic precursor could be an approach to open kinetic pathways to synthesis zeolites which is currently not feasible from solutions.

REFERENCES

1. Corma, A. *J. Catal.* **2003,** *216*, 298-312.

2. Volksen, W.; Miller, R. D.; Dubois, G. *Chem. Rev.* **2009,** *110*, 56-110.

3. Davis, M. E.; Lobo, R. F. *Chem. Mater.* **1992,** *4*, 756-768.

4. Lobo, R. F.; Zones, S. I.; Davis, M. E. *J. Incl. Phenom. Macro. Chem.* **1995,** *21*, 47-78.

5. Davis, M. E. *Nature* **2002,** *417*, 813-821.

6. Bonneviot, L. In *Zeolites: a refined tool for designing catalytic sites*, Proceedings of 2nd International Zeolite Symposium Québec, Canada, 1995; Elsevier Science Ltd:

7. Fedeyko, J. M.; Rimer, J. D.; Lobo, R. F.; Vlachos, D. G. *J. Phys. Chem. B* **2004,** *108*, 12271-12275.

8. de Moor, P. P. E. A.; Beelen, T. P. M.; Komanschek, B. U.; Diat, O.; van Santen, R. A. *J. Phys. Chem. B* **1997,** *101*, 11077-11086.

9. de Moor, P. P. E. A.; Beelen, T. P. M.; van Santen, R. A. *J. Phys. Chem. B* **1999,** *103*, 1639-1650.

10. de Moor, P. E. A.; Beelen, T. P. M.; Santen, R. A. *Chem. Mater* **1999,** *11*, 36.

11. Davis, T. M.; Drews, T. O.; Ramanan, H.; He, C.; Dong, J.; Schnablegger, H.; Katsoulakis, M. A.; Kokkoli, E.; McCormick, A. V.; Penn, R. L. *Nature Mater.* **2006,** *5*, 400-408.

12. Kumar, S.; Wang, Z.; Penn, R. L.; Tsapatsis, M. *J. Am. Chem. Soc.* **2008,** *130*, 17284-17286.

13. Kinrade, S. D.; Knight, C. T. G.; Pole, D. L.; Syvitski, R. T. *Inorg. Chem.* **1998,** *37*, 4272-4277.

14. Burkett, S. L.; Davis, M. E. *Chem. Mater.* **1995,** *7*, 920-928.

15. Burkett, S. L.; Davis, M. E. *Chem. Mater.* **1995,** *7*, 1453-1463.

16. McCusker, L. B.; Baerlocher, C. *Stud. Surf. Sci. Catal.* **2007,** *168*, 13-37.

17. Wilson, S. T.; Lok, B. M.; Messina, C. A.; Cannan, T. R.; Flanigen, E. M. *J. Am. Chem. Soc.* **1982,** *104*, 1146-1147.

18. Lok, B. M.; Messina, C. A.; Patton, R. L.; Gajek, R. T.; Cannan, T. R.; Flanigen, E. M. U.S. Pat. 4440871. 1984.

19. van Bekkum, H.; Flanigen, E. M.; Jansen, J. C., *Introduction to zeolite science and practice*. Elsevier Science: 1991.

20. Newsam, J. M., *Solid State Chemistry: Compounds*. Oxford University Press: Oxford: 1992.

21. Helmkamp, M. M.; Davis, M. E. *Annu. Rev. Mater. Sci.* **1995,** *25*, 161-192.

22. R.J. Argauer, G. R. L. U.S. Patent No. 3702 886 1972.

23. Olson, D. H.; Kokotailo, G. T.; Lawton, S. L.; Meier, W. M. *J. Chem. Phys.* **1981,** *85*, 2238-2243.

24. Cundy, C. S.; Cox, P. A. *Chem. Rev.* **2003,** *103*, 663-702.

25. Auerbach, S. M.; Carrado, K. A.; Dutta, P. K., *Handbook of zeolite science and technology*. CRC: 2003.

26. Csicsery, S. M. *Zeolites* **1984,** *4*, 202-213.

27. Houssin, C. J. M. Y. Nanoparticles in zeolite synthesis. Eindhoven University of Technology, 2003.

28. Venuto, P. B.; Habib Jr, E. T., *Fluid catalytic cracking with zeolite catalysts*. Marcel Dekker, Inc.: New York, 1979.

29. Cejka, J., *Introduction to zeolite science and Practice*. Elsevier Science: New York, 2007.

30. Iler, R. K.; Knovel, *The chemistry of silica: solubility, polymerization, colloid and surface properties, and biochemistry*. Wiley New York: 1979.

31. Holleman, A. F., *Inorganic chemistry*. Academic Press: Berlin, 2001.

32. Cox, P. A.; Casci, J. L.; Stevens, A. P. *Faraday. Discuss.* **1997,** *106*, 473-487.

33. Breck, D. W.; Eversole, W. G.; Milton, R. M. *J. Am. Chem. Soc.* **1956,** *78*, 2338-2339.

34. Burton, A. W.; Zones, S. I.; Elomari, S. *Curr. Opin. Colloid. In.* **2005,** *10*, 211-219.

35. Burton, A.; Elomari, S.; Medrud, R. C.; Chan, I. Y.; Chen, C. Y.; Lucy, M.; Vittoratos, E. S. *J. Am. Chem. Soc.* **2003,** *125*, 1633-1642.

36. Lawton, S. L.; Rohrbaugh, W. J. *Science* **1990,** *247*, 1319.

37. Kokotailo, G. T.; Lawton, S. L.; Olson, D. H. *Nature* **1978,** *272*, 437-438.

38. Chao, K. J.; Lin, J. C.; Wang, Y.; Lee, G. H. *Zeolites* **1986,** *6*, 35-38.

39. Aiello, R.; Crea, F.; Nastro, A.; Subotic, B.; Testa, F. *Zeolites* **1991,** *11*, 767-775.

40. Testa, F.; Szostak, R.; Chiappetta, R.; Aiello, R.; Fonseca, A.; Nagy, J. B. *Zeolites* **1997,** *18*, 106-114.

41. Shen, V.; Bell, A. T. *Microporous Mater.* **1996,** *7*, 187-199.

42. Gies, H.; Marker, B. *Zeolites* **1992,** *12*, 42-49.

43. Sierra, L.; Patarin, J.; Deroche, C.; Gies, H.; Guth, J. L. *Stud. Surf. Sci. Catal.* **1994,** *84*, 2237-2244.

44. Kubota, Y.; Helmkamp, M. M.; Zones, S. I.; Davis, M. E. *Microporous Mater.* **1996,** *6*, 213-229.

45. Wagner, P.; Nakagawa, Y.; Lee, G. S.; Davis, M. E.; Elomari, S.; Medrud, R. C.; Zones, S. I. *J. Am. Chem. Soc.* **2000,** *122*, 263-273.

46. Cheng, C. H.; Shantz, D. F. *J. Phys. Chem. B* **2005,** *109*, 13912-13920.

47. Goretsky, A. V.; Beck, L. W.; Zones, S. I.; Davis, M. E. *Microporous Mesoporous Mater.* **1999,** *28*, 387-393.

48. Breck, D. W. *J. Chem. Educ.* **1964,** *41*, 678-689.

49. Kerr, G. T. *J. Chem. Phys.* **1966,** *70*, 1047-1050.

50. Breck, D. W., *Zeolile molecular sieves structure, chemistry and use.* New York: J. Wiley: 1974.

51. Tezak, B. *Faraday. Soc. Discuss.* **1966,** *42*, 175-186.

52. Flanigen, E. M. *Molecular Sieves; Meier, W.M., Uytterhoeven, J.B., Eds.; American Chemical Society: Washington, Dc* **1973,** 119-139.

53. Coker, E. N.; Jansen, J. C.; Martens, J. A.; Jacobs, P. A.; DiRenzo, F.; Fajula, F.; Sacco Jr, A. *Microporous Mesoporous Mater.* **1998,** *23*, 119-136.

54. Culfaz, A.; Sand, L. B. *Adv. Chem. Ser* **1973,** *121*, l40-151.

55. Nikolakis, V. *Curr. Opin. Colloid. In.* **2005,** *10*, 203-210.

56. Nikolakis, V.; Vlacho, D. G.; Tsapatsis, M. *Microporous Mesoporous Mater.* **1998,** *21*, 337-346.

57. Watson, J. N.; Iton, L. E.; Keir, R. I.; Thomas, J. C.; Dowling, T. L.; White, J. W. *J. Phys. Chem. B* **1997,** *101*, 10094-10104.

58. Flanigen, E. M.; Bennett, J. M.; Grose, R. W.; Cohen, J. P.; Patton, R. L.; Kirchner, R. M. *Nature* **1978,** *271*, 512-516.

59. Dokter, W. H.; Beelen, T. P. M.; Van Garderen, H. F.; Van Santen, R. A.; Bras, W.; Derbyshire, G. E.; Mant, G. R. *J. Appl. Crystallogr.* **1994,** *27*, 901-906.

60. Dokter, W. H.; Beelen, T. P. M.; Van Garderen, H. F.; Rummens, C. P. J.; Van Santen, R. A.; Ramsay, J. D. F. *Colloid. Surface. A* **1994,** *85*, 89-95.

61. Chang, C. D.; Bell, A. T. *Catal. Lett.* **1991,** *8*, 305-316.

62. Nikolakis, V.; Kokkoli, E.; Tirrell, M.; Tsapatsis, M.; Vlachos, D. G. *Chem. Mater.* **2000,** *12*, 845-853.

63. Houssin, C. J. Y.; Kirschhock, C. E. A.; Magusin, P. C. M. M.; Mojet, B. L.; Grobet, P. J.; Jacobs, P. A.; Martens, J. A.; van Santen, R. A. *Phys. Chem. Chem. Phys.* **2003,** *5*, 3518-3524.

64. de Moor, P. P. E. A.; Beelen, T. P. M.; van Santen, R. A.; Beck, L. W.; Davis, M. E. *J. Phys. Chem. B* **2000,** *104*, 7600-7611.

65. Yang, S.; Navrotsky, A.; Wesolowski, D. J.; Pople, J. A. *Chem. Mater.* **2004,** *16*, 210-219.

66. Mintova, S.; Olson, N. H.; Senker, J.; Bein, T. *Angew. Chem. Int. Edit.* **2002,** *114*, 2670-2673.

67. Burkett, S. L.; Davis, M. E. *J. Chem. Phys.* **1994,** *98*, 4647-4653.

68. Kirschhock, C. E.; Buschmann, V.; Kremer, S.; Ravishankar, R.; Houssin, C. J.; Mojet, B. L.; van Santen, R. A.; Grobet, P. J.; Jacobs, P. A.; Martens, J. A. *Angew. Chem. Int. Edit.* **2001,** *40*, 2637-2640.

69. Kirschhock, C. E. A.; Ravishankar, R.; Verspeurt, F.; Grobet, P. J.; Jacobs, P. A.; Martens, J. A. *J. Phys. Chem. B* **1999,** *103*, 4965-4971.

70. Houssin, C. J. Y.; Mojet, B. L.; Kirschhock, C. E. A.; Buschmann, V.; Jacobs, P. A.; Martens, J. A.; van Santen, R. A. In *Small angle X-ray scattering on TPA-Silicalite-1 precursors in clear solutions: influence of silica source and cations* Proceedings of the 13th International Zeolite Conference, Montpellier, France, 2001;

71. Kumar, S.; Davis, T. M.; Ramanan, H.; Penn, R. L.; Tsapatsis, M. *J. Phys. Chem. B* **2007,** *111*, 3398-3403.

72. Kragten, D. D.; Fedeyko, J. M.; Sawant, K. R.; Rimer, J. D.; Vlachos, D. G.; Lobo, R. F.; Tsapatsis, M. *J. Phys. Chem. B* **2003,** *107*, 10006-10016.

73. Fedeyko, J. M.; Vlachos, D. G.; Lobo, R. F. *Langmuir* **2005,** *21*, 5197-5206.

74. Rimer, J. D.; Lobo, R. F.; Vlachos, D. G. *Langmuir* **2005,** *21*, 8960-8971.

75. Rimer, J. D.; Fedeyko, J. M.; Vlachos, D. G.; Lobo, R. F. *Chem. Eur. J.* **2006,** *12*, 2926-2934.

76. Rimer, J. D.; Trofymluk, O.; Navrotsky, A.; Lobo, R. F.; Vlachos, D. G. *Chem. Mater.* **2007,** *19*, 4189-4197.

77. Cheng, C. H.; Shantz, D. F. *J. Phys. Chem. B* **2005,** *109*, 7266-7274.

78. Rimer, J. D.; Vlachos, D. G.; Lobo, R. F. *J. Phys. Chem. B* **2005,** *109*, 12762-12771.

79. Drews, T. O.; Tsapatsis, M. *Curr. Opin. Colloid. In.* **2005,** *10*, 233-238.

80. Drews, T. O.; Tsapatsis, M. *Microporous Mesoporous Mater.* **2007,** *101*, 97-107.

81. Jorge, M.; Auerbach, S. M.; Monson, P. A. *J. Am. Chem. Soc.* **2005,** *127*, 14388-14400.

82. Corma, A.; Davis, M. E. *Chem. Phys. Chem.* **2004,** *5*, 304-313.

83. Persson, A. E.; Schoeman, B. J.; Sterte, J.; Otterstedt, J. E. *Zeolites* **1994,** *14*, 557-567.

84. Schoeman, B. J.; Regev, O. *Zeolites* **1996,** *17*, 447-456.

85. Schoeman, B. J. *Zeolites* **1997,** *18*, 97-105.

86. Ravishankar, R.; Kirschhock, C.; Schoeman, B. J.; Vanoppen, P.; Grobet, P. J.; Storck, S.; Maier, W. F.; Johan. A. Martens; De Schryver, F. C.; Jacobs, P. A. *J. Phys. Chem. B* **1998,** *102*, 2633-2639.

87. de Moor, P. P. E. A.; Beelen, T. P. M.; Komanschek, B. U.; Beck, L. W.; Wagner, P.; Davis, M. E.; van Santen, R. A. *Chem. Eur. J.* **1999,** *5*, 2083-2088.

88. Nikolakis, V.; Tsapatsis, M.; Vlachos, D. G. *Langmuir* **2003,** *19*, 4619-4626.

89. Rimer, J. D. Self-assembly of silica nanoparticles and their role in the mechanism of silicalite-1 crystallization. University of Delaware, 2007.

90. Cundy, C. S.; Lowe, B. M.; Sinclair, D. M. *Faraday. Discuss.* **1993,** *95*, 235-252.

91. Twomey, T. A. M.; Mackay, M.; Kuipers, H.; Thompson, R. W. *Zeolites* **1994,** *14*, 162-168.

92. Li, Q.; Creaser, D.; Sterte, J. *Microporous Mesoporous Mater.* **1999,** *31*, 141-150.

93. Sano, T.; Sugawara, S.; Kawakami, Y. *Stud. Surf. Sci. Catal.* **1994,** *84*, 187-194.

94. Feoktistova, N. N.; Zhdanov, S. P.; Lutz, W.; Bullow, M. *Zeolites* **1989,** *9*, 136-139.

95. Navrotsky, A.; Petrovic, I.; Hu, Y.; Chen, C. Y.; Davis, M. E. *Microporous Mater.* **1995,** *4*, 95-98.

96. Petrovic, I.; Navrotsky, A.; Davis, M. E.; Zones, S. I. *Chem. Mater.* **1993,** *5*, 1805-1813.

97. Piccione, P. M.; Laberty, C.; Yang, S.; Camblor, M. A.; Navrotsky, A.; Davis, M. E. *J. Phys. Chem. B* **2000,** *104*, 10001-10011.

98. Piccione, P. M.; Yang, S.; Navrotsky, A.; Davis, M. E. *J. Phys. Chem. B* **2002,** *106*, 3629-3638.

99. Knight, C. T. G.; Balec, R. J.; Kinrade, S. D. *Angew. Chem. Int. Edit.* **2007,** *119*, 8296-8300.

100. Knight, C. T. G.; Kinrade, S. D. *Anal. Chem* **1999,** *71*, 265-267.

101. Kinrade, S. D.; Knight, C. T. G.; Pole, D. L.; Syvitski, R. T. *Inorg. Chem.* **1998,** *37*, 4278-4283.

102. Johnson Jr, C. S. *Prog. Nucl. Magn. Reson. Spectr.* **1999,** *34*, 203-256.

103. Dixon, A. M.; Larive, C. K. *Appl. Spectrosc.* **1999,** *53*, 426A-440A.

104. Price, W. S. *Concept. Magnetic. Res.* **1997,** *9*, 299-336.

105. Morris, K. F.; Johnson Jr, C. S. *J. Am. Chem. Soc.* **1992,** *114*, 3139-3141.

106. Morris, K. F.; Johnson Jr, C. S. *J. Am. Chem. Soc.* **1993,** *115*, 4291-4299.

107. Webb, G. A. *Annu. Rep. Prog. Chem., Sect. C: Phys. Chem.* **1992,** *89*, 3-36.

108. Gormally, J.; Sztuba, B.; Wyn-Jones, E.; Hall, D. G. *J. Chem. Soc., Faraday Trans. 2* **1985,** *81*, 395-403.

109. Liu, M.; Nicholson, J. K.; Lindon, J. C. *Anal. Commun.* **1997,** *34*, 225-228.

110. Fielding, L. *Tetrahedron* **2000,** *56*, 6151-6170.

111. Lin, M.; Shapiro, M. J.; Wareing, J. R. *J. Org. Chem.* **1997,** *62*, 8930-8931.

112. Lin, M.; Shapiro, M. J.; Wareing, J. R. *J. Am. Chem. Soc.* **1997,** *119*, 5249-5250.

113. Hajduk, P. J.; Olejniczak, E. T.; Fesik, S. W. *J. Am. Chem. Soc.* **1997,** *119*, 12257-12261.

114. Altieri, A. S.; Hinton, D. P.; Byrd, R. A. *J. Am. Chem. Soc.* **1995,** *117*, 7566-7567.

115. Jayawickrama, D. A.; Larive, C. K. *Anal. Chem* **1999,** *71*, 2117-2122.

116. Tyrrell, H. J. V.; Harris, K. R., *Diffusion in liquids: A theoretical and experimental study*. Butterworths: 1984.

117. Heitjans, P.; Kärger, J., *Diffusion in condensed matter: methods, materials, models*. Springer Verlag: 2005.

118. Stejskal, E. O.; Tanner, J. E. *J. Chem. Phys.* **1965,** *42*, 288-292.

119. Tanner, J. E. *J. Chem. Phys.* **1970,** *52*, 2523-2526.

120. Lucas, L. H.; Otto, W. H.; Larive, C. K. *J. Magn. Reson.* **2002,** *156*, 138-145.

121. Callaghan, P. T., *Principles of nuclear magnetic resonance microscopy*. Oxford University Press, USA: 1993.

122. Kärger, J.; Pfeifer, H.; Heinik, W. *Adv. Magn. Reson.* **1988,** *12*, 1-89.

123. Roberts, G. C. K., *NMR of macromolecules: a practical approach*. Oxford University Press, USA: 1993.

124. Chen, A.; Johnson Jr, C. S.; Lin, M.; Shapiro, M. J. *J. Am. Chem. Soc.* **1998,** *120*, 9094-9095.

125. Mansfield, P.; Waugh, J. S., *Advances in magnetic resonance*. Academic Press: 1988.

126. Johnson, C. S. *J. Magn. Reson. Ser. A* **1993,** *102*, 214-218.

127. Choudhury, R. P.; Schönhoff, M. *J. Chem. Phys.* **2007,** *127*, 234702-234711.

128. Brown, W., *Dynamic light scattering: the method and some applications*. Clarendon Press: 1993.

129. Dahneke, B. E., *Measurement of suspended particles by quasi-elastic light scattering*. John Wiley & Sons: 1983.

130. Mills, R. *J. Chem. Phys.* **1973,** *77*, 685-688.

131. Söderman, O.; Stilbs, P.; Price, W. S. *Concept. Magnetic. Reson. A* **2004,** *23*, 121-135.

132. Flood, C.; Cosgrove, T.; Espidel, Y.; Howell, I.; Revell, P. *Langmuir* **2008,** *24*, 7323-7328.

133. Lapham, J.; Rife, J. P.; Moore, P. B.; Crothers, D. M. *J. Biomol. NMR* **1997,** *10*, 255-262.

134. Hedlund, J.; Mintova, S.; Sterte, J. *Microporous Mesoporous Mater.* **1999,** *28*, 185-194.

135. Thomas, W. J.; Crittenden, B. D., *Adsorption technology and design*. Butterworth-Heinemann: 1998.

136. Choucair, A.; Eisenberg, A. *J. Am. Chem. Soc.* **2003,** *125*, 11993-12000.

137. Adamson, A. W.; Gast, A. P.; NetLibrary, I., *Physical chemistry of surfaces*. Wiley New York: 1997.

138. Kerr, G. T.; Kokotailo, G. T. *J. Am. Chem. Soc.* **1961,** *83*, 4675-4675.

139. Li, X.; Shantz, D. F. *J. Phys. Chem. C* **2010,** *114*, 8449-8458.

140. Kannan, N.; Sundaram, M. M. *Dyes. Pigments.* **2001,** *51*, 25-40.

141. Chang, Y. C.; Chen, D. H. *Macromol. biosci.* **2005,** *5*, 254-261.

142. Ho, Y. S.; Wase, D. A. J.; Forster, C. F. *Environ. Technol.* **1996,** *17*, 71-77.

143. Bai, B.; Wu, Y.; Grigg, R. B. *J. Phys. Chem. C* **2009,** *113*, 13772-13779.

144. Mahanta, D.; Madras, G.; Radhakrishnan, S.; Patil, S. *J. Phys. Chem. B* **2009,** *113*, 2293-2299.

145. Weber, W. J.; Morris, J. C. *J. Sanit. Eng. Div. Am. Soc. Civ. Eng.* **1963,** *89*, 31-60.

146. Fegan, S. G.; Lowe, B. M. *J. Chem. Soc., Faraday Trans. 1* **1986,** *82*, 785-799.

147. Schoeman, B. J. *Microporous Mesoporous Mater.* **1998,** *22*, 9-22.

148. Pavel, C. C. *Microporous Mesoporous Mater.* **2004,** *71*, 77-85.

149. Iwasaki, A.; Sano, T.; Kiyozumi, Y. *Microporous Mesoporous Mater.* **1998,** *25*, 119-126.

150. Kirschhock, C. E. A.; Kremer, S. P. B.; Grobet, P. J.; Jacobs, P. A.; Martens, J. A. *J. Phys. Chem. B* **2002,** *106*, 4897-4900.

151. Hunter, R. J.; White, L. R.; Chan, D. Y. C., *Foundations of colloid science*. Clarendon Press Oxford: 1989.

152. Hibbert, D. B.; James, A. M. *Macmillan Press Ltd* **1984**.

153. Smedley, S. I., *The interpretation of ionic conductivity in liquids*. Plenum Press New York: 1980.

154. O'Connor, T. L.; Greenberg, S. A. *J. Chem. Phys.* **1958,** *62*, 1195-1198.

155. Atkins, P. W., *Physical chemistry*. 5th ed.; Oxford University Press, Oxford: 1997.

156. Castellan, G. W., *Physical chemistry: the elecfricul current in ionic rolutions*. Addison-Wesley Publishing Co., Reading, MA: 1983.

157. Hiemenz, P. C.; Rajagopalan, R., *Principles of colloid and surface chemistry*. ACS publications: 1997.

158. Fan, W.; Ogura, M.; Sankar, G.; Okubo, T. *Chem. Mater.* **2007,** *19*, 1906-1917.

159. Ryoo, R.; Jun, S. *J. Phys. Chem. B* **1997,** *101*, 317-320.

160. Johnson, A. C. J. H.; Greenwood, P.; Hagstro m, M.; Abbas, Z.; Wall, S. *Langmuir* **2008,** *24*, 12798-12806.

161. Dishon, M.; Zohar, O.; Sivan, U. *Langmuir* **2009,** *25*, 2831-2836.

162. Lu, Y.; Yang, Y.; Sellinger, A.; Lu, M.; Huang, J.; Fan, H.; Haddad, R.; Lopez, G.; Burns, A. R.; Sasaki, D. Y. *Nature* **2001,** *410*, 913-917.

163. Cha, J. N.; Stucky, G. D.; Morse, D. E.; Deming, T. J. *Nature* **2000,** *403*, 289-292.

164. Waldeck, A. R.; Kuchel, P. W.; Lennon, A. J.; Chapman, B. E. *Prog. Nucl. Magn. Reson. Spectr.* **1997,** *30*, 39-68.

165. Yokoi, T.; Sakamoto, Y.; Terasaki, O.; Kubota, Y.; Okubo, T.; Tatsumi, T. *J. Am. Chem. Soc.* **2006,** *128*, 13664-13665.

166. Yokoi, T.; Wakabayashi, J.; Otsuka, Y.; Fan, W.; Iwama, M.; Watanabe, R.; Aramaki, K.; Shimojima, A.; Tatsumi, T.; Okubo, T. *Chem. Mater.* **2009,** *21*, 3719-3729.

167. van de Water, L. G. A.; van der Waal, J. C.; Jansen, J. C.; Cadoni, M.; Marchese, L.; Maschmeyer, T. *J. Phys. Chem. B* **2003,** *107*, 10423-10430.

168. van de Water, L. G. A.; van der Waal, J. C.; Jansen, J. C.; Maschmeyer, T. *J. Catal.* **2004,** *223*, 170-178.

169. van de Water, L. G. A.; Zwijnenburg, M. A.; Sloof, W. G.; van der Waal, J. C.; Jansen, J. C.; Maschmeyer, T. *Chem. Phys. Chem.* **2004,** *5*, 1328-1335.

170. Corma, A.; Nemeth, L. T.; Renz, M.; Valencia, S. *Nature* **2001,** *412*, 423-425.

171. Zones, S. I.; Hwang, S. J. *Microporous Mesoporous Mater.* **2003,** *58*, 263-277.

172. Hould, N. D.; Lobo, R. F. *Chem. Mater.* **2008,** *20*, 5807-5815.

173. Liu, H.; Ernst, H.; Freude, D.; Scheffler, F.; Schwieger, W. *Microporous Mesoporous Mater.* **2002,** *54*, 319-330.

174. Yuan, S. P.; Wang, J. G.; Li, Y. W.; Jiao, H. *J. Phys. Chem. A* **2002,** *106*, 8167-8172.

175. Schaack, B. B.; Schrader, W.; Schu th, F. *J. Phys. Chem. B* **2009,** *113*, 11240-11246.

176. Knight, C. T. G.; Kinrade, S. D. *J. Phys. Chem. B* **2002,** *106*, 3329-3332.

VITA

Name: Xiang Li

Address: Department of Chemical Engineering
Texas A&M University
TAMU 3122
College Station, TX 77843-3122

Email Address: lixiang1983-judy@hotmail.com

Education: Ph.D., Chemical Engineering, Texas A&M University, 2011
M.S., Chemical Engineering, Tianjin University, 2007
B.S., Applied Chemistry, Beijing University of Chemical Technology, 2005